TOKYO METROPOLITAN UNIVERSITY

Doctoral Dissertation

Methodologies Based on Vibroarthrographic Signals for Knee Disorders Diagnosis

Rui Gong

Abstract

In modern society, as people live longer and longer, there are many diseases of middle and old age that come with it. Knee-related diseases have a serious impact on the quality of life of people, causing pain, sleepless nights, and even disability. Knee osteoarthritis (OA) is a representative type of knee disorder that is difficult to diagnose and difficult to treat. Although medical imaging technologies such as computed tomography (CT) and magnetic resonance imaging (MRI) have been developed and promoted, their high cost and inability to detect diseases in the early stages are still not enough to meet all the needs of clinical applications. We noted this problem and proposed the hypothesis of diagnosing knee disorders based on vibrations and sounds, which has known vibroarthrography (VAG) signal during knee movement.

To test this hypothesis, this study needs a system that can transform the sound or vibration of the knee joint into a biomedical signal that can be continuously monitored and analyzed. As the collected VAG signals may contain outliers, missing values, and noise, new pre-processing and post-processing algorithms also need to be developed to handle the signal. When analyzing VAG signals, in addition to the traditional use of time series analysis methods, feature engineering and machine learning are required to analyze and classify the signals. Finally, a validation of the VAG-based method for the diagnosis of knee disorders using a well-established medical diagnostic system is necessary.

Therefore, in this study, a piezoelectric diaphragm-based VAG signal collection system was designed to monitor the VAG signals stably at a very low cost. In addition, an active VAG signal derived from the impact signal was also tried on the knee joint model. For the interference in the VAG signal, this study develops a set of algorithms for noise reducers based on an ant colony algorithm combined with hybrid techniques, together with a new post-processing technique, which allows the real signal part of the signal to be separated from the noise. For the analysis of VAG signals, this developed a feature engineering method based on the plant root system, which has very high independence and is suitable for machine learning classification. The VAG mentioned above signal and its processing analysis methods were also used to classify healthy knees, aging knees, and OA knees, and satisfactory results were obtained.

The contribution of this study is to focus on knee disorders and to lay the foundation for future clinical applications through methods such as the collection and analysis of biomedical signals like VAG signals. Although mechanical wave-based biomedical signals are far more difficult to process than electrical-based biomedical signals, it is possible to expand them from primary research to applications through the system established in this study.

Acknowledgment

Throughout the writing of this dissertation, I have received a great deal of support and assistance.

I would first like to thank my supervisor tutor, Professor Kazunori Hase, whose expertise was invaluable in formulating the research questions and methodology. Your insightful feedback pushed me to sharpen my thinking and brought my work to a higher level. I would also like to thank Prof. Wakayama, Prof. Yoshimura, and Prof. Ota for your insights and pertinent suggestions that have enhanced this work. Thank you to all reviewers of this dissertation; your comments and advice complete my dissertation successfully.

I would also like to thank my classmates in the Hase lab for their wonderful cooperation. I would particularly like to single out Asst. Prof. Yoshida and Hayashi, Ms. Yishizuka, Ms. Nagao, I want to thank you for your patient support and unparalleled help.

I would like to acknowledge Mr. Goto and Mr. Yoshioka of Livet Inc. Your support and encouragement are indispensable to this work. I had a very pleasant meeting collaborating with you, and your knowledge is a key part of the success of this work.

I would like to acknowledge my colleagues from my career at Mejiro University for their wonderful collaboration.

In addition, I would like to thank my parents and my wife for their wise counsel and sympathetic ear. You are always there for me. Finally, I could not have completed this dissertation without the support of my friends, who provided stimulating discussions as well as happy distractions to rest my mind outside of my research.

Abbreviations

1dNLM	1D non-local mean
ACC	Accuracy
ACF	Autocorrelation Function
ACI	Autologous Cartilage Implantation
ACL	Anterior cruciate ligament
ACO	Ant Colony Optimization
ADC	Analog-to-Digital Converter
AUC	Area Under the Curve
BMD	Bone Mineral Density
CGT	Continuous Gaber transform
CSV	Comma Separated Values
CT	Computed Tomographs
CWT	Continuous Wavelet Transform
DFT	Discrete Fourier transform
DICOM	Digital Imaging and Communications in Medicine
DTW	Dynamic Time-warping
DWT	Discrete WT
ECG	Electrocardiogram
EEG	Electroencephalogram
EEMD	Ensemble EMD
EMD	Empirical Mode Decomposition
EMG	Electromyography
FFT	Fast Fourier Transform
FN	False-Negative
FO	Futility Object
FP	False-Positive
FT	Fourier Transform
FWHM	Full Width at Half Maximum
GA	Genetic Algorithm
GA	Genetic Algorithm
GRBF	Gaussian Radial Basis Function
GUI	Graphical User Interface
HHT	Hilbert-Huang Transform
IMF	Intrinsic Mode Function

IMFs	Intrinsic Mode Functions
KA	Knee Arthroplasty
KL	Kellgren-Lawrence
KNN	k-nearest neighbors
KURT	Kurtosis
LCL	Lateral collateral ligament
LDA	Linear Discriminant Analysis
LFc	lateral femoral cartilage
LR	Logistic Regression
LSSVM	Least squares support vector machine
LTc	lateral tibial cartilage
MAE	Mean Absolute Error
MAV	Mean Absolute Value
MaxPSD	Max Power Spectrum Density
MCL	Medial collateral ligament
MedPSD	Median Power Spectrum Density
MEMS	Microelectromechanical Systems
MFc	medial femoral cartilage
MMG	Mechanomyogram
MR	Magnetic Resonance
MRI	Magnetic Resonance Imaging
MSE	Mean Squared Error
MSE	Mean Squared Error
MTc	medial tibial cartilage
NA	Not Applicable
NF	Nutrition Feature
NLE	Non-linear Energy
NLM	Nonlocal Means
OA	Osteoarthritis
OGS	Outerbridge Grading Systems
OLA	Overlap–add
PCA	Principal Component Analysis
PCA	Principal component analysis
PCC	Pearson Correlation Coefficient
PCC	Pearson correlation coefficient
PCL	Posterior cruciate ligament

PRD	Percentage Root Mean Square Difference
PRE	Precision
PRS	Plant Root System
PSNR	Peak SNR
Pt	Patellar tendon
PZT	Lead Zirconate Titanate
QDA	Quadratic Discriminant Analysis
QoL	Quality of Life
Qt	Quadriceps tendon
RF	Root Feature
RLC	Resistor Inductor Capacitor Electrical Circuit
RMS	Root Mean Square
RMSE	Root-Mean-Square Error
ROC curve	Receiver Operating Characteristic curve
SG filter	Savitzky–Golay Filter
SKW	Skewness
SNR	Signal-to-Noise Ratio
SPE	Specificity
SPE	Specificity
SPI	Serial Peripheral Interface
SSA	Singular Spectrum Analysis
SSC	Slope Sign Change
SSI	Simple Sign Integral
SSIM	Structural Similarity Index
STD	Standard deviation
STFT	Short-Time Fourier Transform
STL	Standard Triangulated Language
STMA	Soft-tissue Movement Artifacts
SVM	Support Vector Machine
SWT	Stationary WT
TN	True-Negative
TO	Target Object
TP	True-Positive
UI	Ultrasound Imaging
US	Ultrasonography
VAG	Vibroarthrography

VAR	Variance of Signal
VAS	Visual Analog Scale
WAMP	Willison Amplitude
WHO	World Health Organization
WL	Waveform Length
WT	Wavelet Transform
ZC	Zero Crossing
ZCR	Zero-Crossing Rate

Contents

List of Figures

List of Tables

TOKYO METROPOLITAN UNIVERSITY

List of Equation

Chapter1

Introduction

1.1 Background

The World Health Organization (WHO) has been working to investigate the Quality of Life (QoL) of people in cities around the world[1]. The WHO found that although the economic development index varies from city to city, the most important factor affecting QoL is the loss of health. Many studies have reported that motor disability is the number one negative factor for health-related QoL in the middle to high age groups, especially knee pain-related diseases being repeatedly reported[2,3]. Therefore, the health of the knee joint is getting a lot of attention and worry.

In fact, as people are worried, the chances of knee joint breakdown are reaching a daunting level as life expectancy continues to increase. Knee disorders such as knee osteoarthritis (OA) are eroding the normal life of middle to high-age people, the suffer the knee pain and eventually disability. In Japan, which has the highest per capita life expectancy in the world, it is predicted that around 2025, more than 11 million people will suffer from daily knee pain that may not go away for life[3,4]. In other words, one-tenth of the population or one-third of the elderly population is about to suffer from knee joint disease. Hence, further exploration of the knee joint and knee-related disorders is time to act.

1.2 Knee Joint Anatomy

Dr. Richard A. Berger, one of the world's most renowned surgeons associated with knee replacement surgery, has stated more than once that the knee joint is the most complex of all joints. Based on sports anatomy, the knee joint can be simply divided into two parts: hard tissue and soft tissue[5].

1.2.1 The Hard Tissue in the Knee Joint

Hard tissue, also known as calcified tissue, refers to the bone in the knee joint. The knee joint is formed between the two major long bones of the lower limb: the tibia, lying between the knee and the ankle, and the femur, lying between the knee and the hip (Figure 1.2.1). Although the fibula contributes to the ankle joint, it is not part of the knee joint. However, there is a third bone present at the knee, the patella (kneecap), which forms the patellofemoral joint by running along the intertrochanteric groove in the femur[5].

Although the femur and tibia provide the major support brace for standing or walking, it can also be seen in Figure 1.2.1 that the structure is not as simple as it seems. The presence of condyle and epicondyle at the end points of the two long bones is what allows the knee joint to complete flexion extension[6]. However, these movements cannot be performed by the hard tissues independently but

require the collaboration of the soft tissues, which are described in detail in the following subsection.

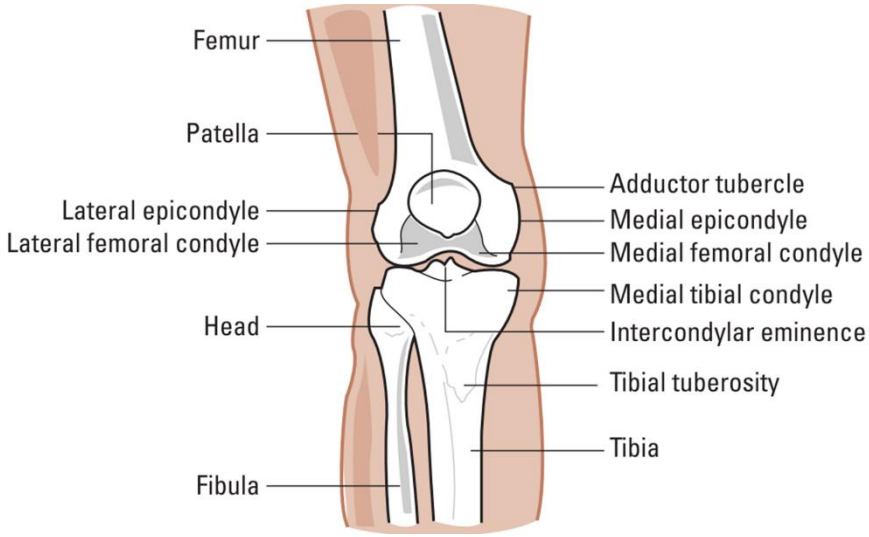

Figure 1.2.1 An anterior view of the right knee joint[5]

The hard tissues of the knee, due to their hard texture and being encapsulated by soft tissues, damage usually occurs from the soft tissues to the hard tissues, except for trauma. However, for genetic or as yet unknown reasons, the femoral or tibial bone marrow can become strange, with damage occurring from hard tissues to soft tissues[7]. This phenomenon is beyond the scope of this paper.

1.2.2 The Soft Tissue in the Knee Joint

The soft tissues of the knee are mainly the cartilage, meniscus, and ligaments. To complete a simple walking movement cannot be without them; it can be said to be the core of lower limb sports.

1.2.2.1 The Cartilage

The cartilage of the knee joint is mainly divided into two parts: patella cartilage and articular cartilage[8,9], and this paper only explicitly discusses the articular cartilage. Cartilage is composed of collagen and water. At least five or more amino acid components have been identified in the collagen cartilage, an irreplaceable framework material[10,11]. The cartilage is usually attached to the epicondyle and condyle, flexes and extends with the long bones, and does not come off easily. However, cartilage is of a certain thickness and may be thin due to wear and tear or making cartilage lesions due to trauma. Although thinning of the cartilage and bumpy of the cartilage surface are both considered to be early stages of knee osteoarthritis, patients also do not notice this lesion because of symptoms such as pain. Bacon Kathryn et al. suggest that the thickness of cartilage is not related to pain[12].

The articular cartilage can be divided by location into lateral femoral cartilage (LFc), medial femoral cartilage (MFc), lateral tibial cartilage (LTc), and medial tibial cartilage (MTc). Although there are few studies on the incidence of cartilage lesions in different locations, the author believes that the femoral

cartilage is more susceptible to damage because it has a larger contact surface. A typical arthroscopic image of cartilage is shown in Figure 1.2.2.

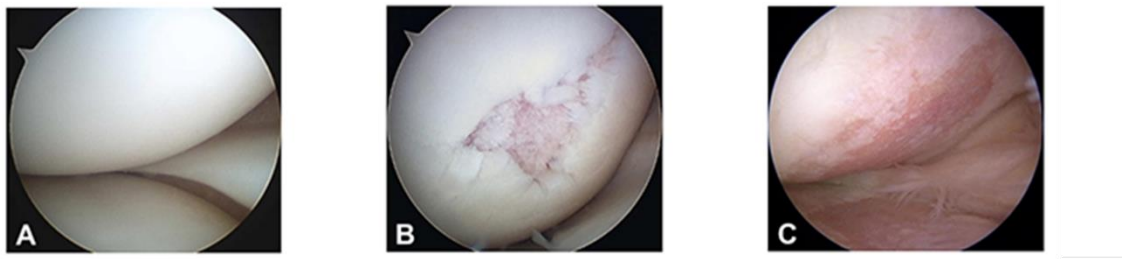

(A) Healthy cartilage (B) Mildly lesioned cartilage (C) Cartilage in knee osteoarthritis

Figure 1.2.2 Three arthroscopic images of cartilage in different stages[13].

Outerbridge classification can connect cartilage damage to knee osteoarthritis[14]. In Figure 1.2.2 (A), the cartilage surface is smooth, and the knee joint is considered healthy. In Figure 1.2.2 (B), there are cracks and bumpy on the cartilage surface, which is considered as early knee osteoarthritis. In Figure 1.2.2 (C), the cartilage disappears to expose the subchondral bone, which is thought to be late-stage knee osteoarthritis. A more detailed graph of the Outerbridge classification of femoral cartilage is shown in Figure 1.2.3.

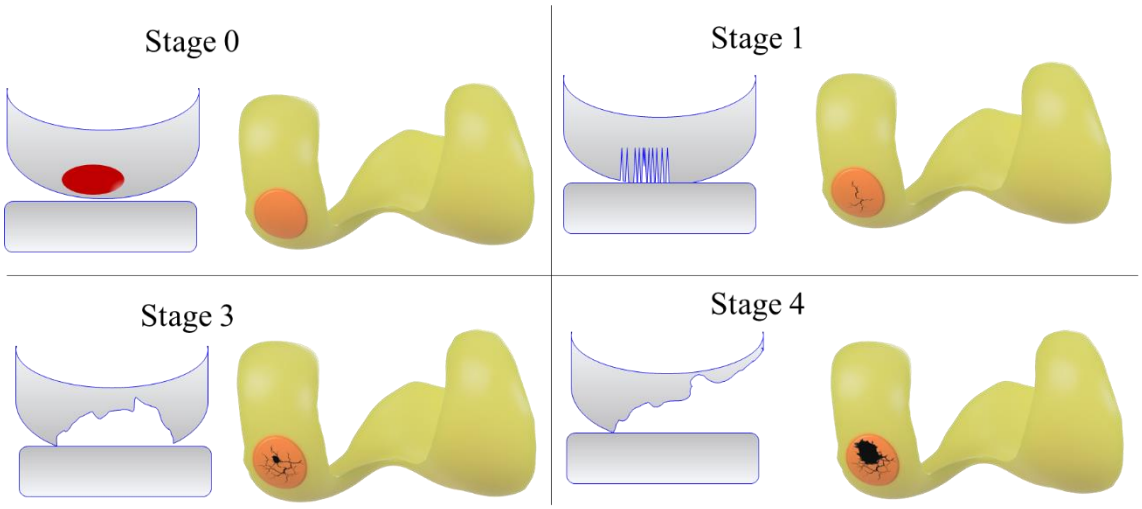

Figure 1.2.3 The medial femoral cartilage damage by Outerbridge Grading Systems.

The left side is a cross-section of medial femoral cartilage anatomy, and the right side is a front-view of the medial femoral cartilage 3D model. Stage 1: Softening and swelling; Stage 2: Fissures on the surface (diameter<1.5cm); Stage 3: Fissuring to the subchondral bone (diameter<1.5cm); Stage 4: Exposed subchondral bone.

In fact, cartilage diseases such as those mentioned above are most common in middle-aged and elderly people, active or retired sports players, or people who are overweight. This is because the

cartilage has excellent mechanical properties and is tightly bound to the subchondral bone[15]. The meniscus, which will be mentioned below, will face a more complex environment than cartilage.

1.2.2.2 The Meniscus

A meniscus is a crescent-shaped fibrocartilaginous anatomical structure that is also composed of collagen and water. The meniscus is commonly used to refer to the meniscal tissue of the knee joint, the lateral or medial meniscus, where the cartilage provides structural stability to the knee joint when subjected to tension and torque[16]. The meniscus was once mistakenly thought by researchers to be a part of the human body that had not fully evolved. However, as researchers have studied biomechanics, it has become increasingly clear that the meniscus plays an irreplaceable role in the knee joint[5]. The meniscus is now known to contribute to stability, shock absorption, load transfer, and stress distribution within the knee joint. Unfortunately, most meniscal damage cannot be effectively healed by the body.

A knee meniscus that is prone to tearing and difficult to heal has an important relationship with its location and shape in the knee joint. In cross-section, both menisci are wedge-shaped with a thick peripheral base infiltrated by capillaries, and each meniscus covers approximately two-thirds of the corresponding articular surface of the tibia[17], as shown in Figure 1.2.4.

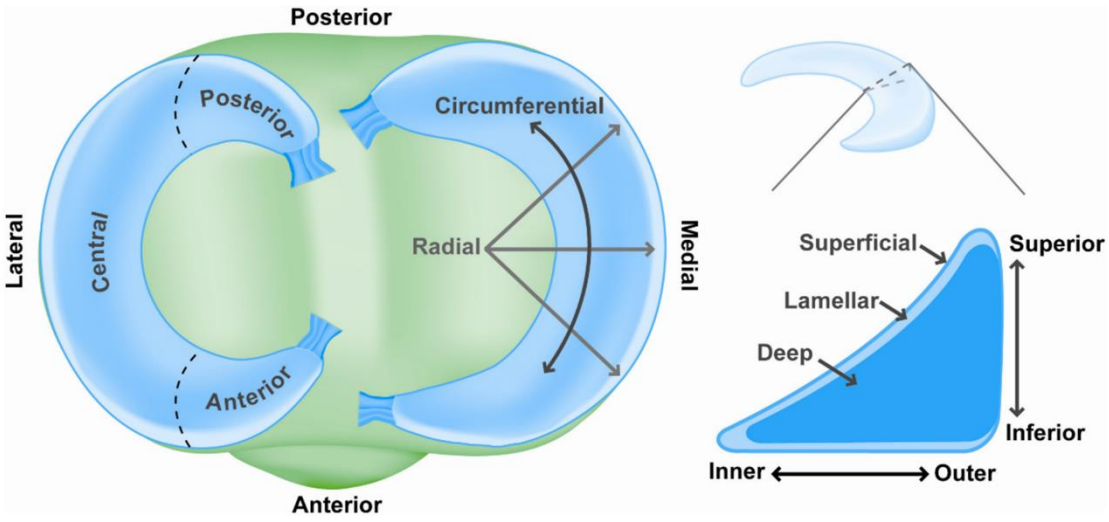

Figure 1.2.4 Regions and directions of the meniscus[16].

Unlike articular cartilage, because meniscal properties vary with location in the tissue, defining different regions, depth zones, and directions is useful. At the same time, when the meniscus is displaced, the large tensile and shear forces caused by the movement are not well tolerated, and the meniscus will be torn. Although there is some debate about the direct relationship between meniscal damage and articular cartilage counts as well as knee OA, it is generally accepted that the majority of the meniscus is disappeared in the later stages of knee OA[18][19].

1.2.2.2 The Ligaments

The main component of a ligament is a long collagen fiber, which is a short bundle of tough connective tissue that connects bone to bone, shapes, and reinforces the joint. In the knee joint, the four main ligaments in the knee connect the femur to the tibia and include the following. An anterior cruciate ligament (ACL): the ligament located in the center of the knee that controls rotation and forward movement of the tibia. A posterior cruciate ligament (PCL): the ligament located in the center of the knee that controls backward movement of the tibia. Medial collateral ligament (MCL): the ligament that gives stability to the inner knee. Lateral collateral ligament (LCL): the ligament that gives stability to the outer knee[20]. As shown in Figure 1.2.5.

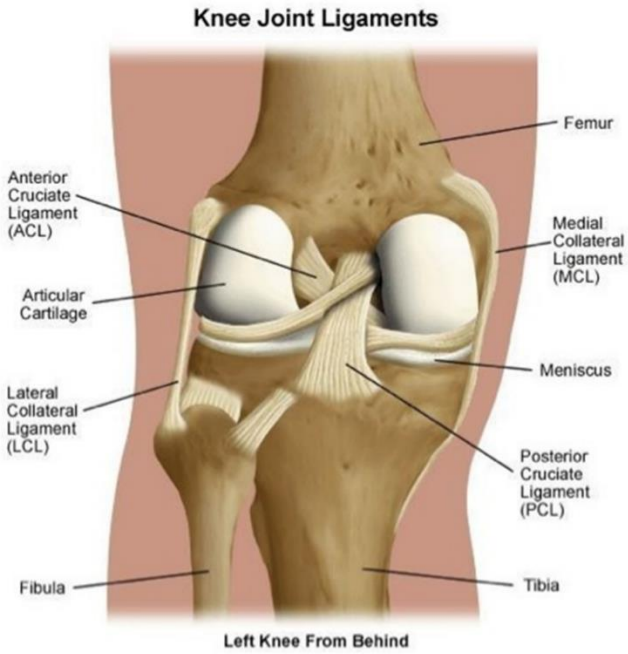

Figure 1.2.5 The ligaments in the left knee joint[20].

As a hinge in the knee joint, like the meniscus, is highly susceptible to tearing while carrying the forces and torques in movement. When the movement exceeds the movable domain by the ligaments with great force, the ligaments tear and are accompanied by severe pain[21]. Torn ligaments in the knee do not directly cause knee OA, but incompletely healed ligaments can reduce knee stability and thus indirectly increase the risk of knee OA[5,21,22].

1.3 Biomechanics of the Knee

The biomechanics of the knee is a large and complex research topic to which a large number of researchers have devoted significant efforts. However, the most basic movement for a knee joint is flexion-extension movement [6,23]. Therefore, this subsection focuses on how the knee joint can carry a flexion-extension movement in a three-dimensional space consisting of axes and planes. A spatial coordinate system is defined as shown in Figure 1.3.1.

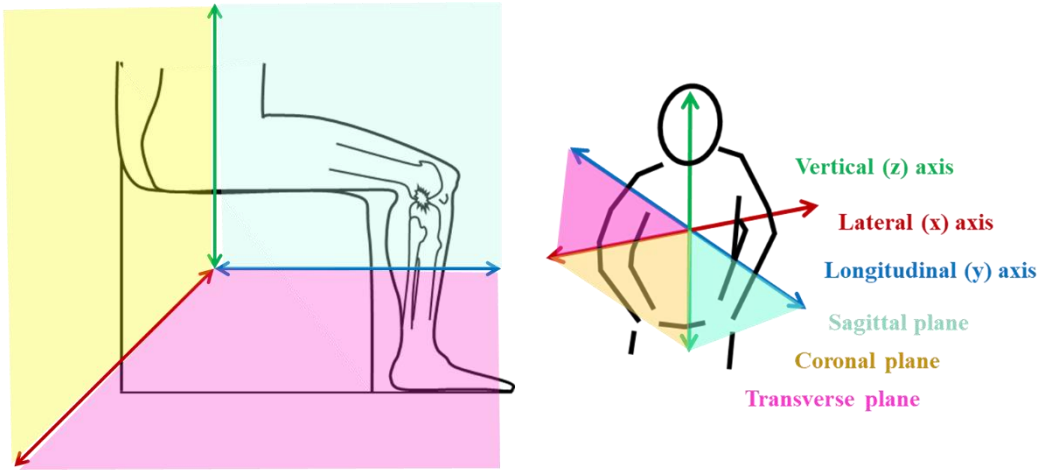

Figure 1.3.1 A spatial coordinate system.

The coordinate axis consists of the sagittal plane, coronal plane, and transverse plane. The axes intersected by the sagittal and transverse planes are the longitudinal axes. The vertical axis is sandwiched by the coronal and sagittal planes. The remainder is the lateral axis. The three axes are positive directions at the divergent point.

When a person sits in a height-adjustable chair with the lower leg (tibia) exactly perpendicular to the transverse plane and the femur parallel to the transverse plane, the tibia is considered to be parallel to the vertical axis, in flexion[5]. When the person stands up with the femur and tibia in a straight line and perpendicular to the ground, it is the extension. Here is a quick cheat sheet of the degrees of knee flexion required to do everyday movements, as shown in Table 1.3.1[24].

Table 1.3.1 The degrees of knee flexion in movements

Degrees of knee	Movements
65°	Walking
70°	Lifting an object from the floor
85°	Climbing stairs
95°	Sitting and standing comfortably
105°	Tie shoelaces
115° (greater)	Squat or sit cross-legged

The degree of freedom of the knee joint is not only limited to flexion and extension but can be moved in other angles as well, with a smaller range of motion that is not easily observed[25]. It is generally accepted that there are six degrees of freedom of knee motion, as shown in Figure 1.3.2[26].

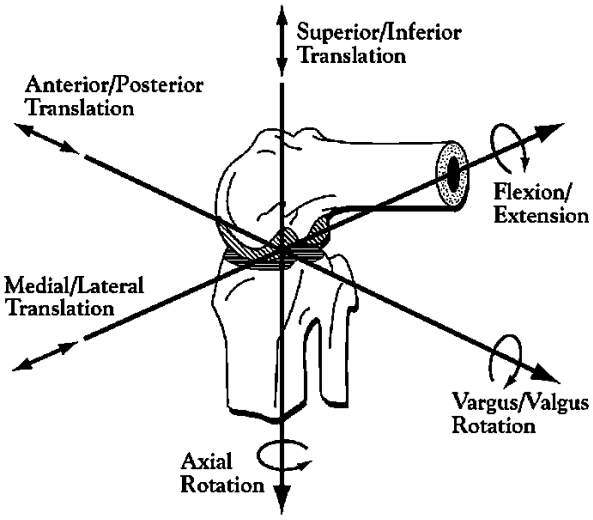

Figure 1.3.2 Six degrees of freedom of the knee joint

1.4 Knee Joint Diseases and Diagnosis

The first sign of almost all knee disorders is the same: knee pain. Knee pain is a common complaint that affects people of all ages. Knee pain may be the result of an injury, such as a ruptured ligament or torn cartilage. Furthermore, arthritis, gout, and infections also can cause knee pain. Many types of minor knee pain respond well to self-care measures. Physical therapy and knee braces also can help relieve pain. In some cases, however, the pain knee may require surgical repair[27].

Besides knee pain, there are some signs that point to the knee needing a complete diagnosis. When the following symptoms occur in conjunction with knee pain, the pain knee may need a doctor.

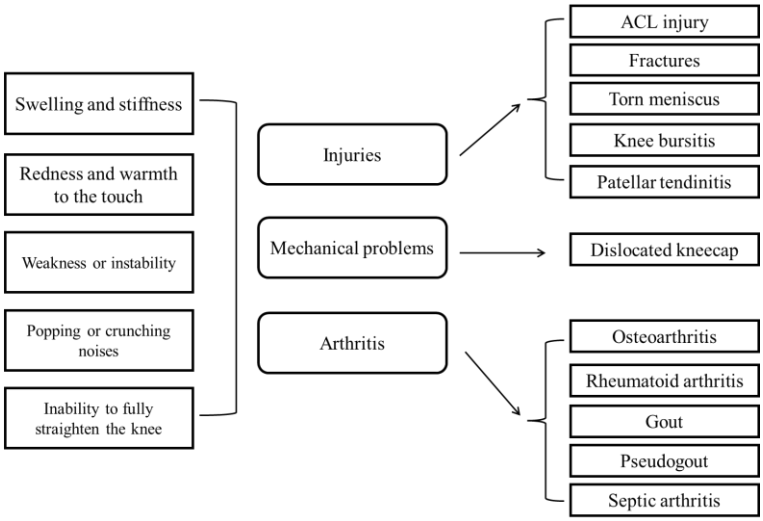

Figure 1.4.1 The symptoms of knee pain and knee joint diseases

In Figure 1.4.1, knee-related diseases are grouped into three categories, and the symptoms associated with these diseases are described. Among them, the disease that needs the most attention is knee OA.

As we described in the previous section, knee OA has a very high incidence and causes both physical and psychological damage to the patient. Therefore, accurate diagnosis of knee OA in the early stage becomes a common aim for doctors.

1.4.1 Radiograph Medical Imaging-based Method for Non-Invasive Diagnosis of Knee

X-rays have been used in orthopedics for a long time, and although the tool is better used in traumatic injuries such as fractures, it is also used in the diagnosis of joint diseases. Kellgren-Lawrence (KL) classification is considered the gold method for the diagnosis of knee OA

and has been used since it was invented[28]. The classification is used to stratify patients by joint space narrowing [29]. The chart below is a good illustration of how to categorize patients with knee OA into four classes by radiology.

Figure 1.4.2 The X-ray diagram of the knee OA by KL classification

In Figure 1.4.2, Grade1 representative knee radiograph of KL classification first stage, which demonstrates doubtful narrowing of the joint space with possible osteophyte formation. Grade2 representative knee radiograph of KL classification second stage, which demonstrates possible narrowing of the joint space with definite osteophyte formation. Grade3 representative knee radiograph of KL classification third stage, which demonstrates definite narrowing of joint space, moderate osteophyte formation, some sclerosis, and possible deformity of bony ends. Grade4 representative knee radiograph of KL classification last stage, which demonstrates large osteophyte formation, severe narrowing of the joint space with marked sclerosis, and definite deformity of bone ends[28].

Although the KL classification is the classical diagnosis of knee OA by X-ray, with the development of orthopedic diagnostics, it has still been found that the method has limitations in both accuracy and usability (Negative type). On the other hand, after the combined X-ray and computer technology, digital x-ray computed tomographs (CT) were applied to the clinical diagnosis of knee OA[30]. Unlike a simple X-ray study, the CT offers a much higher level of detail, creating computerized, 360-degree views of the body's structures. The scans are fast and detailed. This means that a 3D model can be quickly created from these tomography scans, allowing doctors and researchers to easily diagnose

knee disorders or space narrowing from multiple angles[30]. Based on X-ray and CT, a standing X-ray and CT are widely used in the diagnosis of knee OA. This is because the level of narrowing of the knee joint space in the daily state can be recognized more clearly when weight loading[31]. Because the CT scans take much longer than x-rays, reliable support is needed to keep the patient's lower extremity stable during the scan. Both X-ray and CT are called a radiograph and have limitations in diagnosis, in addition to causing a certain amount of radiation to the patient. As the radiation is directed to the body, the areas with high levels of calcium (bones and teeth) block the radiation, causing them to appear white on the image. Soft tissues allow the radiation to pass through. They only appear gray or black on the image, won't show subtle bone injuries, soft tissue injuries or inflammation. Therefore, the medical imaging technology other than radiation had been considered for application in the non-invasive diagnosis of knee OA.

1.4.2 Radiation-free Medical Imaging-based Method for Non-invasive Diagnosis of Knee

The biggest benefit of radiation-free medical images is that there is no risk of radiation exposure. In clinical practice, ultrasonography (US) and magnetic resonance imaging (MRI) are the most common[32,33].

US evaluation of the knee is primarily performed with the patient in the supine position, with the obvious notable exception of evaluation of the posterior structures, for which the patient lies prone. Scanning is performed with a high-frequency (ideally, 12 MHz) linear transducer, although a lower-frequency (7–9 MHz) transducer is sometimes better suited for evaluating the deep posterior structures. [32,34]. The US is very safe, but the image resolution is slightly lower. The biggest weakness is that the imaging area is too small to support a comprehensive evaluation. Therefore, it is still very common to use the US as an early-stage knee joint diagnosis based on its portability and ease of operation. If more detailed images are needed, MRI is the mainstay of today's clinical field.

An MRI test uses magnets and radio waves to capture images inside the patient's body without making a surgical incision, same in the US. However, an MRI lets the doctor see the soft tissues in the patient's body along with the bones. This allows them to inspect the elements of the knee that might have been injured during physical activity or from wear and tear. The test can also provide detailed images of various sections of the knee, such as bones, cartilage, tendons, muscles, blood vessels, and ligaments. An MRI takes images in better contrast than other tests, which X-ray, CT, and US. The only risk associated with MRI is the contrast dye. Some people might have an allergic reaction to the contrast dye used in an MRI. The most common type of contrast dye is gadolinium. According to the Radiological Society of North America, these allergic reactions are often mild and easily controlled by medication. A few knee images by US and MRI are shown below.

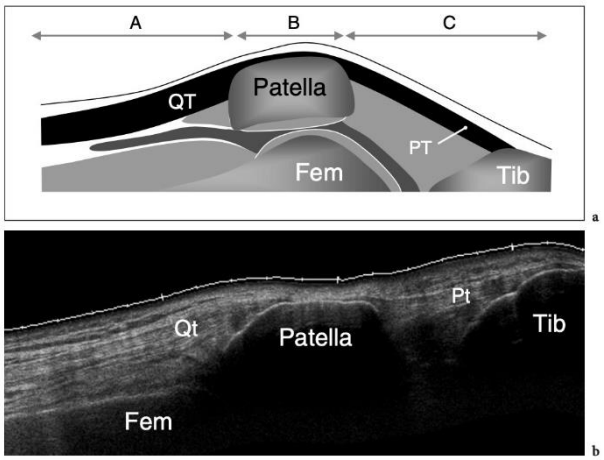

Figure 1.4.3 Anterior aspect of the normal knee of the schematic drawing (a) and the 12–5 MHz US image (b)[35].

Where, the supra-patellar (A), iuxta-patellar (B) and infra-patellar (C) regions. Due to their superficial location, the main structures of the extensor mechanism of the knee, the quadriceps tendon (Qt), the patella and the patellar tendon (Pt) are well depicted with US. Fem, femur; Tib, tibia [35].

Figure 1.4.4 The image is from the knee of a ten-year-old female who had a minor injury 2 days earlier[36].

Where, there is no significant marrow edema signal, and the overlying cartilage is intact. No undermining fluid or cystic change to suggest the latter.

Apply the US to rough diagnostics because it is convenient and inexpensive. Apply MRI to precision diagnostics because it is detailed and expensive. Although everything looked so perfect, the surgeon found during surgery that the medical images were far from the real knee.

1.4.3 Diagnosis of the Knee by Arthroscopy

Knee arthroscopy is a surgical technique that can diagnose and treat problems in the knee joint. During the procedure, the surgeon will make a very small incision and insert a tiny camera — called an arthroscope — into the pain knee. This allows them to view the inside of the joint on a screen. The surgeon can then investigate a problem with the knee and, if necessary, correct the issue using small instruments within the arthroscope.

Arthroscopy is undoubtedly invasive, even if this small incision can only cause limited pain. Often patients have the question, why do I need an arthroscopy after undergoing an X-ray or MRI. First, this is because arthroscopy allows visualization of every part of the knee joint, such as the cartilage surface and meniscus. This visualization facilitates the surgeon to make a proper determination of the knee damage. Second, because arthroscopy is an important surgical aid when the surgeon performs autologous cartilage implantation (ACI) and knee arthroplasty (KA), arthroscopic diagnosis can help the surgeon make the surgery go smoothly shown in Figure 1.2.2[37].

The above medical portraits are widely used in the diagnosis of knee OA but also impose a serious financial burden on the patients. Even the cheapest US requires expensive equipment costs and a large number of consumables and requires specialized medical personnel to operate. Thus, a diagnostic method for knee OA that is not based on medical imaging urgently needs to be proposed.

1.5 Vibroarthrography

During normal knee motions, both the intra- and extra-articular components may produce vibrations or sounds as they pass over one another. The knee joint sound, which is emitted from a knee joint in the course of flexion or extension, is referred to as the Vibroarthrography (VAG)[38–40].

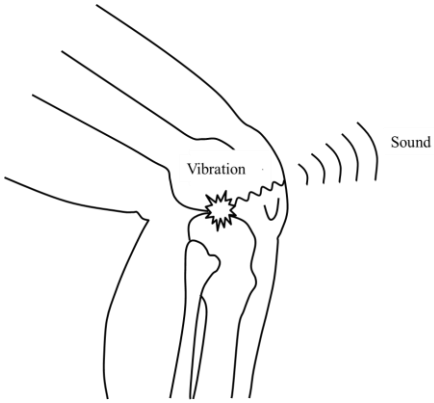

Figure 1.5.1 Sounds and vibrations from the knee joint

1.5.1 A Brief History of VAG Signal

Determining the degree of knee injury by observing knee vibration is an ancient technique, so ancient

that there is no way to trace its origins. However, modern techniques for diagnosing joint vibrations can be traced back 100 years, that auscultation of the knee joint[41,42]. Doctors determine knee disorders by the vibration and sound during flexion and extension movements. This palpation and auscultation technique is extremely dependent on the doctor of experience and has a high probability of miscalculation[41]. Subsequently, there were also attempts to record the sound of the joint with a gramophone or microphone, but they were not successful because the sound was not clear enough. Similarly, sound recording devices such as magnetic tapes were applied to auscultation in the latter half of the 20th century, but still not good to advance knee joint vibration and sound analysis technology[43] But it didn't take long for Chu et al. to successfully diagnose the difference in sound signals between normal and abnormal knees using dual microphones and a unique noise reduction technique[44,45]. This also means that VAG signals are starting to come into clinical applications rather than just being limited to the research field.

With the rapid development of digital technology, VAG signals from the signal collection method to signal analysis have made great progress. By the end of the 20th century, both microphones and accelerometers were used to capture vibrations or sounds in the knee joint, and doctors and researchers corresponded these signals to medical images, creating a relatively complete system of diagnosis of the knee[46–49]. In the 21st century, accelerometers and gyroscopes based on microelectromechanical systems (MEMS) have become lighter, smaller, and more sensitive, and the collected VAG signals can be analyzed in a highly integrated computer[50,51].

1.5.2 Advance Studies of VAG Signal

Patellar chondromalacia is a major application of VAG signals in diagnosis. Researchers have been able to diagnose chondromalacia patellae at an early stage by classifying VAG signals collected from sensors fixed to the kneecap after feature extraction. The classification results are usually compared with the diagnostic results of MRI or CT, and classification accuracy of about 80% can be achieved after enough machine learning[52]. In addition to being used for kneecap injuries, VAG signals have also been used in the diagnosis of ligament injuries and cartilage injuries. Especially in the latter case, disorders of knee cartilage are often accompanied by changes in the roughness of the cartilage surface, generating more sound and vibration during flexion-extension movements[53–55].

There is also controversy over the method of VAG signal generation. Although researchers believe that only VAG signals generated by flexion-extension movements of the knee joint are strong enough to be observed, the way in which the flexion-extension movements are performed is discussed. Tanaka et al. suggested that asking participants to sit on a chair with a height higher than the participant's calf length and then swinging the calf by rocking it in order to obtain the VAG signal would be a good option[56]. Samani et al. instead considered that generating VAG signals by sitting and standing up movements was a good option[57]. In the former case, since the upper body is fixed by the chair, the

noise caused by the change of body weight will be less. The latter will cause the VAG signal to be recorded more clearly due to the change of weight when standing up and sitting down.

Although the VAG signal is an ancient but advanced diagnostic technique for the knee, the collection, and analysis techniques involved with it have been somewhat controversial. The first topic is the presentation of the VAG signal. Due to the VAG signals are essentially mechanical waves, whether they are collected in the form of vibrations or sound is discussed in the biomedical field. Kim et al. believed that the analysis of VAG signals should be attributed to acoustics, and they successfully analyzed the pathology of the knee joint based on acoustics[58]. Umapathy et al. have a different opinion. They considered the VAG signal as vibration and optimized the analysis algorithm for that vibration signal[59]. In addition to wired devices that collect VAG signals, IoMT-based wireless devices are also making a splash[60,61]. As smart medical applications, wearable and wireless based VAG signal collection devices are usually based on Bluetooth communication protocols. IoMT-based VAG signal collection devices have the feature of being lightweight and convenient, but also have the feature of unstable wireless transmission. This is where copper-core cable-based VAG collection equipment sues for high-speed and stable signal transmission for medical applications.

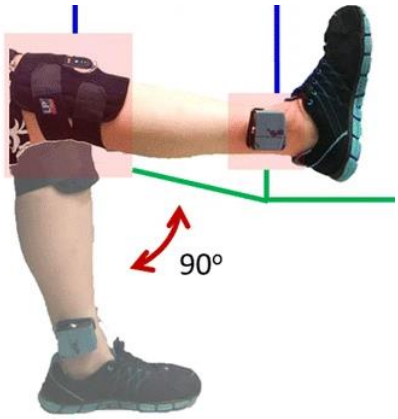

Figure 1.5.2 An IoMT-based VAG signal collection device[62]

The second topic is whether the VAG signal should be pre-processed or not. It is well known that since the VAG signal is collected with flexion-extension motion, the noise from the body motion is also involved in the VAG signal. Krishnan et al. considered the noise contained in the VAG signal to be unacceptable, and they developed an adaptive time-frequency filtering algorithm to remove this noise[63]. At the same time, others believe that filtering loses the information in the real signal and therefore do not recommend pre-processing. Finally, the analysis of the VAG signal has also been discussed. Someone believes that data science and machine learning theories can achieve high accuracy classification without knowing the relationship between VAG signals. This analysis technique is recommended[52]. Others argue that the VAG signal, as a biomedical signal, must be known by mechanism when applied to the clinic and that machine learning is too black-box for modeling[64].

Nowadays, VAG signal has become a complete biomedical signal system from device development, signal collection, signal processing and analysis to clinical application. Despite the debate on the details of the VAG application, the outline of the future direction is still clearly visible.

1.5.3 Challenges and Goals of VAG Signal research

From the above brief, it is clear that the VAG signal is such an excellent biomedical signal that a large number of experts are studying it now. But that doesn't mean it doesn't have challenges in front of the VAG signal. In fact, there are countless topics waiting to be solved. In the following, let's present the problems and solutions by chapter.

The first challenge of any biomedical signal is always the collection of the signal. Although the electronic information technology has been developed, VAG signal still faces this challenge. This dissertation roughly summarizes the following problems, broadly speaking, the problem of the type of generated signal, the problem of sensor attachment, the problem of signal transmission, the problem of sampling rate, etc [53,65–68]. In Chapter 2, a novel VAG signal collection system is designed to not only solve the traditional VAG signal collection problem, but also solve the pain point of difficult operation for non-professionals by designing the interface.

The second challenge comes from the clinical application of the VAG signal. Although VAG signals have been used in the diagnosis of chondromalacia patella and these diseases need to deteriorate to the point of requiring surgery to have a high diagnostic accuracy [52,69], the VAG signal is more powerful in the diagnosis of knee OA. In Chapter 3, a diagnostic maneuver using a combination of VAG signals and mechanical learning is proposed and validated. And in Chapter 4, the clinical application goes even further into diagnosing aging knees and young knees.

The third challenge comes from the processing of VAG signals, which is a common problem for almost all biomedical signals. Chapter 5 describes the pre-processing process of the signal in two parts. Part 1 reviews the pre-processing of the VAG signal, mainly including: changing the length of the VAG signal; removing the baseline drift; removing outliers; filling in missing values; and other pre-processing. Part 2 proposes a noise reduction method for VAG signals based on the ant colony algorithm and dynamic filter parameters. The proposed method works for signals with clear peaks and non-stationary signals with less clear peaks. In addition, this chapter also covers post-processing-based techniques to deal with soft-tissue movement artifacts from vibroarthrographic knee-joint signals.

The fourth challenge comes from building models for normal and abnormal knees, which are feature engineering and classification models. Chapter 6 mainly outlines the feature engineering and classification methods for VAG signals and proposes a novel feature extraction method. The novel method particularly proposes a population intelligence algorithm based on the plant root system, which can contain the main information of the VAG signal while having excellent independence. Several classifiers using this feature can improve the classification accuracy between the VAG signal of normal

knees and the VAG of abnormal knees.

The fifth challenge comes from the VAG signal itself, which as a mechanical wave biomedical signal is very weak and mixed with noise, and the noise will not be removed even after amplification. Since the VAG signal is generated from the friction between the knee joints after cartilage loss, this study had pondered whether the attenuation of the external input signal could be used to diagnose cartilage loss and further diagnose knee OA. In Chapter 7, focuses on the application of attenuation of impact signals on the knee joint model. The knee joint status is evaluated by comparing the attenuation of the input signal before and after passing through the knee joint without any movement. This is a brave and creative attempt to diagnose joints that are no longer affected by the noise of movement. However, since the input signal is an impact signal, this study is only at the knee model stage for now and is considered for future extension to the clinic. An overview of the dissertation structure is shown in Figure 1.5.3.

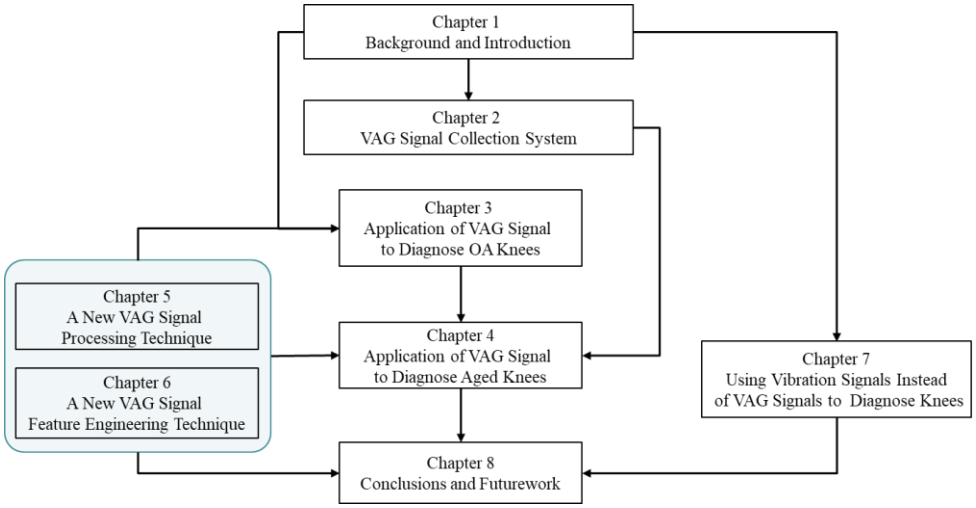

Figure 1.5.3 An overview of the dissertation structure

The goal of this dissertation emerged from the above proposed challenges in the study of VAG signals and the solutions given in each chapter. That is, to construct a well-established diagnostic scheme for knee disorders via VAG signals. Conclusions and future prospects are drawn in Chapter 8. In this chapter, not only the hypothesis proposed at the very beginning of this study is reviewed, the experiments. The results and discussion are again extended further. All the work in this dissertation is summarized and also gives an insightful and precise outlook on the future of VAG signals.

Chapter2

VAG Signal Collection System

The VAG signal is the most common VAG signal, which is a mechanical wave signal generated by friction during joint movement.

2.1 A Sound-based VAG Signal Collection Devices

Based on the fact that the passive VAG signal is a mechanical wave that is not easy to record and save, the first mission is to convert it into an electrical signal. The primary collection device is to record the VAG signal in the form of acoustic or vibrational waves.

Acoustic was used in VAG signal recording in the mid-20th century. Immediately thereafter, the combined microphone and stethoscope device shines in collecting VAG signals[39,48]. The device works on a very simple mechanism. The stethoscope amplifies the knee sound, which is then converted into an electrical signal by the microphone and finally is saved as an electrical signal. There are also two types of saving methods: analog and digital, with the latter being more common today. This is due to the rapid development of analog-to-digital converter (ADC) chips, the sampling rate and sampling depth are getting higher and higher, and the amount of information collected from the VAG signal is getting larger and larger. Here an actual sample to make a case is introduced as follows[70].

The measurement device was made using stethoscopes and electronic components available in the market, considering the possibility of clinical use. The appearance of the device is shown in Figure 2.1.1. The stethoscope is connected to the microphone through a tube, where the knee joint sound is converted into an electrical signal and output as an analog signal. A connector is attached to the base, and the signal waveform can be checked in real-time by connecting to an oscilloscope.

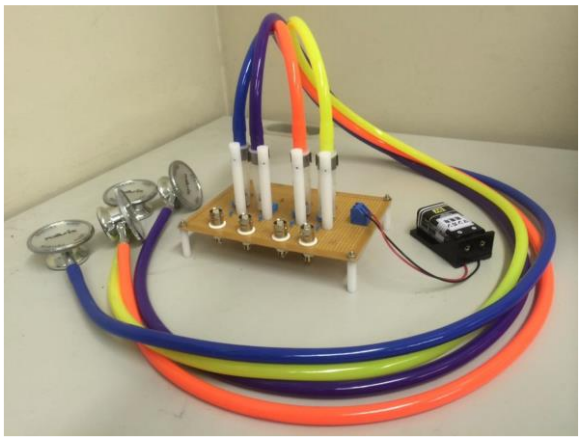

Figure 2.1.1 A knee joint sound measurement system

A mechanical stethoscope (Nursing Scope Double, Kentz Medico Co., Ltd.) was used, and only a chest piece was used as the measuring device. An Omni-directional electret condenser microphone

(C9767BD403 DB Products Limited) was used. A universal base (ICB-505, Sanhayato Co., Ltd.) was used.

Knee joint sounds were measured from four locations around the knee joint. Stethoscopes were attached to the patella, medial femoral epicondyle, lateral femoral epicondyle, and tibia (Figure 2.1.2). In this study, only the data obtained from the tibia was used because the joint sound obtained from the tibia later showed a significant difference between healthy subjects and patients with knee OA, and the shape of the tibia was flat, making it easy to attach the stethoscope and accelerometer. Since cartilage wear, which is the cause of knee OA, is located between the femur and tibia, the tibial area, which is subjected to direct vibration, was considered to be suitable for the stethoscope. The tibia, which was used in this study, is one of the lower leg bones and is a long bone with a triangular cross-section. The tibia is a long bone with a triangular cross-section.

Figure 2.1.2 A view of the actual use of the knee joint sound collection device

In order to make the device more portable, a simplified version of the device was developed, as shown in Figure 2.1.3.

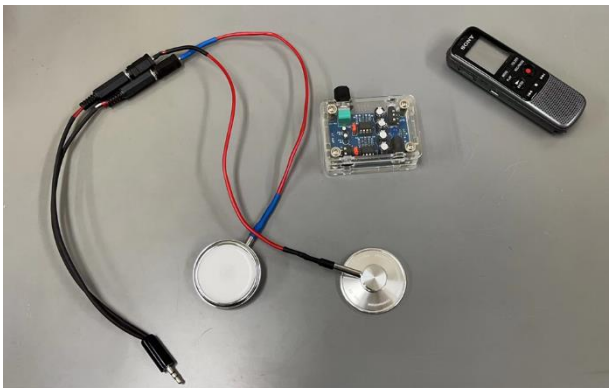

Figure 2.1.3 A simplified knee joint sound measurement system

More modular components were used in the system, such as a sound amplifier and digital recorder. The biggest advantage of this system is that the manufacturing cost is extremely low without any reduction in the quality of VAG signal collection. This simplified system is affordable in hospitals, health centers, or at home to confirm the health of the knee.

2.2 A Vibration-based VAG Signal Collection Devices

Although VAG signals based on stethoscope-microphone systems are more cost-effective in the signal collection process, they also have limitations. The limitation comes from the stethoscope, where the construction of a typical stethoscope consists of three parts, bell, diaphragm, and tube. Although stethoscopes are constantly evolving, the diaphragm has changed little due to the limitations of the material. Because of this, the vibration frequency of the diaphragm in the stethoscope constrains the upper limit of the VAG signal sampling rate[71]. Therefore, a vibration-based VAG signals were used in this study.

2.2.1 Piezoelectric and VAG Sensor

The conversion of vibration signals into electrical signals is mainly done through piezoelectric materials, such as piezoelectric ceramics. A piezoelectric material possesses a perovskite crystalline structure. A material with typical piezoelectric phenomena and perovskite crystalline structure is lead zirconate titanate〔$Pb(Zr \cdot Ti)O_3$〕, abbreviated as PZT. Typical properties and applications of PZT are listed as follows:

(1) Voltage generation (direct piezoelectric effect): Piezoelectric ceramic generates a voltage corresponding to applied mechanical stress. This is generally used as energy harvesters, gas ignition, and sensors to detect pressure, acceleration, and angular velocity.

(2) Displacement generation (inverse piezoelectric effect): Piezoelectric ceramic generates a displacement corresponding to an applied voltage. This is often employed for linear actuator applications such as piezo injectors, nano-positioning, and antivibration systems. The advantages of piezoelectric ceramics compared to electronic and hydraulic type actuators are the fast response, large generation pressure, and highly accurate operation resonance.

(3) Resonance: Piezoelectric ceramic has intrinsic vibration with respect to shape and size. When applying an electric field with a certain frequency, so-called resonant frequency, the piezoelectric ceramics vibrates with a large amplitude showing the maximum current flow. This characteristic is used for ultrasonic vibrators, for example, washing machines, humidifiers, sonar, electrical signal filters, and ultrasonic motors.

The device makes use of the very nature of (1) above to make a sensor for VAG signal collection. Although there are numerous piezoelectric ceramics that can convert vibration signals into electrical signals, we finally chose piezoelectric diaphragms (MURADA) as the base component of the sensor. The piezoelectric diaphragm consists of a piece of metal plate and a piece of piezoelectric ceramic with an insulating glue sandwiched between them. The vibration of the knee joint deforms the diaphragm, and an electrical potential develops between the piezoelectric ceramic film and the metal film. The diaphragm is shown below.

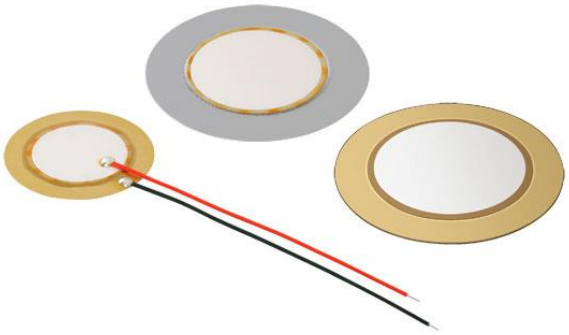

Figure 2.2.1 Piezoelectric diaphragms

Piezoelectric diaphragm into a sandwich structure, the middlemost is piezoelectric ceramic, covered with a thin layer of electrodes. Underneath is a metal plate, and the appropriate sampling frequency can be selected according to the metal-like thickness and diameter. The metal plate is usually brass or nickel alloy, which allows to make it extremely thin. The most commonly used sensor for this device is the model 7BB-35-3L0, which can collect vibration signals up to 3000Hz.

Although diaphragm-type sensors are somewhat less sensitive, they have advantages for collecting biomedical signals that other types of sensors do not have. The first advantage is in its shape. Since it is thin enough and rounded, it fits the skin better and does not easily hurt the participants when collecting VAG signals. The second advantage is the simplicity of the construction, which allows the selection of the piezoelectric ceramic material and the metal sheet material according to the sampling rate. With this sensor, a clearer signal can be collected even outdoors.

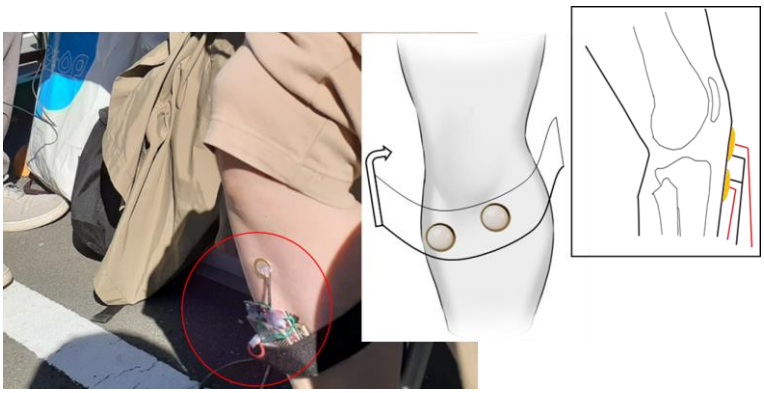

Figure 2.2.2 Collecting VAG signals outdoors via piezoelectric diaphragms

2.2.2 Angle Sensors

In addition to the vibration sensor, there is an angle sensor as an auxiliary. The sensor is designed to measure the angle between the femur and tibia, the angle between flexion and extension to roughly determine the location of knee damage.

The principle of angle measurement based on acceleration is very simple. In the initial position, the

acceleration sensor is perpendicular or parallel to the ground. At this time, the acceleration sensor will be influenced by gravity. When the angle changes, the acceleration sensor makes an angle with gravity, and this angle can be calculated according to the trigonometric equation. Since the acceleration of gravity is constant, the change in the acceleration sensor measurement is the change in angle.

$$Angle = \arccos(\frac{a}{g}) \qquad \text{Equation 2.2.1}$$

2.2.3 Electronic Circuits

The collected signals need to be converted into data after a suitable electronic circuit, and the circuit design is the key to the success of the device. In order to make the device meet the safety and wearability, this device is battery-powered, and the design idea is shown in Figure 2.2.3.

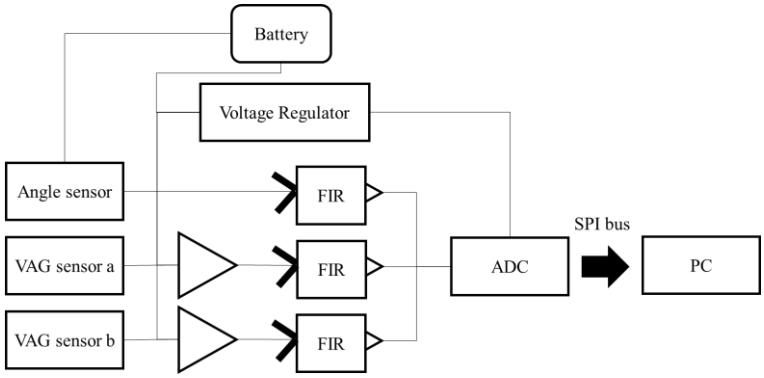

Figure 2.2.3 A schematic diagram of the signal collection circuit

From the above figure, it can be seen that there are three independent signals constituting three channels, of which the VAG signal occupies two channels, and the angle signal occupies one channel. The VAG signal is amplified by the amplifier by a certain multiple and then passed through a h bandpass filter to remove the effects of body motions. To better handle the noise in the VAG signal acquisition circuit, the bandpass filter is used to calculate the RLC constant from f0 pass center frequency, Q (quality factor), and ζ attenuation ratio.

Since the angle signal obtained from the acceleration sensor has sufficient potential, no amplification is required, but a low-pass filter is still needed to remove high-frequency noise. The three-channel signal is then passed through an analog-to-digital converter (ADC) with a sampling rate of 2000 Hz, and the data is saved as a time series on a computer via a Serial Peripheral Interface (SPI) capture card.

In addition, both the ADC and the amplifier are fixed by the regulator to operate at the rated voltage. There are also several protection circuits in the circuit, which are omitted from the description here.

2.2.4 Device shape design and Bonding Method

Since the device mainly measures the frictional vibrations caused by knee flexion and extension when the participant sits down and stands up, as shown in Figure 2.2.4 Therefore, the light weight and

wearability of the device becomes very important.

In addition to sitting and standing, the swing of the lower leg also generates the VAG signal. So, separating the angle sensor in space from the main control (master) chip is the design concept of this study. In this way, each of the three sensors is connected to the master chip via three Bayonet Neill Concelman (BNC) connectors, and the master chip is connected to the computer via mini-USB.

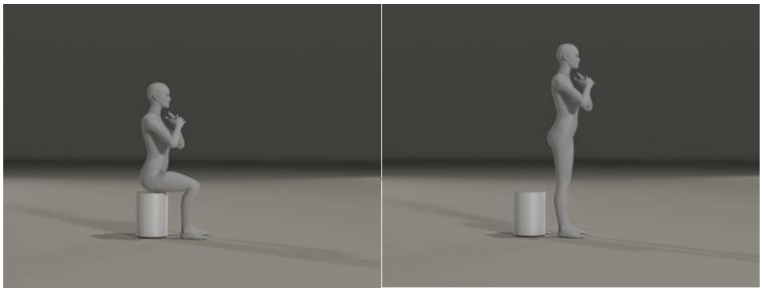

Figure 2.2.4 Sitting and standing generate VAG signals

A complete set of hardware devices is shown in Figure 2.2.5. This study uses a thin wooden board to hold the circuit board in place, ensuring lightweight and insulation at the same time so that participants are in a safe state at all times. Compared to metal boards, wooden boards have the added benefit of reducing the risk of a cold touch and allergies when in contact with the participant's skin. The shell of the device is made by 3D printing using polylactic acid material with space reserved for bonding.

Figure 2.2.5 The VAG signal collection device developed in this study and bound to the participants.

2.2.5 The Interface of the VAG Signal Collection System

For the collection of VAG signals, a software system is required in addition to the hardware system. In this study, a graphical user interface (GUI) was developed based on the JAVA programming language and processing framework, as shown in Figure 2.2.6. With this system, different USB ports and sampling speeds can be changed, and the data can be named by a rule and saved as a file in comma separated values (CSV) format. The GUI is currently version 1.1 and will continue to be optimized in

the future as the hardware system is upgraded[72].

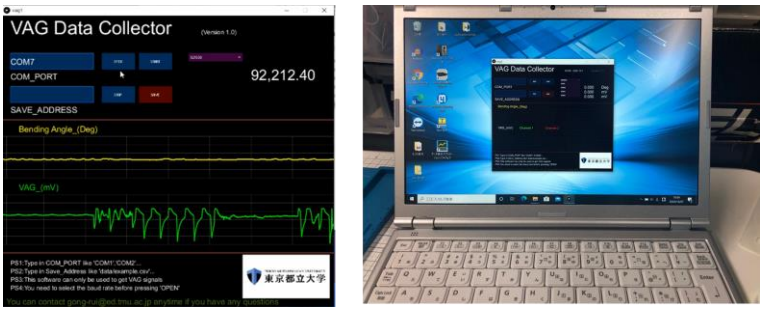

Figure 2.2.6 A GUI for a VAG data collector

2.2.6 Conclusion

Although the device has been successfully applied to the VAG signal collection experiments, it still has some limitations waiting for improvement. First of all, the sampling rate of this system is only 2000Hz, which is affected by the operating frequency of the master control chip, and the ADC chip also needs to be replaced with a higher sampling accuracy. Second, the piezoelectric diaphragm used as a VAG sensor is no longer quite adequate for sensing more details of vibrations, and a piezoelectric sensor with soft material is urgently needed to be developed.

Chapter3

Application of VAG signals in normal and abnormal knees

3.1 Knee Osteoarthritis Detection based on the Combination of Empirical Mode Decomposition and Wavelet Analysis

3.1.1 Introduction of this Section

Osteoarthritis (OA) represents a progressive degradation process and usually occurs in the knee joint because this joint supports almost the entire weight of a human body, and also provides motion during walking [73]. Therefore, the knee is the most vulnerable, both to the injuries and OA in the human body. The knee OA is an idiopathic disease characterized by a degeneration of articular cartilage. A breakdown of the cartilage matrix can lead to the development of fibrillation and fissures, appearance of gross ulcerations, and disappearance of the full thickness surface of the joint. These processes are accompanied by changes in the bone due to osteophyte formation and thickening of the subchondral plate [74]. The pathological manifestations of the joints are osteophyte formation and narrowing of the joint space [75,76]. The knee OA mainly occurs in the elderly [77]. About 30% of people over the age of 65 suffer from knee OA [78]. Moreover, the incidence of knee OA is higher in females than in males, and its possibility increases with age. However, the knee OA is not limited to the elderly; a significant proportion of OA cases are associated with trauma and obesity; a large number of OA cases are idiopathic [79].

The most common symptom of knee OA is joint pain. The pain tends to worsen with activity, specifically following a period of rest that has been known as the gelling phenomenon [80]. Early detection of knee OA helps to control the disease via surgery or physical therapy [81]. At present, knee OA is mainly diagnosed via general clinical examination including the analysis using the X-ray, computed tomography, magnetic resonance imaging (MRI), arthroscopy, and vibroarthrographic (VAG). The detection of the knee OA using the X-ray images is the most common method, and it is based on the Kellgren–Lawrence (KL) classification grades. The KL system is a validated method for classifying the individual joints into one of the five classes, where the Class 0 represents normal joint, and Class 4 denotes the most severe radiographic disease [82]. Since the differences before Grade 3 are extremely limited, doctors can have different assessments of the OA and hence, draw different conclusions regarding its presence and severity. On the other hand, the MRI technology can be susceptible to the defection of the articular cartilage surface and soft tissue. The cartilage MRI diagnosis remains dependent on visual assessments, so there is a risk that small early OA lesions may

not be detected [83]. Further, arthroscopy is a rod-shaped optical instrument with a diameter of about 5 mm for observing the internal structure of joints. It represents an endoscope used to diagnose and treat joint diseases. Arthroscopy is equipped with a lens at the end of a thin tube. The diagnosis is conducted inserting the thin tube into a joint, and then the structure inside the joint is displayed on a monitor; thus, the cartilage inside the joint can be directly observed. Although arthroscopy improves the accuracy of the OA diagnosis, it should be avoided since it is invasive and can cause complications [84].

The traditional diagnosis of joint disease is based on listening to the sound and feeling the vibrations [85]. Due to the recent development of advanced technologies, such as digital signal processing and machine learning, the measurement and analysis accuracy of VAG signals has dramatically improved [86]. There has been a new technology based on acceleration instead of palpation, where the diagnosis is conducted analyzing the VAG signals collected during the knee flexion and extension motion. Compared with the healthy patients, those with articular cartilage, meniscus, and ligament have the VAG signal with unique characteristics in time series. However, these characteristics are surrounded by noise. Even when the noise is reduced, a part of the signal is still lost. Since the generation mechanism of the VAG signals is complex and random, the range of the signal-to-noise ratio of these signals cannot be determined a priori. Therefore, we choose the empirical mode decomposition (EMD) for signal preprocessing. For the time–frequency analysis of the VAG signal, different from commonly used traditional Fourier transform (FT) and short-time-Fourier-transform (STFT), in this work, we use the wavelet transform. Namely, the FT decomposes a signal into its frequency components, so the information in the time domain is lost, while the STFT provides the frequency components in the local time intervals of fixed duration. However, using both of them, it is very difficult to analyze signals that contain non-periodic and fast transient features, which is why we use the continuous wavelet transform (CWT) that can provide good time resolution and relatively poor frequency resolution at high frequencies and good frequency resolution and relatively poor time resolution at low frequencies [87].

In this paper, a combined method of the EMD and CWT is proposed to improve the diagnostic accuracy of knee OA.

3.1.2 Methods

3.1.2.1 VAG signal acquisition

As shown in Figure. 6.1.1, the VAG signal can be recorded using an accelerometer. The procedure is as follows: the sensor is attached to the subject's tibia where 15cm under from the patella-center using medical double-sided adhesive tapes; the subject is required to hold arms tightly and legs open from shoulder width sitting on a height of 420 mm chair without armrests, stand up as steady as possible in 2 seconds [84]. The purpose of holding arms tightly is to reduce the effects of the upper

limb shake when the subject is standing up. The accelerometer sensor measures the acceleration and deceleration amplitude of the knee joint during the course of flexion-extension. Moreover, during the measurement of the VAG signal, an electronic goniometer is used to measure the bending angle of the knee joint.

We collected the raw signal by an accelerometer sensor (BW21SG2, Fuji Ceramics), a conversion connector (BNCP-ZR, Fuji Ceramics), and pre-amplifier (CA201, Fuji Ceramics) with a sampling rate of 25 kHz. The signal was digitized with a resolution of 12 bit per sample using a PC oscilloscope (Picoscope 4424, Pico Technology) and the Picoscope 6 software (Pico Technology). Each subject is measured 4 times, and the available data closest to 2 seconds is selected.

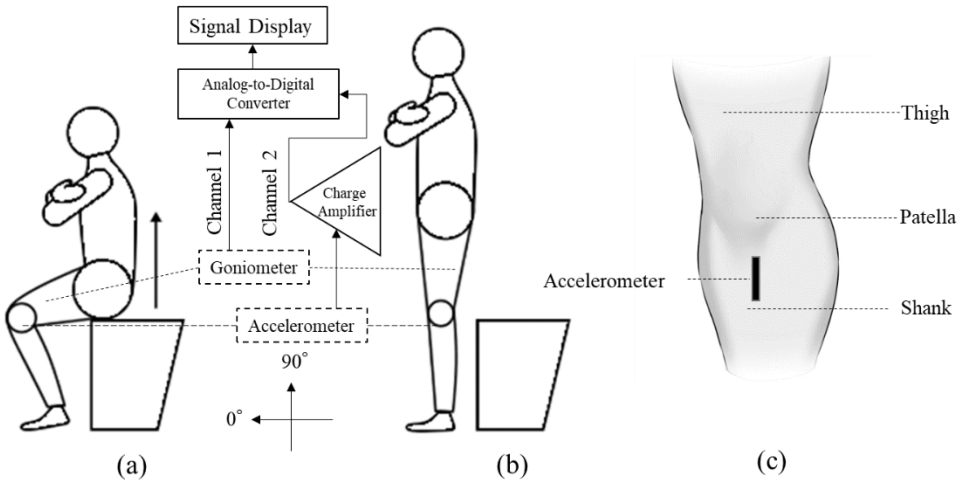

Figure 3.1.1 The knee joint VAG data acquisition setup.

Channel 2 records the VAG signal at the middle position of the patella; Channel 1 records the goniometer voltage (angle) information. (a) sitting position with arms held tightly (b) standing position with arms held tightly. (c) shows the front view of the position of accelerometer

3.1.2.2 VAG signal preprocessing and analysis

In clinical applications, the use of VAG signals for computer-assisted diagnosis and analysis of knee joint pathology signal requires exceptional high quality and accuracy. However, since the sensor is attached to the skin on the patella surface, it can acquire several different types of signals, including the mechanomyogram (MMG) and electromyogram (EMG) signals, ambient interference, and random noise [88]. Due to the participation of several muscles in the sitting–standing movement, the EMG and MMG signals are readily induced by the flexion and extension movements [89].

3.1.2.2.1 Extraction method for the comparison set features

EMD is a method for the analysis of nonlinear and nonstationary signals [90]. The EMD decomposes a given signal into a set of intrinsic mode functions (IMFs) using a sifting process according to the algorithm mentioned in [91]. Accordingly, signal $x(t)$ is adaptively decomposed into the IMFs $c_i(t)$, $i = 1, 2, \cdots, k$ and residue $r(t)$, as follows:

$$x(t)=\sum_{i=1}^{k}c_i(t)+r(t)$$ Equation 3.1.1

where k denotes the number of IMF functions. The residue $r(t)$ reflects the average trend of a signal $x(t)$ or a constant value. The upper envelope $E_u(t)$ and lower envelope $E_l(t)$ are obtained using the local maxima and minima of the signal $x(t)$, respectively. The mean of the upper and lower envelope is expressed as

$$m_1(t)=\left(E_{u1}(t)+E_{11}(t)\right)/2$$ Equation 3.1.2

By subtracting the mean from the original signal, we have

$$h_1(t)=x(t)-m_1(t)$$ Equation 3.1.3

Then, it is checked whether $h_1(t)$ satisfies the conditions for the IMFs. The above steps are repeated until $h_1(t)$ is an IMF. The first IMF after n iterations is expressed as

$$c_1(t)=h_{1(n-1)}(t)-m_{1n}(t)$$ Equation 3.1.4

The first residue $r_1(t)$ can be calculated as

$$r_1(t)=x(t)-c_1(t)$$ Equation 3.1.5

Repeat the whole algorithm with $r_1(t),r_2(t),\cdots$ until the residue is a monotonic function. After k iterations $x(t)$ is decomposed according to Equation 3.1.1.

3.1.2.2.2 Reconstructed signal

The value and noise of the raw signal are distributed in the IMFs; thus, it is necessary to remove the noise to reconstruct the signal. In this paper, the mean squared error (MSE) and peak signal-to-noise ratio (PSNR) measures are used to select an IMF and then reassemble the signal.

The MSE assesses the quality of an intrinsic mode function $c_i(t)$, and is expressed as

$$\mathrm{MSE}\left(c_i(t)\right)=\frac{1}{n}\sum_{i=1}^{n}\left(x(t)-c_i(t)\right)^2$$ Equation 3.1.6

The PSNR (in dB) is defined using the MSE as

$$PSNR\left(c_i(t)\right)=20\cdot\log_{10}\left(\frac{PPV\left(c_i(t)\right)}{\sqrt{MSE\left(c_i(t)\right)}}\right)$$ Equation 3.1.7

where $\mathrm{PPV}\left(c_i(t)\right)$ of an intrinsic mode function $c_i(t)$ is defined as the difference between its maximum positive peak and minimum negative peak that is given by

$$\mathrm{PPV}(c_i(t)) = \mathrm{Max}(c_i(t)) - \mathrm{Min}(c_i(t)) \qquad \text{Equation 3.1.8}$$

Generally, the filters perform denoising process through the subtraction operation. For instance, a median filter of a time series will smoothen the signal and lose some of them. The disadvantage is that it is difficult to analytically treat the effect of a median filter. This denoising method is not suitable for time series such as VAG signals when the high-frequency features should be classified. Thus, in this work, addition is chosen to reconstruct the signal. The two smallest MSE values and the largest PSNR values of all the IMFs, if they are the same, then select the next one. These three IMFs are chosen. They are reconstructed, and the signal $y(t)$ is obtained.

3.1.2.3 Feature extraction

3.1.2.3.1 Feature extraction using CWT

To observe the frequency characteristics, a CWT is performed on the reconstructed signal. The CWT transforms the reconstructed signal $y(t)$ into a function $D(s, p)$ of two real variable s and p that is given by

$$D(s,p) = \int_{-\infty}^{\infty} y(t)\psi_{s,p}(t)dt \qquad \text{Equation 3.1.9}$$

Function $\psi_{s,p}(t)$ in Equation 3.1.9 is referred to as the wavelet function, and is defined by translating along the time axis and stretching a so-called "mother wavelet" function $\psi(t)$ that is expressed as

$$\psi_{s,p}(t) = \frac{1}{\sqrt{s}}\Psi\left(\frac{t-p}{s}\right) \qquad \text{Equation 3.1.10}$$

where s is the scale, and p is the shift of the wavelet in the time domain. The wavelets can be real or complex functions. For the application studied in this paper, a real wavelet is used. The Morlet wavelet is given by

$$\Psi(t) = e^{-\frac{t^2}{2\sigma^2}}\cos(2\pi f_0 t) \qquad \text{Equation 3.1.11}$$

where σ denotes the approximate bandwidth and f_0 is the center frequency. Although the device supports frequencies up to 2000 Hz, the sample rate of the signal is 25000 Hz, so we decided to divide the frequency domain to 250 scales for 100Hz per scale.

The CWT coefficients x are represented using a matrix with rows and columns and times and scales. In order to facilitate the following calculations, x needs to be normalized in the range (0,1); the normalized matrix is denoted as Y, which is expressed as

$$Y = \frac{X - X_{\min}}{X_{\max} - X_{\min}} \qquad \text{Equation 3.1.12}$$

where $X_{\min}$ and $X_{\max}$ denote the minimum and maximum value of x, respectively. Thus, the CWT

coefficients γ in the intervals of 100 Hz below the frequency of 2500 Hz are summarized into a feature.

3.1.2.3.2 Feature extraction in the spatiotemporal domain

To detect any difference in a reconstructed signal from the abnormal and normal, the features need to be extracted in the spatiotemporal domain that include the skewness and kurtosis of the autocorrelation function (ACF) values. The ACF $A(\tau)$ of the reconstructed signal $y(t)$ is calculated according to the following formulas:

$$A(\tau) = \frac{1}{N-\tau} \sum_{i=0}^{N-\tau-1} (y(i)y(i+\tau)) \qquad \text{Equation 3.1.13}$$

where N is the number of samples.

$$kurtosis = \frac{\mu^4}{\sigma^4} \qquad \text{Equation 3.1.14}$$

where μ^4 denotes the fourth moment about the mean μ of $A(\tau)$, and σ denotes the standard deviation of $A(\tau)$.

$$skewness = \frac{1}{N} \sum_{i=1}^{N} \left(\frac{y_i - \mu}{\sigma} \right)^3 \qquad \text{Equation 3.1.15}$$

3.1.2.4 Least squares support vector machine (LSSVM) classifier

The LSSVM method introduces the idea of a square sum of errors into the objective function of the standard SVM, where a training data consisting of n samples is considered. $\text{Train} = \cdot\{(u_i, v_i) | i \cdot = 1,2,\cdots,n\}$, where $u_i \in R^d$ denotes the input data and $v_i \in R$ is the output data. A nonlinear mapping $\varphi(\bullet)$ is employed to project the input-sample space to the feature space $\varphi(u) = \{\varphi(u_1),\cdots,\varphi(u_i)\}$ and construct the following optimal linear decision function [92]:

$$y(u) = \omega^T \varphi(u) + \beta \qquad \text{Equation 3.1.16}$$

Using the structural risk formula, we have:

$$R = \frac{1}{2} \| \omega \|^2 + CR_{emp} \qquad \text{Equation 3.1.17}$$

The weight vector ω and offset β can be calculated using Equation 3.1.16. In Equation 3.1.17, C and R_{emp} denote the penalty factor and loss function, respectively. In the LSSVM, the loss function is always equal to the quadratic loss function, which is expressed as

$$R_{emp} = \sum_i \xi_i^2 \qquad \text{Equation 3.1.18}$$

where ξ_i denotes the deviation degree of a misclassification sample from the ideal sample. Then, obtaining the solutions of ω and β is equivalent to solving the optimization problem given by

$$\min R = \frac{1}{2}\| \omega\|^2 + C\sum_{i=1}^{n}\xi_i^2 \qquad \text{Equation 3.1.19}$$

$$\text{s.t. } v_i = \omega^T\varphi(u_i) + \beta + \xi_i, \{i = 1,2,\cdots,n\} \qquad \text{Equation 3.1.20}$$

By introducing the Lagrangian multiplier $g = \{g_1, g_2, \cdots, g_i\}$ into Equation 3.1.19 and Equation 3.1.20, we get

$$\begin{aligned}&\mathcal{L}(\omega,\beta,\xi_i,\alpha) = \frac{1}{2}\| \omega\|^2 \\ &+C\sum_{i=1}^{n}\xi_i^2 - \sum_{i=1}^{n}\left(g_i\left(\omega^T\varphi(u_i) + \beta + \xi_i - v_i\right)\right)\end{aligned} \qquad \text{Equation 3.1.21}$$

Next, we calculate the derivative of every factor in Equation 3.1.21. To eliminate ω and ξ, we introduce the equations $\omega = \sum_{i=1}^{n} g_i\varphi(u_i)$ and $\xi_i = \frac{g_i}{2C}$ into Equation 3.1.21. Then, it can be written that

$$v_i = \sum_{j=1}^{n}\left(\alpha_j \cdot <\varphi(u_j), \varphi(u_i)>\right) + \beta + \frac{g_i}{2C} \qquad \text{Equation 3.1.22}$$

Suppose that there exists a kernel function $K(u_i, u_j) = <\varphi(u_i), \varphi(u_i)>$ that satisfies the Mecer condition[93]. Then, Equation 3.1.22 can be re-written as

$$v_i = \sum_{j=1}^{n}\left(g_j K(u_i, u_j)\right) + \beta + \frac{g_i}{2C} \qquad \text{Equation 3.1.23}$$

Solving Equation 3.1.23, the model parameters β and $[g_1, g_2, \cdots, g_n]^T$ are obtained. Then, the decision function of the LSSVM is expressed as

$$v(u) = \text{sgn}\left[\sum_{i=1}^{n}\left(\alpha_j K(u, u_i)\right) + \beta\right] \qquad \text{Equation 3.1.24}$$

As it is well-known, different types of kernel function $K(\mathrm{u}, \mathrm{u}_i)$, such as the polynomial kernel function, sigmoid kernel function, linear kernel function, and Gaussian Radial Basis Function (GRBF), lead to different LSSVM performances. In this work, the Gaussian RBF is used because there is only one parameter compared with the other kernel so that it will work well in practice and is relatively easy to calibrate[94]. The Gaussian RBF kernel is given by

$$K(u, u_i) = e^{-\frac{|u-u_i|^2}{2\varepsilon^2}} \qquad \text{Equation 3.1.25}$$

Since $|u - u_i|$ is always a positive value, kernel achieves a maximum output when $|u - u_i| = 0$, and then, approach to zero as $|u - u_i|$ increases. The speed of this approach depends on ε, it is faster at smaller ε and vice versa. Thus, the factor ε should be optimized, and we use a heuristic algorithm to determine its optimal value.

3.1.2.5 Classification and ensemble systems

To classify the reconstructed signal as normal or abnormal by an LSSVM classifier, a large set of

normal and abnormal signals was used in the training process. The training was performed using the feature vectors having the two features extracted from the ACF of the reconstructed signal: ① kurtosis of ACF, ② skewness of ACF with four CWT coefficient features extracted from the frequency bands, ③ CWT coefficient in the range of 100–200 Hz, ④ CWT coefficient in the range of 200–500 Hz, ⑤ CWT coefficient in the range of 500–1000 Hz, and ⑥ CWT coefficient in the range of 1000–2500 Hz.

Table 3.1.1Feature sets

Feature set	Feature of reconstructed signal
G_a	①②③④⑤⑥
G_b	①②
G_c	③④⑤⑥
G_d	①②③④
G_e	①②⑤⑥

The VAG signals were reconstructed using 25 patients suffering from knee OA and 26 young and healthy people. The features were extracted using the presented algorithm. We combined the six features into five sets to verify their accuracy, as presented in Table 3.1.1. In these five sets of features, 10 data were randomly selected for the normal and abnormal signals for the LSSVM training. The remaining data were used for testing.

Since the data amount was not enough, the sensitivity and specificity of each set of features were calculated using 100 simulations. In each LSSVM simulation, training and test data were randomly selected. To evaluate the accuracy of each group of features after mechanical learning, the receiver operating characteristic curve (ROC curve) was used. The ROC analysis was used as it can provide essential information about diagnostic test performance; namely, the closer the apex of the curve toward the upper left corner, the higher the discriminatory ability of the test i.e., the true-positive rate is high, and the false-positive [1-*specificity*] rate is low[95]. The area under the ROC curve (AUC) can provide a way to measure the accuracy of a diagnostic test. The larger the area, the more accurate the diagnostic test[96].

The AUC of the ROC curve, where $FP = (1 - specificity)$ and $ROC(\mathrm{FP})$ is sensitivity, was calculated using

$$AUC = \int_0^1 ROC(FP)d(FP) \qquad \text{Equation 3.1.26}$$

The classification accuracy of commonly used AUC ranging in the diagnostic test is summarized in Table 3.1.2.

Table 3.1.2 Classification accuracy using AUC for a diagnostic test.

AUC range	Classification accuracy
0.9 < AUC < 1.0	A (Excellent)
0.8 < AUC < 0.9	B (Good)
0.7 < AUC < 0.8	C (Worthless)
AUC < 0.7	D (Not good)

Besides, the classification accuracy is mostly expressed as

$$Accuracy = \frac{TP + TN}{TP + TN + FP + FN} \qquad \text{Equation 3.1.27}$$

where TP denotes the true-positive, TN denotes the true-negative, and FN denotes the false-negative.

3.1.3 Results

We used a median filter to compare the denoised signal with the reconstructed signal, as shown in Figure. 6.1.2.

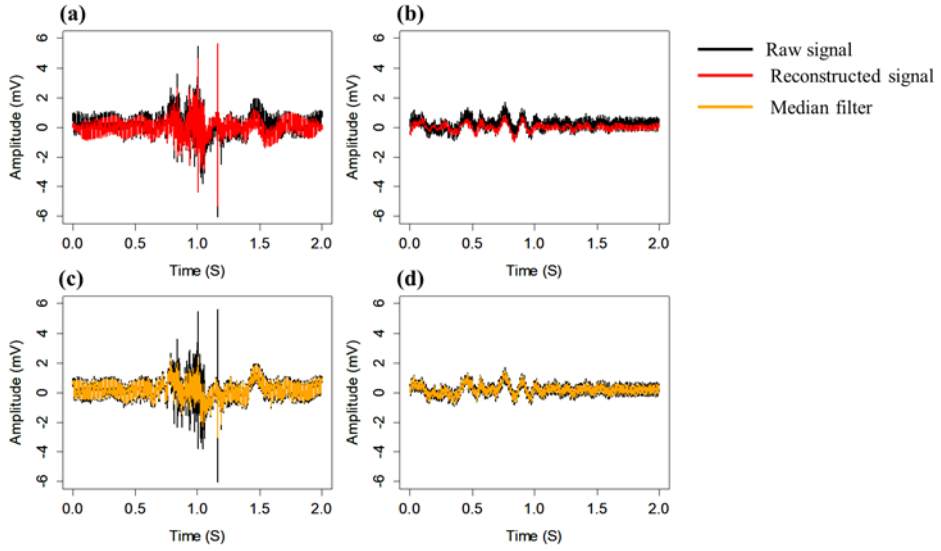

Figure 3.1.2 The comparison of the original, denoised, and reconstructed signals.

The black line denotes the original signal, the red line denotes the reconstructed signal, and the blue line is the signal denoised with the median filter: (a), (c) the knee joint VAG signal of a patient (female) with Grade III knee OA; (b), (d) the knee joint VAG signal of a healthy subject

From the perspective of the dynamic time warping calculation, the similarity of the signal reduced by the median filter was better than that of the reconstructed signal. The DWT distances of the reconstructed signal of the patient with knee OA and the healthy subjects were 9370mV and 6725 mV, respectively. The DWT distances of the signal denoised with the median filter of the patient with knee

OA and the healthy subject were 7292 mV and 4197 mV, respectively. However, as shown in Figure. 3.1.2, obviously, the reconstructed signal retains more peak details to facilitate feature extraction in the next step.

As shown in Figure. 3.1.3, there were some differences in the ACF features between the healthy subjects and patients with knee OA. However, a part of them overlapped; thus, it was difficult to classify based on just the ACF features.

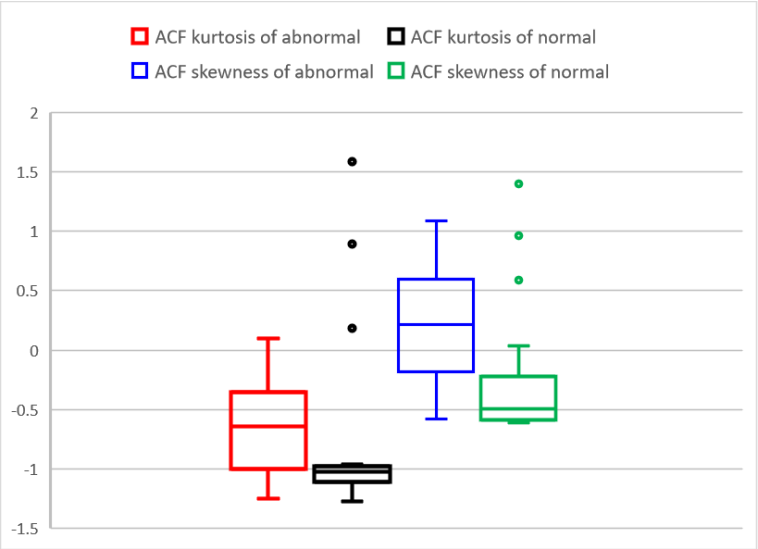

Figure 3.1.3 The box plot of ACF features.

The red box denotes the ACF kurtosis of the patient (female) with Grade III knee OA; the black box denotes the ACF kurtosis of the healthy subject; the blue box denotes the ACF skewness of the patient (female) with Grade III knee OA; the green box denotes the ACF skewness of the healthy subject.

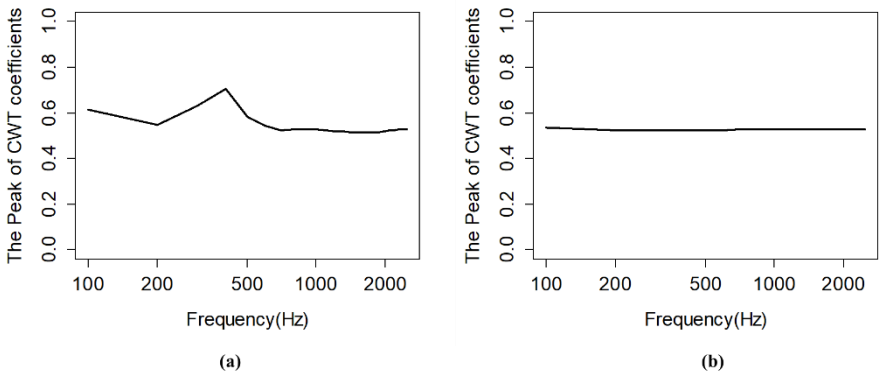

Figure 3.1.4 The horizontal axis denotes the frequency, and the vertical axis denotes the peak of the CWT coefficients: (a) the patient (female) with Grade III knee OA, (b) the healthy subject

Using the CWT calculation, we obtained the peak value of the CWT at each frequency range of the flexion and extension actions as shown in Figure. 3.1.4. The ratios of the CWT coefficients average

values of the 100–200 Hz interval, 200–500 Hz interval, 500–1000 Hz interval, and interval above 1000 Hz to the overall average value were calculated as features. The ratio of the healthy people was higher in the low-frequency band, while that of patients with knee OA was higher in the high-frequency band.

The classification accuracy rate in the percentage of the Gaussian RBF kernel LSSVM with the G_a feature set was 86.67% that was higher than the accuracy obtained using other feature sets using the same classifier. According to the results presented in Table 3.1.3, the AUC obtained using the G_a feature set was 0.9965 with a standard error (SE) of 0.02156 as illustrated in the Figure. 3.1.5.

Table 3.1.3 Classification results of the different feature sets and ensemble systems on the Gaussian RBF kernel LSSVM.

Feature set	Accuracy (%)	AUC	SE
G_a	86.67	0.9965	0.02156
G_b	76.83	0.9744	0.02465
G_c	80.22	0.9533	0.01993
G_d	74.19	0.8407	0.02421
G_e	77.98	0.8935	0.0368

Referring to the Table 3.1.1 and Figure. 3.1.4, the superiority of G_a ensemble in the diagnostic performance was prominent, with the highest overall accuracy, the best AUC value, and the second-lowest SE value; G_b had the second highest AUC (0.9744) and SE values, but the accuracy (76.83%) was not very high. Although G_c had the lowest SE value, the accuracy and AUC values were on the intermediate levels.

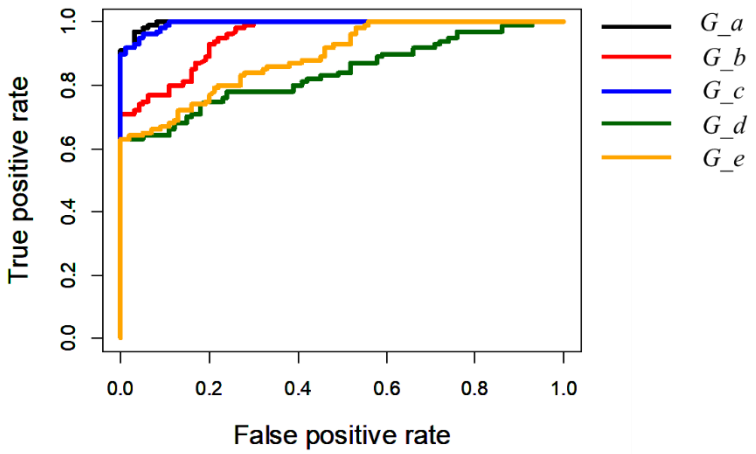

Figure 3.1.5 The ROC curves provided using the five feature sets with the Gaussian RBF kernel LSSVM classifiers in the ensemble ($p < 0.002$)

In the ensemble experiments, the highest accuracy provided using the feature set was 86.67% (G_a), whereas, the lowest was only 74.19% (G_d). On the other hand, the highest AUC provided was 0.9965 (G_a), whereas, the lowest was only 0.8407 (G_d).

According to the analysis, G_d provided the worst result. However, the accuracy was higher than 70%, the AUC value exceeded 0.8, and it was evaluated as B (good). However, the discrimination of the feature sets in the low-frequency band was not very good, and it was worse than that of the feature sets in the high-frequency band. The best result had the accuracy of more than 85%, and the AUC value, higher than 0.99 that was evaluated as A (excellent).

3.1.3 Discussion

These accuracy rates of G_a are not lower than those we can find in the published research works, where the values obtained for accuracy are in the range of 84–89%. Moreover, the AUC values of our feature sets are higher, the highest value even exceeds 0.99[97,98].

The reason for the good result of G_a was the CWT coefficients of the three frequencies, the low, medium, and high, were applied as features. It can be seen in Figure. 3.1.4 that when only ACF features were missing, the impact on the results was not great. However, when the features of one of the frequency bands were missing, the accuracy and AUC values were greatly reduced, specifically in the high-frequency band.

In view of the excellent performance of the Gaussian RBF kernel LSSVM method, using G_a feature set, we used this method to determine the knee OA level, i.e., to distinguish Grade III and Grade IV OA. The results are presented in Figure. 3.1.6, where it can be seen that the sensitivity rate was 48% and the specificity rate was 98%, and the AUC value was only 0.762. The percentages of correctly predicted Grade III and IV knee OA were 4.0% (PV−) and 34.7% (PV+), respectively, which was worse than blind guessing. The reason for such results could be scarce amount of training data, resulting in insufficient machine learning. On the other hand, all the VAG signals corresponded to the late stage of knee OA, so the similarity between Grade III and IV knee OA was too high.

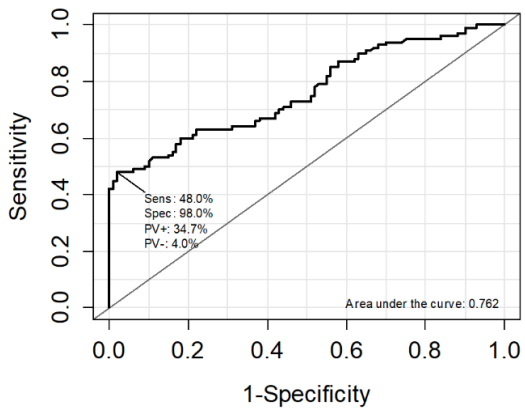

Figure 3.1.6 The ROC curve analysis for prediction of Grade III and IV knee OA

Although we got a good result, we still need to discuss how we can use the method to diagnose

patients in early stages of knee OA. As the number of patients with early stages of knee OA rarely, we collected only one VAG signal from Grade II patient. Even though this patient had more pain than Grade III, the X-ray diagnosis report was only Grade II. That's why this patient was found in early stage. Thus, we put the data into the machine learning test and got the 56.22% possibility of healthy ($P<0.01$). The result was obviously false negative, because of the signal collected by the sensor is very similar to the healthy.

That's very difficult to find the cause from overly sparse samples, and mostly the pain in the early stage is inconspicuous, easily overlooked. Nevertheless, we still suspect that it is likely that the frequency range of CWT coefficients is insufficient because we did not study the CWT coefficients of reconstructing signals by EMD below 100Hz and above 2000Hz. In addition, some articles have proposed to use the features of high frequency or ultra-high frequency to improve classification accuracy. This consistent with our finding that the high frequency feature set has a more significant influence on classification.

The reason we don’t use higher frequency in this paper is we will have a heavy calculation burden in reconstruct signal process with the increase of the sampling rate, and there is some serious mode mixing phenomenon in EMD. Next, we are going to try to solve the mode mixing problem by add white noise into the original signal and enhance overall computing speed by a perfect algorithm to extract features from a wider frequency range.

3.1.4 Conclusions of this Section

In this study, the knee VAG signals that were obtained using an accelerometer and a goniometer were used in the knee OA detection. The VAG signals were input into a personal computer and reconstructed by the EMD. To obtain the feature set, the autocorrelation function and continuous wavelet transform (CWT) process were applied to the reconstructed signal. Finally, the classification was performed using the LSSVM and the overall evaluation was performed using the ROC curve. The results showed that high accuracy and AUC value were achieved. Consequently, a combined EMD and CWT analysis method of the knee VAG signal that can monitor the knee joint pathology provides an economic alternative to the osteoarthritis patients. However, further research on OA grade classification and its early-stage diagnosis is needed.

Chapter4

Application of VAG signals in aged and young knees

4.1 Vibroarthrographic Signals for the Low-cost and Computationally Efficient Classification of Aging and Healthy Knees

4.1.1 Introduction of this Section

Knee pain is common in older age and often leads to a limited range of motion or an inability to bear weight on the knee, typically leading to knee disorder [99]. If the knee disorder is not treated in time, it can deteriorate into osteoarthritis (OA), which is the fourth leading contributor to overall years lived with disability (YLDs), accounting for 3.0% of total global YLDs [100]. The root cause of knee disorder is knee aging, which can be divided into natural aging and early aging. The prevalence rates of knee disorders caused by early aging differ between urban and rural populations, especially in places with low economic development [101]. Because of the lack of professional medical imaging equipment and technical expertise in rural hospitals, knee joint disorders caused by aging are more difficult to diagnose and prevent in such settings, and they thus more commonly deteriorate to OA, ultimately leading to disability [102]. There is no cure for knee OA, but if doctors diagnose aging in the knee at an early stage, the deterioration can be slowed by an anti-aging defense method.

Vibroarthrographic (VAG) signal analysis technology has gained interest as a low-cost diagnostic method for knee joint disorders [97]. VAG signals can be collected noninvasively and with almost no pain to the patient. When the knee flexion and extension angles are changed, vibrations produced by knee friction are transmitted from the knee joint to the skin surface and can be detected by collection equipment for signal analysis. Because VAG signals can be obtained easily and painlessly, they are very suitable as a low-cost pre-diagnostic tool before clinical medical imaging diagnosis or for use in routine knee aging tests [103].

To allow the application of VAG signal analysis in routine knee aging diagnostic tests, the collection equipment should be small, lightweight, low-cost, and usable by non-professionals. However, the collection equipment and analysis systems for VAG signals are still scarce in medical settings. Because VAG signals are weak and easily disturbed by environmental interference, which cannot be stabilized, it is challenging to provide an accurate diagnosis. There are some good results to

distinguish between a knee with OA of Kellgren–Lawrence (KL) classification grade 3 or higher and a healthy knee, but it is still hard to distinguish between a knee with mild OA classified below KL grade 2 and a healthy knee [55]. A new feature mining and analysis method must be developed to increase the classification accuracy between mild OA cases (aging knees) and healthy knees. Therefore, we have developed a method combining multiple features, with the entropy of the short-time Fourier transform (STFT) spectrum included as an essential feature.

Entropy is a quantified measure of the complexity of physical properties. Information entropy is an expanded application of entropy in signal science, and it is often used to assess the complexity of physiological time-series signals for the diagnosis of diseased states [104]. In the method developed in the present study, the entropy of the VAG signal STFT spectrum is used as an important feature component. Before signal analysis and feature extraction, internal and external interference must be eliminated from the acquired signal. The body produces many types of biological signals, and VAG signals can be easily buried by other biological signals or ambient noise during signal acquisition, which can produce errors [105][106].

To obtain a clean VAG signal without noise, the choice of noise reduction method is critical. Denoising methods are usually classified as denoising after decomposition or direct denoising. For one-dimensional (1D) biological signals, typical digital noise reduction processes include the 1D non-local mean (1dNLM) filter and empirical mode decomposition (EMD) denoising methods [106,107]. In this study, we used the STFT spectrum in combination with the principal component analysis (PCA) threshold as the denoising method to increase the noise removal efficiency. Previous studies have shown that this filter design pattern typically has good denoising performance in VAG signal noise reduction [65,108].

A classifier is a computationally intensive part of digital signal processing. To reduce calculation hardware costs and make implementation feasible in underdeveloped areas, the tradeoff between the accuracy and speed of the calculation should be considered [109,110]. For the sake of speed, basic linear and nonlinear classifiers are used in this study instead of a deep learning classifier, despite many studies having proven that the classification results of deep learning with exhaustive numerical assessment are better [111].

Regarding participant selection, because of the similarity between the natural and early aging of the knee, we evaluated participants in two age groups with average ages of 25.4 of g and 86.3 of g years to classify knees as healthy (junior group) or aging (senior group) [112]. Simple VAG signal collection devices and lightweight algorithms were used here to identify mild knee disorders (aging knees). Although this is a challenging task, this study has already yielded some results. In this study, naturally aging knees were distinguished from healthy knees with a high rate of accuracy using the proposed system and algorithm, laying the foundation for the diagnosis of early knee aging in the

future.

4.1.2 Signal Acquisition

This section presents the details of the experiment performed in this study, including the experimental participants, the VAG signal collection device, and the VAG signal collection process. The Ethics Committee of Tokyo Metropolitan University approved this study; the approval number is H2-111.

4.1.2.1 Experimental participants

Knee joint disorders often occur in older people (natural knee aging) and manual laborers (early knee aging). Although the cause of such disorders is unclear, it is speculated to be related to the excessive wear of the knee cartilage [112,113]. Natural and early knee aging can lead to various degrees of knee disorder, and the process is not marked by noticeable knee pain [101]. The questionnaire results (Table 4.1.1) indicated little difference in the knee pain Visual Analog Scale (VAS) responses between the senior and junior groups [114]. In the VAS, no pain is assigned a score of 0 and severe pain a score of 10. The average pain scores of both groups were less than 1, demonstrating that the participants were likely unaware that mild knee pain may be an indication of disorder. In other words, these results indicate that only knee pain severe enough to inhibit mobility will attract attention; however, once the pain reaches this stage, it is often too late to apply anti-aging measures. In short, knee joint disorder by aging is almost invisible [115].

The older participants with reduced mobility were identified as having aging knees and placed in the senior group. In contrast, younger participants with unhindered mobility were identified as having healthy knees and placed in the junior group.

None of the participants recruited for this study had been diagnosed with any mental illnesses. They were all able to clearly understand the commands from the experimenter and obey the given commands. Moreover, none of the participants had suffered any severe knee trauma or undergone knee surgery in the year preceding this study.

4.1.2.2 VAG signal collection device

The VAG signals were collected with a specially designed device. Piezoelectric sensors (7BB-35-3L0 piezoelectric sensor, Murata) were used to convert the vibration signals into electrical signals. The signal was amplified with a fixed gain, and circuit noise was removed by filtering in real time. The change in the flexion–extension angle of the knee joint over time was recorded in this study. It was not possible to measure the angle directly, but acceleration was measured with an accelerometer (KXR94-2050 tri-axis accelerometer, Kionix) and calculated to angle. Both the VAG and acceleration signals were converted to digital signals by an analog-to-digital (AD) converter (MCP3208 12-bit 8-channel AD converter, Microchip). All the signals were collected at a 2000 Hz sampling rate and saved

on the computer together.

Table 4.1.1 Basic information of participants

	Senior Group	Junior Group
Number of participants	10(Including 7 females)	26 (Including 5 females)
Average age	86.3 ± 5.03	25.4 ± 2.78
Average knee pain VAS (0–10)	0.46 ± 1.21	0.25 ± 0.81
Average height (cm)	153.7 ± 9.1	172.4 ± 7.6
Average weight (kg)	55.4 ± 13.5	62.6 ± 10.1

4.1.2.3 Signal acquisition experiment

At the start of the experiment, participants were required to hold their arms crossed on their shoulders with their knees spread at shoulder width while sitting in a chair with a height equal to the calf length. The VAG sensor was fixed to the tibia with medical double-sided tape, 15 cm below the kneecap center [116]. The acceleration sensor was fixed to the thigh and aligned parallel to the thigh [117], as shown in Figure 4.1.1.

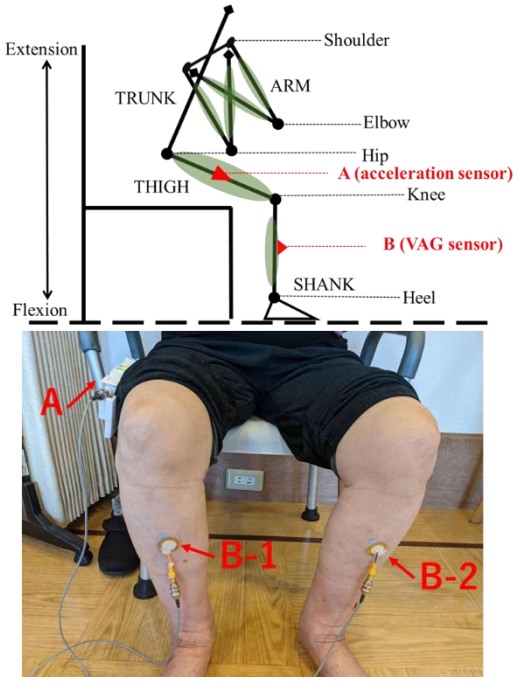

Figure 4.1.1 Fixed positions of the sensors on the participant.

A is an acceleration sensor mainly used to measure the flexion and extension angles. B-1 and B-2 are VAG sensors.

Next, the participant was required to stand up and sit down as steadily as possible three times in

3s. This action causes the contact surfaces of the knee joint cartilage changes during the flexion and extension of the knee joint. It was assumed that the knee cartilage of the senior participants is aging. The difference between the collected VAG signals for the senior and junior groups was then evaluated [117].

4.1.3 Methodology

This section presents the pre-processing and denoising methods, the VAG signal feature extraction method, and the signal classification method.

4.1.3.1 Pre-processing and denoising

4.1.3.1.1 Signal splitting

First, the signal was cut according to the knee joint bending angle. The angle was calculated from the gravitational acceleration measured with the acceleration sensor as

$$\theta = \cos^{-1}\frac{a}{g} + \frac{\pi}{2} \qquad \text{Equation 4.1.1}$$

where θ is the bending angle, a is the acceleration measured by the sensor, and g is the acceleration due to gravity. In this definition, the angle is 180° when the thigh is horizontal (parallel to the ground) and 90° when it is vertical angle (perpendicular to the ground). The sensor also recorded noise during dynamic movements, such as quivering, and thus a moving average filter is used for curve smoothing [118].

In the experiment, the participant's knee joints from flexion passed a full extension and finally returned to flexion as a complete action. In that way, a participant can usually provide three valid sets of angle data during a single motion, and the angle variation is as shown in Figure 4.1.2.

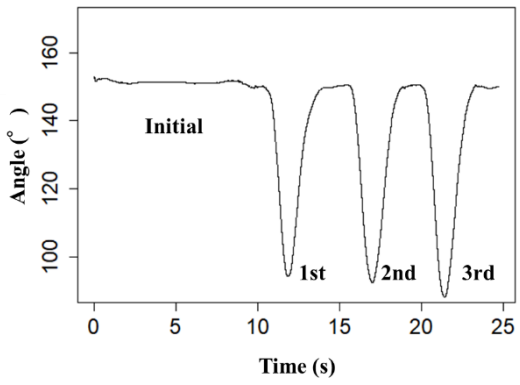

Figure 4.1.2 Flexion–extension angle of the knee during sitting and standing movements.

Because some participants could not complete the required action correctly, the failed data were manually removed. A total of 44 sets of senior group data and 92 sets of junior group data were obtained.

4.1.3.2 Denoising

The pre-processed signals were then denoised before signal analysis. The noise reduction process consisted of two parts: the removal of low- and high-frequency noise. A flowchart of the complete noise reduction process for the VAG signals is shown in Figure 4.1.3.

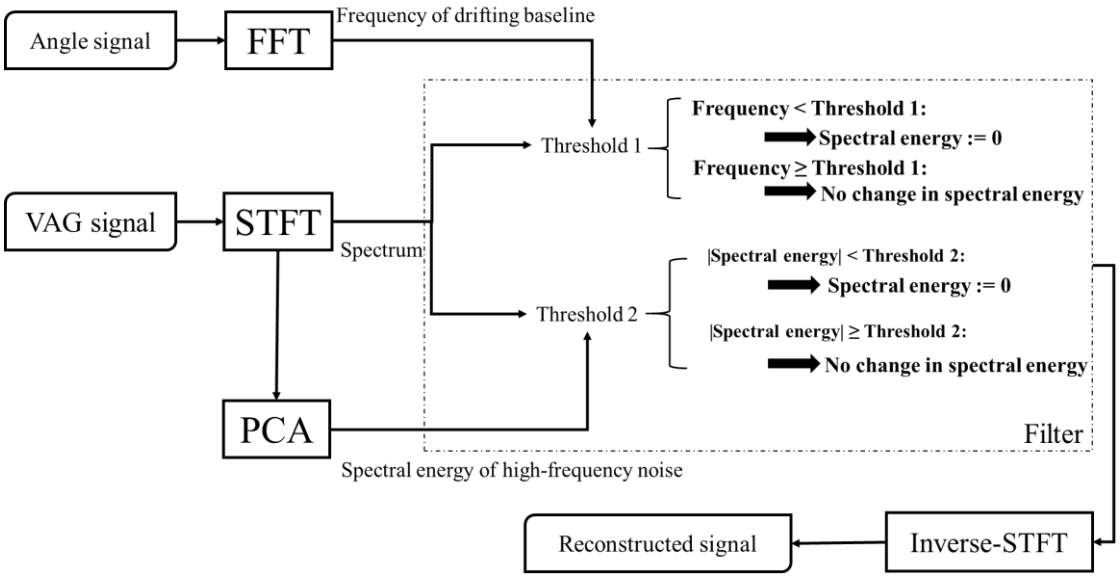

Figure 4.1.3 Flowchart of VAG signal noise reduction method.

Because VAG signals consist of nonlinear and nonstationary time-series data, it is difficult to remove the low-frequency noise component, which causes the baseline to drift. If the drifting baseline frequency can be determined, it can be removed with a well-designed filter. The baseline drift is usually produced by mechanical noise from soft tissue associated with body motions.

To prevent noise caused by movement, the activity assigned to the patient should be as simple as possible. The movement tasks selected in this experiment were standing up and sitting down, and an acceleration sensor which is fixed on the thigh, can record the mechanical noise. The cutoff frequency of the baseline drift can then be calculated by fast Fourier transform (FFT) with a Hamming window.

In the FFT, 20 Hz was used as the upper bound in this study. The Fourier spectra for the senior and junior groups were mainly concentrated below 3.5 and 4.5 Hz, respectively. Therefore, a high-pass filter was applied with a cutoff frequency (threshold 1) of 5 Hz. This noise reduction method is commonly used to filter electrocardiogram (ECG) signals and can also be used with VAG signals [119].

In recent research, a wavelet transform (WT) filter has often been used to remove high-frequency noise in biological signals, such as electromyography (EMG) and electroencephalogram (EEG) signals [120,121]. However, in comparison with a well-designed STFT filter, the performance of this noise reduction method is limited.

In addition, to optimize the use of the filter, it is best to use an optimization algorithm, such as a

genetic algorithm (GA), that selects suitable parameters and thresholds for different signals to design a filter [122]. However, the heavy calculation load of a GA is not suitable for pre-diagnosis technology. Principal component analysis (PCA) is often used for collaborative filtering in image denoising methods, and it is considered suitable to determine the VAG signal threshold [123]. Because this method has the benefit of high calculation speed, it can be used to set the high-frequency noise threshold or random noise threshold of the VAG signal.

Consequently, after considering the balance between the calculation speed and the noise reduction performance, we selected the STFT to design the filter for VAG signal denoising.

Before noise reduction, an appropriate window function must be chosen. In the present study, the simplest rectangular window function was selected as the shift window function for the STFT to satisfy the perfect reconstruction condition [124]. The rectangular window function is described by

$$w(n)=\begin{cases}1, & 1\le n\le N\\ 0, & \text{otherwise}\end{cases} \qquad \text{Equation 4.1.2}$$

where $N = 30$ was selected as the window size, and the overlap rate was set to 20%. The parameter values were selected by fitting the filter to the noise, while considering the balance between the resolutions in the time and frequency domains.

The window was shifted with a step size of 24 to obtain the overlap rate. The mth window frame of the VAG signal $x(n)$ is given by $s(m,n)=x(n)\cdot w(m-n\cdot 80\%N)$, and the STFT spectrum is obtained by taking the discrete Fourier transform (DFT) of each window frame as:

$$\begin{aligned}S(m,\omega)&=\mathrm{STFT}\{x(n)\}=DFT\{s(m,n)\}\\&=DFT\{x(n)\cdot w(n-m\cdot 80\%N)\}\end{aligned} \qquad \text{Equation 4.1.3}$$

The spectrum of the VAG signal always includes real signals and random noise. Random noise is a low-energy signal with a uniform energy distribution across the span of the VAG signal spectrum. After the PCA process, it was found that these random noise components were evenly distributed after the third principal component like a long tail. In the top 100 features obtained by PCA, the third principal component of the spectrum was set to threshold 2 for a good signal-to-noise ratio (SNR).

The filter was designed by combining threshold 1 and threshold 2. First, the low-frequency noise (threshold 1, below 5 Hz) energy was set to 0. Second, the spectrum energy was set to zero wherever its absolute value was below the third PCA (threshold 2), and a clean $S_2(m,\omega)$ was obtained. Taking the inverse STFT yielded a denoised VAG signal $y(n)$ for the next step in the signal analysis. The inverse STFT was evaluated with the overlap–add (OLA) method after the inverse DFT, as described by [124]

$$s_2(m,n) = \mathrm{DFT}^{-1}\{S_2(m,\omega)\}$$ Equation 4.1.4

$$y(n) = \sum_m s_2(m,n) \cdot \omega(n - m \cdot 80\%N)$$ Equation 4.1.5

An example of the resulting denoised VAG signal $y(n)$ is shown in Figure 4.1.4 A VAG signal with low noise is crucial for the performance of the subsequent signal analysis and feature extraction. Only by extracting suitable features can we achieve sufficient classification accuracy.

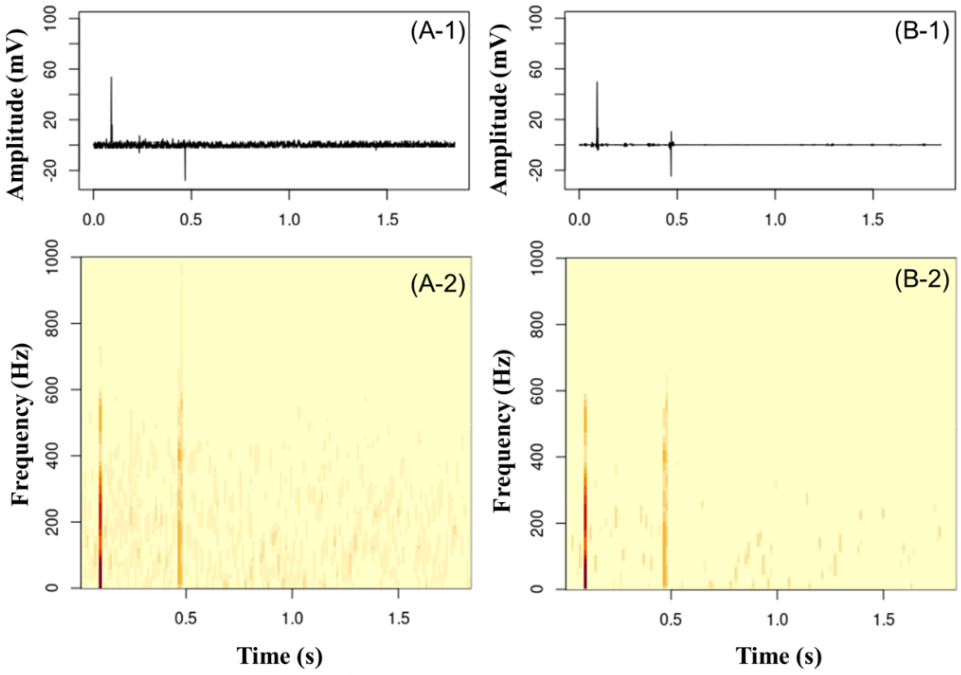

Figure 4.1.4 (A-1) Original VAG signal (senior group). (A-2) STFT spectrogram of (A-1). (B-1) VAG signal after noise reduction. (B-2) STFT spectrum of (B-1).

4.1.3.2 Feature extraction

The senior and junior groups were found to spend different amounts of time on the sitting–standing motion task performed in this study. This means that the durations of the recorded signals were different, so in the feature extraction process, the selected features should not depend on the number of data samples.

4.1.3.2.1 Time-domain features

For a 1D time-series signal, some basic statistical features must be observed before signal processing. As classic time-domain features have been widely used for the detection of bearing failures in industrial settings by mechanical vibration, we considered that time-domain features are of vital importance. However, the addition of unnecessary features reduces the performance of the classifier [125], and we therefore chose

to consider the time-domain features of the skewness S and kurtosis K of the VAG signal [126]. These are defined as

$$S = \frac{\frac{1}{L}\sum_{i=1}^{L}|y_i - \mu|^3}{\left(\sqrt{\frac{1}{L}\sum_{i=1}^{L}|y_i - \mu|^2}\right)^3} \quad \text{Equation 4.1.6}$$

$$K = \frac{\frac{1}{L}\sum_{i=1}^{L}|y_i - \mu|^4}{\left(\frac{1}{L}\sum_{i=1}^{L}|y_i - \mu|^2\right)^2} \quad \text{Equation 4.1.7}$$

$$\mu = \frac{1}{L}\sum_{i=1}^{L} y_i \quad \text{Equation 4.1.8}$$

where μ is the mean of a segment, which corresponds to the amplitude of the signal and is calculated using Equation 4.1.8, and L is the number of samples in the collected signal (signal length).

4.1.3.2.2 Features based on time–frequency analysis

In recent decades, the wavelet transform (WT) has begun to take the place of the STFT as the most suitable time–frequency method for analyzing nonlinear and nonstationary signals because the continuous WT (CWT) solves the problems of time and frequency resolution that occur for the STFT. However, even in CWT-based signal processing, time–frequency analysis also suffers from the problem of spectral energy leakage [127].

Because this spectral leakage problem cannot be solved entirely, another feature to replace the instantaneous frequency should be considered. In this study, the sample entropy was introduced as a feature, and this feature was calculated from the spectrum obtained from the time–frequency analysis. The sample entropy is advantageous because it is independent of signal length and is relatively simple to implement [128].

The sample entropy for a given dataset $Z(i) = \{z_1, z_2, \ldots, z_n\}$ is defined as follows. An m-dimensional template vector is defined as $\dot{Z}_m(i) = \{Z_i, Z_{i+1}, \ldots, Z_{i+m-1}\}$, and the Euclidean distance $d\left[\dot{Z}_m(i), \dot{Z}_m(j)\right](i \neq j)$ is constrained to be less than the tolerance r. The sample entropy is then defined as:

$$\mathrm{SampEn}(m, r, Z) = -\log\frac{A}{B} \quad \text{Equation 4.1.9}$$

$$\mathrm{A} = \sum \begin{cases} 1, d\left[\dot{Z}_{m+1}(i), \dot{Z}_{m+1}(j)\right] < r \\ 0, d\left[\dot{Z}_{m+1}(i), \dot{Z}_{m+1}(j)\right] \geq r \end{cases} \quad \text{Equation 4.1.10}$$

$$B = \sum \begin{cases} 1, d\left[\dot{Z}_m(i), \dot{Z}_m(j)\right] < r \\ 0, d\left[\dot{Z}_m(i), \dot{Z}_m(j)\right] \geq r \end{cases} \quad \text{Equation 4.1.11}$$

In this study, m was set to 2 and r was set to 20% of the standard deviation of $Z(i)$ to align with the ideal parameter values given in the existing literature [128].

During feature extraction, the STFT was again applied to obtain the signal spectrum. The difference between this and the noise reduction process is that the window function and length are selected for better domain resolution.

Based on the selection of the window function in the denoising step, a rectangular window with a length of 30 was again used in the time domain. In the frequency domain, a Hamming window with a length of 60 was used, given by:

$$w(n) = \begin{cases} 0.54 - 0.46\cos 2\pi n, 1 \leq n \leq N \\ 0, \text{otherwise} \end{cases} \quad \text{Equation 4.1.12}$$

Both windows have an overlap rate of 20%.

The minimum bending angle signal was used as a timestamp to divide the time-domain features of the VAG signal into two categories: standing up and sitting down. The first feature is the sample entropy of the angle signal when standing up, and the second is that when sitting down. Two different angle-entropy-based features can then be obtained. The frequency domain was also divided into three equal parts: the low-, middle-, and high-frequency segments. Each of the frequency-entropy-based features is then calculated as the sample entropy of each corresponding frequency segment. The entropy-based feature extraction processing approach is shown in Figure 4.1.5. This approach yields a total of seven features: two time-based features, two angle-entropy-based features, and three frequency-entropy-based features.

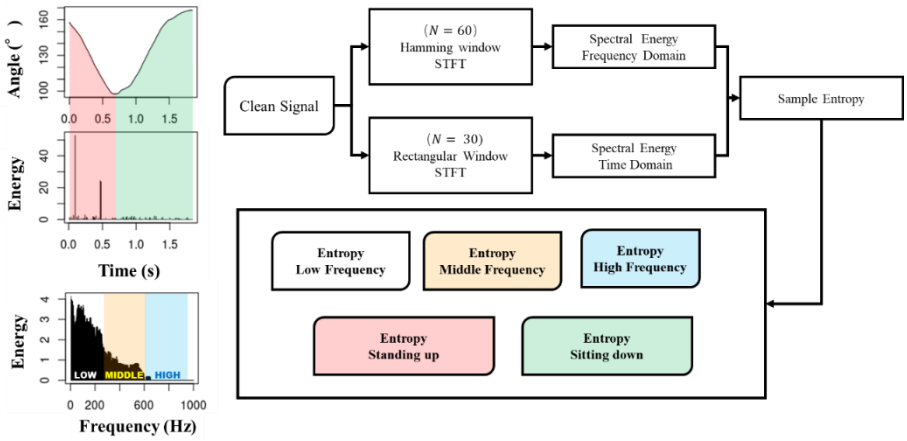

Figure 4.1.5 Flowchart of entropy-based feature extraction.

4.1.3.3 Classification

Before designing a classifier, the features were grouped. In this study, the Pearson correlation coefficient (PCC) was used to group the features, as shown in Table 4.1.2.

Table 4.1.2 Correlation coefficients for features

	Skewness	Kurtosis	Extension Entropy	Flexion Entropy	Low-Frequency Entropy	Middle-Frequency Entropy	High-Frequency Entropy
[a] Skewness	1.000	−0.257	0.097	0.072	−0.076	0.004	−0.024
[b] Kurtosis	−0.257	1.000	−0.331	−0.228	0.208	−0.336	0.275
[c] Extension Entropy	0.097	−0.331	1.000	0.481	−0.093	0.053	−0.108
[d] Flexion Entropy	0.072	−0.228	0.481	1.000	−0.081	0.041	−0.067
[e] Low-Frequency Entropy	−0.076	0.208	−0.093	−0.081	1.000	−0.384	0.891
[f] Middle-Frequency Entropy	0.004	−0.336	0.053	0.041	−0.384	1.000	−0.297
[g] High-Frequency Entropy	−0.024	0.275	−0.108	−0.067	0.891	−0.297	1.000

P-value < 0.0001

The features obtained by the same method have a strong correlation; because of this, the time-, angle-entropy-, and frequency-entropy-based features can each be considered a feature set. Second, weakly correlated features can also be combined to form a feature set, and all the features can be combined into an additional a feature set. This gives the following six feature sets; set_1:[a]+[b], set_2:[c]+[d], set_3:[e]+[f]+[g], set_4:[a]+[b]+[c]+[d]+[e]+[f]+[g], set_5: [a]+[b]+[c]+[d], and set_6: [c]+[d]+[e]+[f]+[g]. The normalized feature data were randomly divided into training and testing sets, with each comprising half of the entire dataset.

Next, classifiers were used to classify the VAG signals as junior or senior group signals according to the extracted features with a hidden label, and the correct classification rate was calculated by comparing the results with the true labels. Both linear and nonlinear classifiers were applied to verify the feature sets.

4.1.3.3.1 Logistic regression classifier

A logistic regression (LR) classifier is considered a generalized linear model classifier because the output always depends on the sum of the inputs and parameters. Usually, LR is applied to binary classification problems (two classes). In reality, LR can also be used on problems with more than two classes (multinomial). In LR classification, the probability is calculated using a logical function as

$$p = \frac{1}{1+e^{-u}} \qquad \text{Equation 4.1.13}$$

$$u = a_0 + a_1 \cdot f_1 + a_2 \cdot f_2 + \cdots + a_d \cdot f_d \qquad \text{Equation 4.1.14}$$

$$p = \begin{cases} \text{Negative}, & 0 \le p < 0.5 \\ \text{Postive}, & 0.5 \le p < 1 \end{cases}$$ Equation 4.1.15

where p is the probability of the classification decision, u is the sum of the input features and parameters, $\{f_1, f_2, \cdots, f_d\}$ are the features of the VAG signal, d is the dimension, and $\{a_0, a_2, \cdots, a_d\}$ are the weight coefficients.

4.1.3.3.2 K-nearest neighbors classifier

The *k*-nearest neighbors (KNN) classifier is radically different from the LR classifier. This type of classifier is nonlinear and shows good performance in pattern recognition. KNN requires the tuning of only one parameter, k, which is the number of nearest neighbors, and does not make any assumptions about the distribution of the training data [129].

The nearest neighbors can be found by computing the Euclidean distance in feature space between the training and testing data. The dominant class among the nearest neighbors determines the class of each of the data points in the testing set. Thus, the choice of k is very important; a k value that is too small will cause over-fitting of the boundary, whereas one that is too large will cause under-fitting. In this study, the cross-validation method was used to obtain a suitable k value: $k=5$.

4.1.4 Results

The classification results were summarized by the F-score method. The senior and junior groups were considered to be the positive and negative classes, respectively. That is, if both the predicted and true classes are the senior group, this is a true positive, and the converse (both predicted and true being the junior group) is a true negative. Additionally, the incorrect classifications of a predicted senior group with a true junior group and vice versa are respectively a false positive and a false negative. The results are given in Table 4.1.3.

As demonstrated by the results in Table 4.1.3, the LR classification accuracy of each feature set was higher than the KNN classification accuracy. The highest accuracy was obtained with set_4 and the lowest with set_3.

Table 4.1.3 Classification results

KNN	TP	TN	FP	FN	ACC	PRE	SEN	SPE
set_1	16	45	6	2	0.8841	0.7273	0.8889	0.8824
set_2	13	43	9	4	0.8116	0.5909	0.7647	0.8269
set_3	11	42	11	5	0.7681	0.5000	0.6875	0.7925
set_4	18	46	4	1	0.9275	0.8182	0.9474	0.9200
set_5	16	46	6	1	0.8986	0.7273	0.9412	0.8846
set_6	14	44	8	3	0.8406	0.6364	0.8235	0.8462

LR	TP	TN	FP	FN	ACC	PRE	SEN	SPE
set_1	14	45	8	2	0.8551	0.6364	0.8750	0.8491
set_2	12	43	10	4	0.7971	0.5455	0.8000	0.8148
set_3	7	45	15	2	0.7536	0.3182	0.7778	0.7500
set_4	17	46	5	1	0.9130	0.7727	0.9444	0.9020
set_5	15	46	7	1	0.8841	0.6818	0.9375	0.8679
set_6	14	43	8	4	0.8261	0.6364	0.7778	0.8431

TP: True Positive. TN: True Negative. FP: False Positive. FN: False Negative.

ACC: Accuracy. PRE: Precision. SEN: Sensitivity. SPE: Specificity.

4.1.5 Discussion

The accuracy of the classification demonstrates the good performance of this method in the diagnosis of the naturally aging knee. The highest accuracy of the true positive rate (sensitivity) reached 0.9474 with set_4. Both the LR and KNN classifiers can achieve a maximum overall accuracy exceeding 0.9.

Because of the high performance of the proposed method, we also used previous data to verify the reproducibility of the results. VAG signals recorded from 25 OA patients and 26 healthy participants were input into the developed pipeline. Although different devices with different sampling rates were used, the frequency domain was again equally divided into low-, middle-, and high-frequency segments. Because of the lack of sitting down movement, set_2 only includes the extension entropy. In addition, the accuracy of this method was compared with that of existing methods, and the results are given in Table 4.1.4[55,130,131].

Table 4.1.4 Comparison with existing studies

	SVM [30]	LS-SVM [31]	LS-SVM [7]	KNN (this study)	LR (this study)
ACC	0.8661	0.8356	0.8667	0.8727	0.88
SEN	0.9107	0.944	0.7899	0.8846	0.875
SPE	0.7878	0.8	0.9023	0.8821	0.8519

ACC: Accuracy. SEN: Sensitivity. SPE: Specificity.

SVM: Support-Vector Machine.

LS-SVM: Least-Squares Support-Vector Machine.

As shown in Table 4.1.4, the methodology proposed here achieved a better diagnosis accuracy than support-vector machine (SVM) series classifiers. However, the sensitivity in this case was not as high as 0.9, which is as expected. The reference study demonstrates that aging occurs in the entire body, including every muscle and joint [132,133]. Because the VAG sensors were attached to the tibia, between the knee joint and the ankle joint, they also would have collected signals generated by the

naturally aging ankle joint. Therefore, it is hypothesized that the features may have been enhanced by the mixed aging ankle and knee VAG signals, leading to the high accuracy of the knee aging diagnosis of above 0.9 in Table 4.1.3. However, early aging is different from natural aging, in that it occurs in targeted areas as a result of injury or overuse. If the proposed pre-diagnosis system is applied to early knee aging in the future, the accuracy of diagnosis may be less than that obtained here because of this factor.

Additionally, the frequency-entropy-based feature sets had the lowest accuracy. There are two reasons for the poor results obtained with these features: the first is that the threshold selection in the noise reduction process is not sufficient, resulting in the loss of details in the signal, and the second is that the window function is too short, resulting in the low frequency resolution in the feature extraction process. This demonstrates that our algorithm still has room for improvement.

Although KNN had a higher accuracy than LR, LR was selected as the first choice for our pre-diagnosis system. The maximum accuracy difference between LR and KNN was $\Delta set_1 = 0.029$, and the difference at the highest accuracy was only $\Delta set_4 = 0.0145$, as indicated in Table 4.1.3. From the results of the LR analysis shown in Figure 4.1.6, the classification edge of feature [a] is not linear but closer to quadratic. The above findings can explain the accuracy difference between the two classifiers with set_1. Optimizing the classification features and classifier parameters remains a task for future work.

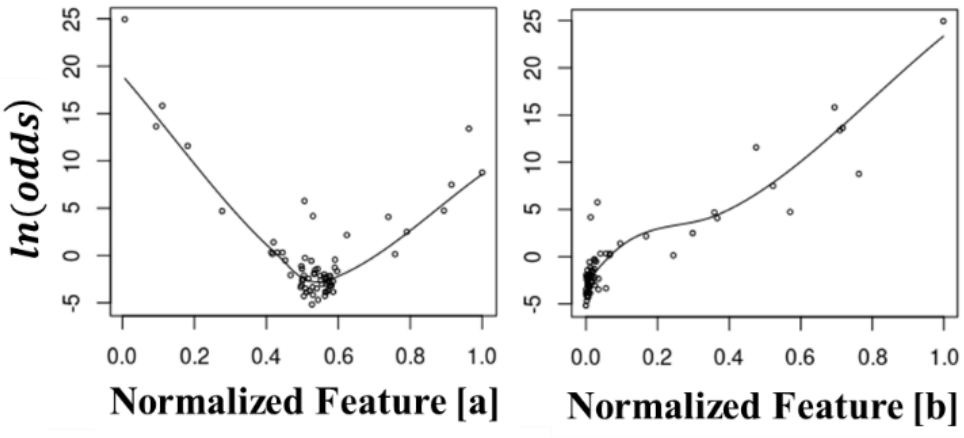

Figure 4.1.6 Feature [a] and [b] classification edges for set_1 in the LR classifier.

Furthermore, when a Core i7 7700k was used for the calculations, the training and testing of the LR method took 0.16 s, whereas the training and testing of the KNN method took 14 s. Considering that the size of the dataset grows with an increasing number of participants, LR was our first choice for the diagnosis of early knee aging.

Finally, the receiver operating characteristic curve (ROC) was obtained, and the area under the curve (AUC) was calculated for each group of features of the preferred LR classification.

As shown in Figure 4.1.7, the largest AUC was obtained with set_4, and it reached a standard very

close to excellent. Among the six sets of features, four sets achieved a good standard, and only two were of a low standard [96]. These results indicate that the proposed method can be used as a pre-diagnostic technique for knee aging that is feasible for widespread use.

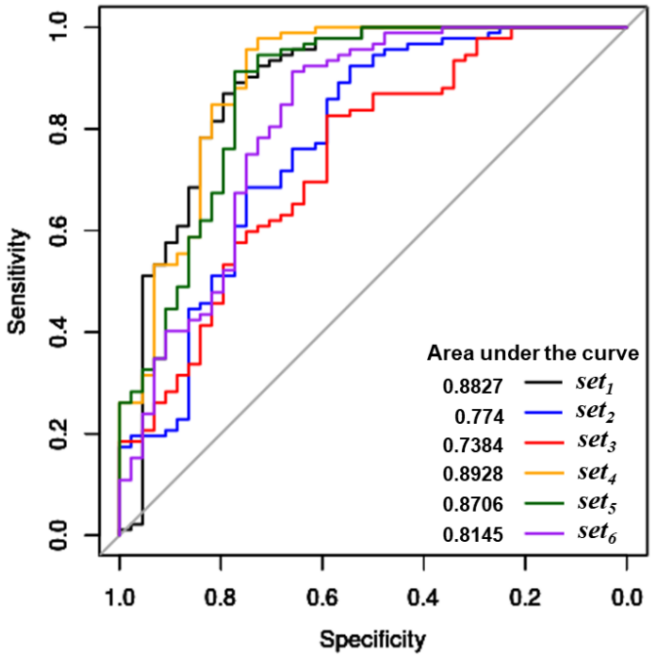

Figure 4.1.7 ROC of LR classifier

The VAG signal has many advantages and has not been widely used as a conventional knee diagnostic indicator. Not only is this signal easily disturbed by noise during collection but this noise must also be eliminated in a computationally demanding process. Consequently, a denoising algorithm using the STFT was developed in this study to solve the noise problem to a certain extent. Additionally, to avoid the impact of energy leakage in the STFT, the sample entropy was used as a classification feature in the time–frequency analysis.

This makes our approach appear somewhat complicated. The average processing time must therefore be determined to verify the computational efficacy of the entire system, and signal collection was not included in this processing time.

As shown in Table 4.1.5, even a lightweight algorithm requires almost 60 s. After excluding the semi-manual pre-processing step, the largest proportion of the calculation time is devoted to denoising. Thus, improving the denoising efficiency while maintaining reproducibility is an important challenge that will be addressed in future work.

Table 4.1.5 Average processing time

	Pre-processing	Denoising	Feature Extraction	LR Classifier	Total
Junior group	23.15 (s)	21.52 (s)	0.95 (s)	0.16 (s)	45.78(s)
Senior group	24.22 (s)	23.46 (s)	2.3 (s)	0.16 (s)	50.14(s)

※Core i7 7700k

Several limitations are worth noting in this study. First, the use of only one type of sensor causes restrictions in this study. The natural aging process affects the whole body, including the musculoskeletal system and joints [101,112,134]. The diagnosis of knee aging would be more accurate if electromyographic (EMG) sensors could be added to analyze the role played by muscles. Second, the participant sample size was quite small. Although we reduced the bias by increasing the experimental sample size, expanding the number of participants remains among the most important tasks for future study. Finally, the experiments in this study were completed in a simple environment to avoid environmental interference. Before the diagnosis system of knee aging is applied in the clinic, reliability testing in a complex environment must be considered.

4.1.6 Conclusion of this Section

In response to osteoarthritis caused by an invisibly aging knee joint, this paper proposed a method for the analysis of VAG signals, and a classification accuracy of 90% was obtained in a natural aging diagnosis experiment. This result indicates that with the device and algorithms proposed in this study, one cause of knee disorder can be identified. Identifying aging knees with the proposed method can delay the onset of knee disorders with physical therapy and rehabilitation. Although there remain some limitations, such a lightweight pre-diagnosis system would provide the great advantage of widespread usability. For example, manual laborers living in areas lacking medical staff and equipment would have a higher likelihood of receiving a diagnosis in time to counteract the damaging effects of knee OA.

Chapter5

Pre-processing of VAG signals

5.1 A Brief Review About the Pre-processing of VAG Signal

Although the VAG signal is a biomedical signal, it is a mechanical wave signal rather than an electrical signal. While both electrical, as well as mechanical wave-based biomedical signals, are affected by interference, mechanical wave signals are significantly more affected. This is why biomedical signals often require more elaborate pre-processing. In this section, let's briefly review the pre-processing of VAG signals.

5.1.1 Categories of VAG Signals

Once the VAG signal is converted from analog to digital, it can be analyzed and processed. Before analyzing the signal, it is necessary to category the signal. The classification method is not much different from other types of time series.

First, determine the stationarity of the VAG signal. When it becomes a stationary signal, its frequency component does not change. A non-stationary signal is a signal whose frequency changes with time. Note that if the amplitude or time of the signal is scaled, the steady-state also changes.

The next is the distribution of data points of VAG signals. There are two types of statistical results, Gaussian type and non-Gaussian type[135]. Most of the VAG signals are Gaussian type, but the non-Gaussian type is attracting particular attention because of its high independence. The type of VAG signal is judged by a general normal distribution (Shapiro test, etc.), but recently it can be judged by negative entropy.

The final is the VAG signal belongs to linear or non-linear. The tendency of VAG signals is linear or non-linear when fitting a mathematical function. Be careful of overfitting and underfitting.

5.1.2 Adjusting the Trend and Length of the VAG Signal

After the first categorization of the VAG signal, a simple pre-processing is needed to make it easier to analyze. It is usually necessary to process the baseline drift at the observed location. The easiest way to get rid of this baseline drift is to use a high-pass filter that combines a Fourier transform (FT) and a Butterworth filter. The root mean square error (RMSE) can also be used as a criterion to evaluate the effectiveness of baseline drift removal. Since the error caused by the trend is distributed in the global area of the signal rather than the local area, the baseline drift should be removed first, and then the signal length should be pruned, and the order is not interchangeable[136].

5.1.3 Handling missing values and outliers of the VAG Signal

Handling missing and outlier values are the most difficult and tough part of signal processing, regardless of the type of biomedical signal. When the VAG signal has been collected, most of the data is normal, but sometimes there are missing or outlier values due to sensor or circuit poor contact. Pre-processing is required to handle outliers and missing values. Missing values are easy to find in the data and are usually stored in “NA” format. Outliers are difficult to detect, and it is difficult to distinguish between outliers due to body abnormalities and those due to electronic circuitry. A common technique is to use box-and-whisker plots or Grubbs tests to filter outliers from the signal and then remove the outliers[137]. In recent years, a class of support vector machines has become a common method for detecting anomalies, and machine learning models are sensitive to outliers and can find overlooked regions.

In addition, the missing values that are always present in the signal and the missing values due to the removal of outliers are replenished. There are two common replenish methods used to deal with missing values: interpolation and extrapolation. The extrapolation method builds some known numerical data on the expected values outside the data range. The interpolation method is a method of constructing (finding) new data points based on the range of a discrete set of known data points. The interpolation method here is the interpolation method. The well-known methods are spline interpolation and Lagrangian interpolation[138].

5.1.4 Denoising Processing

Denoising is a core aspect of preprocessing, and there are countless books on signal processing alone to guide researchers and engineers in this process. The design and construction of filters are the core of the core. Filters can be designed based on the time domain, representative of which is the moving average filter. Filters can also be designed in the frequency domain, such as high pass, low pass, band pass, and band rejects filters. A novel filter design solution for the VAG signal is described in the next section.

5.1.5 Conclusion of this Section

In this study, the pre-processing of the VAG signal is considered to be a more important step than the subsequent analysis. However, it is also the most neglected and error-prone part of the process. Pre-processing has a very low tolerance for mistakes, and the slightest oversight can turn the whole job into ashes. The research related to biomedical signal pre-processing is also our future direction.

5.2 Adaptive VAG Signal Denoising via Ant Colony Optimization using Dynamic Denoising Filter Parameters

5.2.1 Introduction of this Section

Knee disorders are often caused by damage to cartilage and meniscus. Such injuries are among the common causes of pain and disability in middle-aged and elderly patients and are the leading cause of impairment in daily life activities [139]. Most cases of injury or disorder generate odd vibration signals or sound signals, which are referred to as vibrarthographic (VAG) signals. Although VAG signals are also present in healthy knees, the VAG signal from a normal knee is irregular, with an insignificant vibration amplitude. However, in an abnormal knee, VAG signals have features that are different from those of the normal knee and can generally be found by signal analysis [105].

Notably, there has been a long history of clinical diagnosis of knee disorders by observing the vibration and sound of the knee joint. Early clinical diagnosis was made through palpation and stethoscope, which were based on listening to the sound and feeling the vibrations based on the doctor's experience. With the development of electronic technology and data storage technology, the VAG signal as a biological signal can be digitized for data analysis. After signal processing and analysis, the disordered knee joint and healthy knee joint can be distinguished by extracting the features of the VAG signal. Zhang et al. argued that wavelet transform (WT) extraction is best performed during dynamic knee movement [140]. Indeed, WT has a higher accuracy resolution in terms of time and frequency scales than the fast Fourier transform (FFT). Because the FFT decomposes a signal into its frequency components, the FFT loses information in the time domain. In other words, it is challenging to analyze signals that contain non-periodic and fast transient features [55]. Continuous WT analysis was also considered to be a tool for VAG signal analysis of knee joint pathology [141].

Before signal analysis, biological signals have a challenge regarding signal denoising. Biological signals are susceptible to the surrounding environment and physical state of the participant. Even the best signal analysis method cannot be implemented in a signal with a low signal-to-noise ratio (SNR). Unfortunately, the VAG signal is an unstable signal with a very low SNR. Although we had made a distinction between aged and healthy knees using the VAG signal, it is still the denoising process that affects the classification accuracy[54]. Hence, the VAG signal should be subjected to more finely denoising pre-processing.

Compared with the electrocardiogram (ECG) signal, the denoising process is more difficult because there are few fixed-shape waveforms and inconspicuous peaks and valleys in the VAG signal [69,142,143]. The signal waveform changed significantly depending on whether the target was a

cartilage, meniscus, or ligament disorder in the knee joint [144].

The most problematic VAG signal in the denoising process originates from healthy knees and slightly damaged knees. Such knees have fewer peaks and lower amplitudes and are more easily disturbed by environmental interference and random noise. Many studies have attempted to design filters to remove these types of noise, but it is still difficult to obtain a true signal and distinguish noise from the VAG signal. Therefore, signal decomposition followed by filtering as a novel attempt has been suggested. Also, good results have been reported in using hybrid technology to denoise the electroencephalogram (EEG) signal [145,146] through filter design after decomposing the original signal. Since both EEG signals and VAG signals are unsteady biological signals, we attempt to learn from this hybrid technology.

The empirical mode decomposition (EMD) method is often used to decompose a biological signal to combine well-designed filters for denoising hybrid technology. Although no obvious misdiagnosis has been reported for the classification of a knee joint with osteoarthritis (OA) by VAG signals with EMD, there is a mode mixing problem that cannot be ignored [117,147].

Regarding the VAG signal, the reason for the mode-mixing problem is noise interference. There is a high-frequency noise discontinuity distribution in the original VAG signal, leading to the signal being a local high-frequency signal. Thus, it causes the point of the local extreme value of the original signal distribution to occur mutations, causing the envelope formed by the local extreme value point to exhibit jump phenomena. Finally, the resulting time-scale fit error caused the mode mixing phenomenon to occur in the EMD process.

When mode mixing occurs, an intrinsic mode function (IMF) can cease to have physical meaning by itself, falsely suggesting that different physical processes are represented in a mode. Hence, ensemble EMD (EEMD) is a correction method for EMD[108,111].

However, even with EEMD-based hybrid technology denoising using a filter with fixed thresholds and parameters, the SNR improvement is desirable for the VAG signal of a healthy knee. In other words, the denoising problem of an abnormal VAG signal is approximately solved whenever the denoising problem of the VAG signal in the normal knee is solved. Therefore, researchers had sought help from evolutionary algorithms [148]. Some studies have indicated that a hybrid denoising filter with a genetic algorithm (GA) has been successfully applied to an ECG signal with a typical waveform and is a significant improvement over traditional method [149,150]. Nevertheless, there has been little progress in the noise reduction processing of VAG signals because of the inability to preserve real signal components while removing noise components. However, in the VAG signal analysis, we found that the noise component and real signals were not evenly distributed to each sub-signal by EEMD.

We hypothesize that if a filter with adaptive thresholds can be added to each sub-signal, then it may be possible to remove noise while preserving real signals to the greatest extent possible. To verify the above hypothesis, we propose the use of the zero-crossing rate (ZCR), which is the number of times

within an epoch in which the signal crosses the zero-amplitude axis, to evaluate each sub-signal and the use of the Savitzky–Golay filter (SG filter) to remove noise components. We attempt to use ant colony optimization (ACO) algorithms for the core of the algorithm for optimal parameter selection.

ACO algorithms are inspired by the foraging behavior of some ant species and have been applied to several combinatorial optimization problems as a swarm intelligence algorithm[55,151]. These ants deposit pheromones on the ground to mark a favorable path that other colony members can follow. In the proposed method, the high SNR is the "food," and the parameters and threshold of the denoising filter are the "favorable path." ACO exploits a colony behavior mechanism to solve optimization problems[55]. Accordingly, the present study attempts to design a denoising filter that combines ACO and optimization parameters based on EEMD to obtain a stable VAG signal with high quality after denoising processing.

The main contribution of the present study is the proposal of an improved VAG signal quality method using hybrid EEMD and ACO, and the proposed hypothesis has been proven experimentally and thoroughly evaluated. The proposed method not only improves the VAG signal quality but also extends to other low-amplitude biological signals based on the results of this study. The proposed method may become an inspiration for noise reduction technology for low-amplitude signals.

In addition, the biggest highlight of the proposed method is that each step of the decomposition, optimization and denoised process phases does not include the operation of the frequency components. After the proposed denoising process, the denoised signal is very conducive to extracting the frequency-domain features. Features extracted from infinitely close to the real VAG signal may help the knee joint disorder diagnosis classification model with machine learning to become more reliable.

5.2.2 Methods

5.2.2.1 Vibrarthographic signal acquisition and pre-processing

For signal acquisition, a novel device that can record a VAG signal is created. The signal collection procedure was as follows: The sensor (7BB-20-6L0 piezoelectric sensor, Murata) was attached to the tibia of the participant, which was 15 cm below the center of the patella using medical double-sided adhesive tape. An acceleration sensor (KXR94-2050 tri-axis accelerometer, Kionix) was attached to the participant's thigh to measure the flexion-extension angle of the knee joint. The participant must keep their arms tight against the body and keep their legs open approximately shoulder width while sitting down on a calf-length chair with armrests. The patient must stand up and sit down as steadily as possible three times within 3 seconds [117]. Before the experiment, each participant was allowed to practice the required movement with the same rhythm, and the device recorded the VAG signal and the angle signal at a sampling rate of 2000 Hz during the experiment.

In the data pre-processing step, to monitor the features of the interest of the VAG signal, the flexion-extension movement must be repeated three times to determine the timestamp of the angle signal. We interrupted the raw VAG signal according to the timestamp and set each VAG signal length between 5000 and 6000.

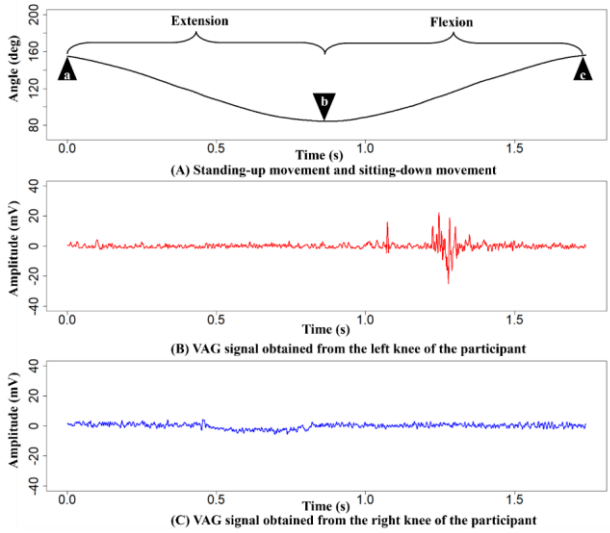

Figure 5.2.1 VAG signal and bending angle during dynamic knee movement

Correcting the baseline wander is also an essential step. A baseline wander is a typical artifact that causes the recorded VAG signal distortion and hinders the correct diagnosis of diseases [108]. The baseline-wander is a low-frequency artifact in the VAG signal that commonly arises from the amplifier or participant movement and is quickly removed by a moving-average filter in the present study. An example of an acquired VAG signal after cutting and baseline-wander correction is shown in Figure 5.2.1.

In Figure 5.2.1, although the VAG signals in the left and right knees do not differ significantly in stages a-b, more substantial amplitude peaks are present in the left knee in stage b-c. These peaks have a higher full width at half maximum (FWHM), which is probably the reason for the slight pain. The possibility of injury may be hidden by pain or discomfort in the knee joint, manifested as different frequency and amplitude peaks, particularly high FWHM peaks, in the VAG signal waveform [111]. For the denoising process, signals without any particularly pronounced peaks are more difficult to handle. The present study prefers to use the normal knee VAG signal to test the denoising capability of the proposed algorithm.

Therefore, the present study used 60 sets of VAG data for knees obtained from 26 participants aged between 20 and 30 years who did not have any pain or discomfort and were not diagnosed with a knee joint disorder before the experiment. For comparison, this study also used 10 sets of VAG data obtained from 3 participants aged between 80 and 90 years who have knee pain and limited mobility [54]. All study participants provided informed consent, and the ethics review board of Tokyo Metropolitan

University approved the study design (approval number H2-111).

Before the denoising algorithm began, a white noise signal was added to the original VAG signal. White noise is a random signal with a constant power spectral density. The power of the white noise signal in each frequency band is the same and is often used to test the effectiveness of the denoising method [148]. In the present study, white noise was added in two ways. The first is to set the white noise amplitude based on the SNR of the noisy VAG signal and the original VAG signal, and the second is to set the white noise amplitude based on the percentage of the peak value of the original VAG signal. Independent of the method used to add white noise, the purpose was to test the effectiveness of the denoising method in various imaginary noise environments

5.2.2.2 Standard Denoising Method

Denoising methods are usually characterized as a denoising process after decomposition or a direct denoising process, as shown in Figure 5.2.2

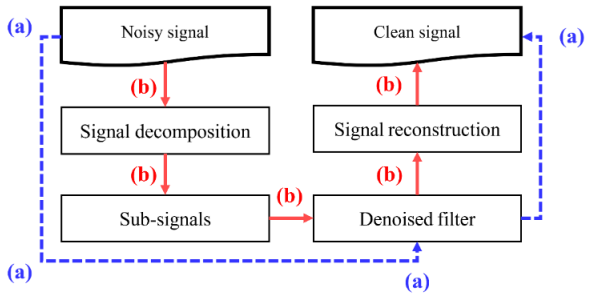

(a) A direct denoising process
(b) A denoising process after decomposition

Figure 5.2.2 Standard denoising methods

As the name implies, the direct denoising process is performed on the original signal. The denoising process after decomposition is decomposed into sub-signals and then operates on these sub-signals. The denoising process after decomposition (Path b) was chosen as the standard denoising method in the present study. Because any signal can be assumed to consist of different sub-signals of an oscillation, the sum of the information of the sub-signals is greater than the original signal [149]. The proposed method not only decomposes the VAG signal using EEMD, but also selects the decomposed sub-signals. Unlike the standard method, in the proposed method, the filter parameters are optimized for different sub-signals.

5.2.2.3 Proposed Denoising Method

As shown in Figure 5.2.3, the proposed method for the denoising process can be summarized in three phases: decomposition, optimization, and denoising. The decomposition phase decomposes the EEMD of a noisy VAG signal into several sub-signals and the classification of the sub-signals by the ZCR. An additional note is that the ZCR carries frequency information in the time domain but does not change the frequency-domain components. The optimization phase involves finding and outputting

the optimal parameters for the denoising filter. Finally, the denoising phase involves adapting the filters with optimal parameters to reduce the noise of each sub-signal and reconstruct a clean VAG signal.

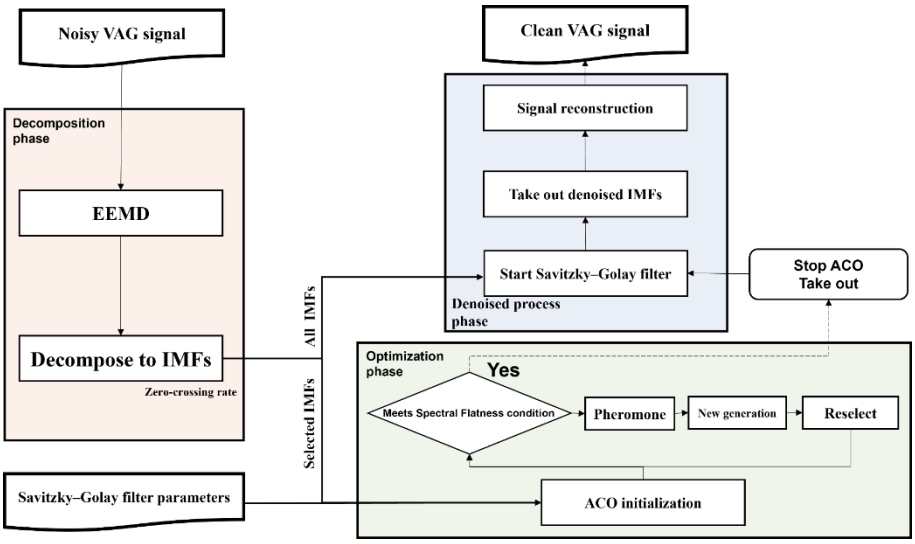

Figure 5.2.3 Flowchart of ACO-EEMD hybrid-technique-based dynamic parameters for the denoising process

5.2.2.3.1 Decomposition Phase

Specialization is to assign specific types of members and joints to every available generalized chain subject to certain design requirements to obtain the specialized chains. Among, design requirements are determined based on the concluded topological structure of the original designs.

In this phase, the main task is to decompose the noisy VAG signal using the EEMD method. The EEMD algorithm can usually be described as:

$$x^i[n] = x[n] + G^i[n] \qquad \text{Equation 5.2.1}$$

where the target signal $x[n]$ and $G^i[n](i = 1,\ldots,I)$ are different realizations of white Gaussian noise. The standard deviation $\hat{m}$ of the white Gaussian noise, $G^i[n]$ is relative to the absolute amplitude of $x[n]$. We multiply the absolute amplitude using a multiplier to denote the noise width. The multiplier in this study is $m = 0.05$, which is lower than the recommended value of $m = 0.2$ [150].

$$\hat{m} = m \cdot |\max(x[n]) - \min(x[n])| \qquad \text{Equation 5.2.2}$$

The crucial components of the VAG signal are mainly concentrated in high frequencies. signal. Consequently, the filtered high-frequency white Gaussian noise strength must be reduced to detect e the VAG signal. Therefore, we set a threshold for the maximum filtered white noise level. We chose 5% absolute amplitude for the noise standard deviation. In fact, the additional noise enhances the decomposition method to avoid mode mixing and improve the performance of the EEMD algorithm. However, the impact outside the decomposition process is next to nothing after the ensemble average [150].

Each $x^i[n](i=1,...,I)$ is completely decomposed by EMD, giving the modes $IMF_k^i[n]$ of the signal, where $k=1,...,K$ denote the modes. We define $\overline{IMF_k}$ as the k^{th} mode of x[n], obtained as the average of the corresponding IMF_k^i as follows:

$$\overline{IMF_k}[n]=\frac{1}{I}\sum_{i=1}^{I}IMF_k^i[n] \qquad \text{Equation 5.2.3}$$

In the proposed method, the signal is decomposed into 10 IMFs by EEMD, and the deviation values of their ZCRs were calculated. The ZCR of a signal frame is the rate of signal changes of the signal during a frame, which reflects the number of times that the signal changes from positive to negative, divided by the length of the frame [152]. Letting $y_i(n)=0,1,...,N-1$ be the samples of the i^{th} frame, the ZCR is defined by the following equation:

$$ZCR(i)=\frac{1}{2N}\sum_{n=0}^{N-1}\left|\mathrm{sgn}\left[y_i(n)\right]-\mathrm{sgn}\left[y_i(n-1)\right]\right| \qquad \text{Equation 5.2.4}$$

where,

$$\mathrm{sgn}\left[y_i(n)\right]=\begin{cases}1, y_i(n)\geq 0\\ -1, y_i(n)<0\end{cases} \qquad \text{Equation 5.2.5}$$

We then arrange all deviation values of $ZCR(i)$ from large to small, and the five largest IMFs are labeled imf_1 through imf_5 The five smallest IMFs are combined into one IMF, and the result is labeled $imf_{combine}$. In addition, a denoising filter must be prepared for the IMFs, where the SG filter is chosen as the base filter.

The SG filter is often used to smooth biological signals for SNR improvement [151]. The SG filter is also referred to as the least-squares smoothing filter, which performs better for VAG signals than traditional moving-average filters, with a particular advantage in the high-frequency domain. The SG filter is not very good at rejecting noise but is more effective for preserving high-frequency information components [153]. In addition, because the SG filter is particularly good at preserving the line shape, this filter is conducive to signal reconstruction processing in the next step. Finally, the SG filter has few parameters, which can reduce the optimal calculation time. Thus, the SG filter was chosen in the present study.

5.2.2.3.2 Optimization phase

The SG filter is referred to as the objective function $F_{objective}$ in the ant colony system. There are two main dynamic parameters of $F_{objective}$: frame length λ (which must be odd) and polynomial order ξ. In addition, dynamic parameters must be set within a reasonable range. In addition, there is a parameter that returns the v_{th} derivative of the convolution coefficients. We set the derivative order to zero for the filter to smooth the curve.

The ACO algorithm continuously optimizes the dynamic parameters to achieve a better noise

reduction effect. A condition function (called the fitness function in the evolutionary algorithm) must be manually set to accomplish the goal. The choice of the condition function is essential because this function directly affects logical structure of the total algorithm. In the present study, the spectral flatness is chosen as a condition function $F_{\text{condition}}$ to plan the best path for the ant colony system. Generally, we calculate the spectral flatness by dividing the geometric mean by the power spectrum using the arithmetic mean [154]. The spectral flatness is defined as follows:

$$F_{\text{condition}} = \frac{\sqrt[N]{\prod_{n=0}^{N-1} H(n)}}{\frac{\sum_{n=0}^{N-1} H(n)}{N}} \qquad \text{Equation 5.2.6}$$

where N represents the length of the power spectrum $H(\text{n})$, and n represents the value of a discrete sample of $H(\text{n})$, where $n = 1, 2, 3..., N$.

The combination of the condition and objective functions can export the cost function $\text{F}_{\cos t}$ to the ACO algorithm. The minimum value of the cost function $\min(\text{F}_{\cos t})$ is also referred to as the favorable path of the ant colony system. Here, $\text{F}_{\cos t}$ is described as

$$F_{\text{cost}} = \sum_{i=1}^{5} F_{\text{condition}}\left(F_{\text{objective}}\left\langle imf_i, \lambda, \xi \right\rangle\right) + F_{\text{condition}}\left(F_{\text{objective}}\left\langle imf_{\text{combine}}, \lambda, \xi \right\rangle\right) \qquad \text{Equation 5.2.7}$$

where $\lambda \in [5, 21]$ and $\xi \in [2, 5]$. The term λ is specified as a positive odd integer, and ξ must be a positive integer that is smaller than $\lambda - 1$, which can also be summarized as a two-dimensional search space with constraints in the ACO algorithm [147].

In the initialization of the ACO algorithm, some parameters must be adjusted to balance the computation speed and accuracy. In the present study, we preferred to control the number of generations of ants rather than the number of ants. As such, we set $\delta = 100$ ants in each generation, which is equivalent to 25 generations. After randomly generating the pheromone path for the first generation of ants in each search space, the step solutions s_1 and s_2 for each ant must be computed based on $F_{\text{condition}}$. In the pheromone path of the first generation of ants, the solutions increase in order in the archive according to quality (minimum pheromone evaporation) and are indicated by rank as l. The probability $prob_l$ of choosing the path for each ant as a prototype for the next generation is calculated by the weight w_l and is consistent with a Gaussian distribution function, as follows:

$$w_l = \frac{1}{q\delta\sqrt{2\pi}} \exp\left(-\frac{(l-1)^2}{2(q\delta)^2}\right) \qquad \text{Equation 5.2.8}$$

$$prob_l = \frac{W_l}{\sum_{1}^{\delta} w_l} \qquad \text{Equation 5.2.9}$$

where $q \in (0, 1)$. When q is small, the best-ranked solutions are strongly preferred, and when q is large, the probability becomes more uniform. We set q = 0.2 to set adjust the probability towards a more

uniform distribution.

The optimal parameters are obtained by iteration of the better solutions, choosing s_l as the prototype. This process was achieved by adding the standard deviation, σ_l^i of each solution. This process is referred to as the pheromone update in ACO [155].

However, the pheromones evaporate over time. If pheromones are not updated by the next generation of ants, the pheromone path will decrease at a constant evaporation rate η For $\eta > 0$, which is the same for all dimensions (the higher the value of η, the lower the convergence speed of the algorithm), we set $\eta = 0.5$. To establish the value of the standard deviation σ_l^i at construction step $i \in \{1, 2\}$, we calculate the average distance from the chosen solution s_l to other solutions in the archive and multiplied this distance by the evaporation rate η. The standard deviation was calculated as follows:

$$\sigma_l^i = \eta \sum_{j=1}^{\delta} \frac{\left| s_v^i - s_l^i \right|}{j-1} \qquad \text{Equation 5.2.10}$$

After removing the same number of worst solutions, the total size of the solutions did not change. This process ensures that only the best solutions are maintained so that these solutions effectively guide the ants in the search process[156].

When all generations of ants are exhausted, or three consecutive generations of ants return to the same solutions, the loop will be stopped. Because $\mathrm{F}_{\cos t}$ is the sum of all values of $F_{\text{condition}}$, the optimal solutions of $\mathrm{F}_{\cos t}$ can also be found as dynamic parameters.

When the ACO optimization process stops, the dynamic parameters need to be removed and returned to the SG filter to denoise each corresponding IMF. Finally, we obtain a clean VAG signal by reconstructing each denoised IMF.

5.2.2.3.3 Evaluation of the Effectiveness of the Proposed Method

The SNR and signal structural similarity are typically used to evaluate the denoising process. Furthermore, the peak SNR (PSNR) method was used to evaluate the denoising process. The PSNR can be seen as the ratio between the maximum possible power of a signal and the power of the corrupting noise. Although the PSNR is often used for two-dimensional image processing, the PSNR is also convenient for one-dimensional VAG signals.

Because VAG signals have few fixed-shape waveforms, a low-amplitude signal is easily masked b high-amplitude noise. The mean squared error (MSE) measures the signal process quality of an estimator, which is also the noise power in the PSNR. MSE can be defined as follows.

$$MSE = \frac{1}{N} \sum_{i=1}^{N} \left(a_i - b_i \right)^2 \qquad \text{Equation 5.2.11}$$

where N is the number of signal data points, a_i is returned by the process, and b_i is the actual value for datapoint i. MSE is always non-negative and yields a better result for values closer to zero.

The one-dimensional PSNR process can be defined by the peak value and MSE as follows:

$$PSNR = 20 \cdot \log_{10}\left(\frac{\mathrm{MAX}(a_i)}{\sqrt{MSE}}\right)$$ Equation 5.2.12

The method of comparing signal structural similarity was mainly performed using the Pearson correlation coefficient (PCC). The PCC is used to measure the strength of a linear association between two signals, where $r=1$ indicates a perfect positive correlation and $r=-1$ indicates a perfect negative correlation. The term r is obtained as follows:

$$r = \frac{\sum_i (c_i - \bar{c})(d_i - \bar{d})}{\sqrt{\sum_i (c_i - \bar{c})^2}\sqrt{\sum_i (d_i - \bar{d})^2}}$$ Equation 5.2.13

Where c_i and d_i are the individual original and processed signal data points indexed with i, and $\bar{c}$ and $\bar{d}$ are the corresponding signal mean values.

The percentage root mean square difference (PRD) can distort the measurement between the reconstructed and original VAG signals. As a percentage by which to evaluate the distortion measurement performance (lower is better) [157], the PRD is defined as follows:

$$PRD = \sqrt{\frac{\sum_{i=1}^{N}(e_i - g_i)^2}{\sum_{i=1}^{N}(e_i)^2}} \times 100\%$$ Equation 5.2.14

where e_i and g_i are the ith sample of the original and processed VAG signals, respectively.

5.2.3 Results and Discussion

he VAG signal waveforms after denoising using the standard and proposed methods are shown in Figure 5.2.4.

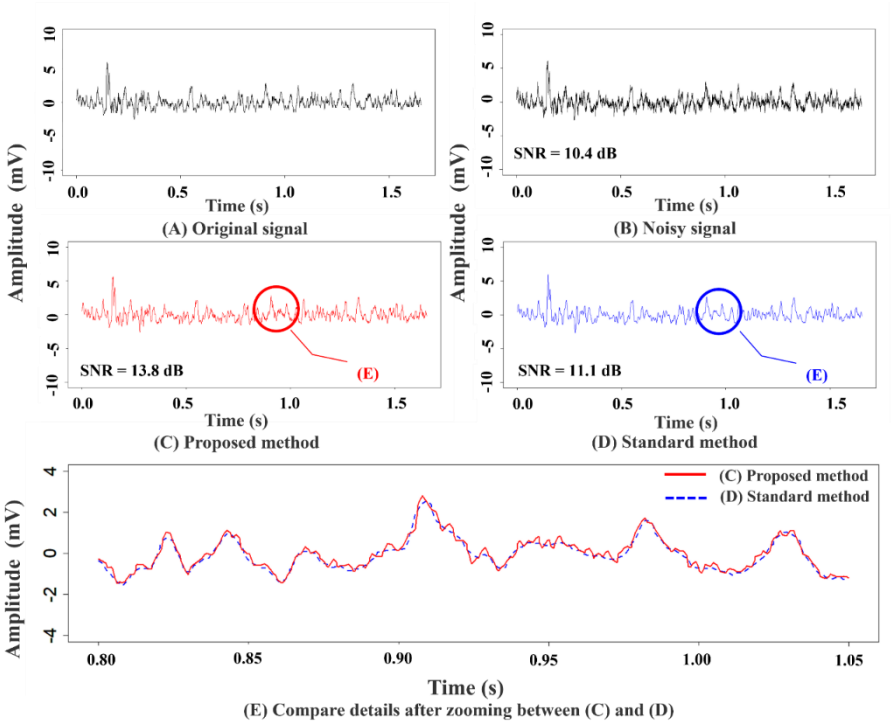

Figure 5.2.4 Waveforms of the proposed method and the standard method

In Figure 5.2.4, the waveform obtained using the standard method (D) is smoother than that obtained using the proposed method (C). However, the SNR of the waveform obtained using the proposed method (C) was greater than that obtained using the standard method (D). This is because the waveform obtained using the standard method (D) loses more details in the denoising process than the waveform obtained using the proposed method. As shown by the close-up (E), the waveform obtained using the proposed method (C) has far more mini-peaks than the waveform obtained using the standard method (D).

The results indicate that, for the denoising process, the proposed method retains more details (mini-peaks) because the ACO algorithm does an excellent job of differentiating the real signal and the noise, unlike the standard method without any calculation or optimization.

In fact, adding white noise to only one type of amplitude is insufficient. It is also necessary to verify the ability of the proposed method to reject noise of various strengths. By adding white noise of various strengths, noisy VAG signals were obtained from 0 to 25 dB. The signals were processed by the proposed method and the standard method, and the results for the mean value and standard deviation are shown in Figure 5.2.5

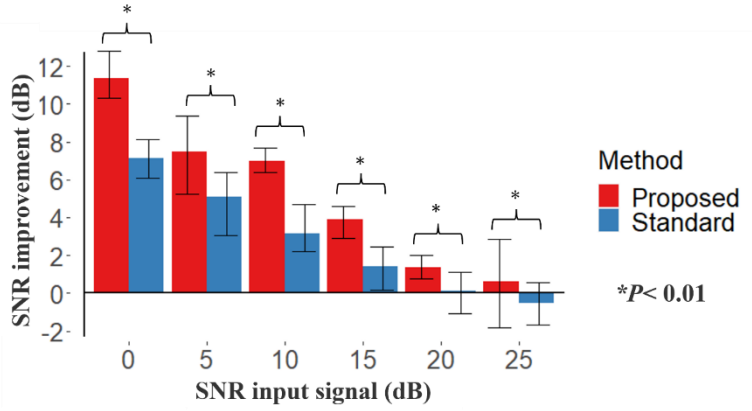

Figure 5.2.5 SNR improvement of the proposed method and standard method

The proposed method is superior to the standard method in terms of the SNR, as shown in Figure 5.2.5. However, as the input signal SNR increased, the improvement decreased significantly, either the proposed or standard methods (for all P-values less than 0.01 and a maximum P-value of 0.0057, by Student's t-test). When the SNR of the noisy input signal exceeded 20 dB, the improvement in the proposed method was almost negligible. However, the improvement in the standard method is negligible when the SNR of the noisy input signal exceeds 15 dB. Furthermore, the mean value of the improvement in the standard method is negative when the SNR of the noisy input signal is 25 dB.

The main reason for the occurrence of the SNR is the inability of standard methods to distinguish between white noise and mini-peaks. Conversely, in the proposed method, even though the mini-peaks and the white noise amplitude are very similar in a noisy VAG signal, the ZCR combined with EEMD can enhance the difference between mini-peaks and white noise by choosing the sub-signals. Moreover, the ACO algorithm optimizes the intensity of the denoising filter for each sub-signal based on the spectral flatness. Overall, the risk of negative SNR improvement was effectively controlled in the proposed method. This advantage is also observed in the PSNR, as shown in Figure 5.2.6.

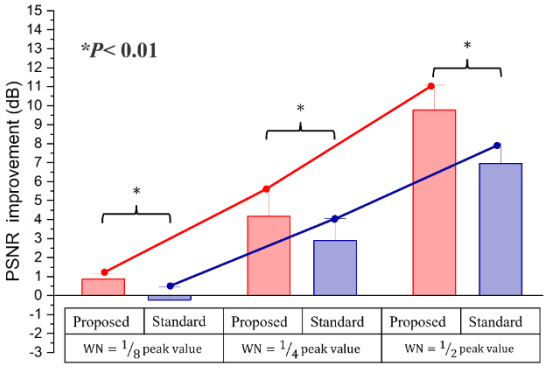

Figure 5.2.6 PSNR ratio improvement of the proposed method and standard method

In general, a higher PSNR indicates that the signal reconstruction is of higher quality after denoising. Equation 11 shows that the PSNR is determined by the peak value and MSE as the information quality. The PSNR improvement can also be defined as a correction of information quality. As shown in Figure

5.2.6, the PSNR improvement follows the same trend as the SNR improvement. The performance of the proposed method is always better than that of the standard method and increases as the white noise amplitude increases (for all P-values less than 0.01 and a maximum P-value of 0.0079, by Student's t-test.)

If the VAG signals are intended for clinical diagnosis of the knee joint, the signal structure should not be changed significantly by signal processing [158]. Although the proposed method performs well in noise reduction, its signal structure stability must be verified by PCC. As shown in Figure 5.2.7, the PCC was calculated between the original VAG signal and the clean signal obtained by the proposed method, between the original VAG signal and the clean signal obtained by the standard method, and between the original and noisy VAG signals.

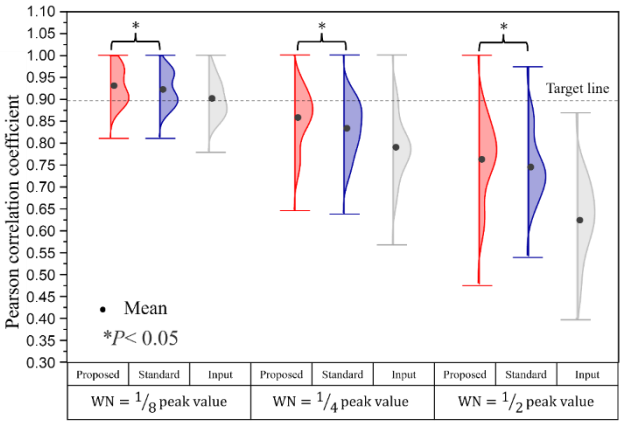

Figure 5.2.7 Structural similarity between signals

When low-intensity white noise was added, no significant increase was observed before or after the denoising process for either the proposed method or the standard method (for all P-values less than 0.05 and a maximum P-value of 0.044, by Student's t-test). This is because the addition of white noise does not sufficiently affect the original signal structure. Following an increase in the white noise intensity, the PPC increased after the denoising process but did not overtake the target line. The signals before and after the denoising process, for which the waveforms are not the same, must have the same characteristics. Therefore, the structural similarity expectation (target line) was set to 90%.

VAG signal decomposition and signal reconstruction are suspected to affect the structural stability of the VAG signal. Because the VAG signal has several mini-peaks, the reconstructed mini-peaks can easily shift in the time domain. Therefore, this study used various reference methods to verify this hypothesis.

A one-dimensional nonlocal means (NLM) filter and a discrete WT (DWT) filter are often applied to the denoising process of time-series biological signals and can be quickly performed using MATLAB Toolbox [107,156]. Nonlocal means is a direct denoising process (Path a in Figure 5.2.2), and DWT

is a denoising process after decomposition (Path b in Figure 5.2.2). Therefore, the filters with thresholds above were used for contrast.

The noisy signal was mixed with 0, 10, and 20 dB white noise as the input signal for each denoising process. The present study uses four indicators to compare the improvements in the denoising process: SNR, PSNR, PCC, and PRD. The results of the four methods are presented in Figure 5.2.8.

Overall, the results indicate that the proposed method and the DWT denoising filter are the best performers among the four methods. Although the results for the proposed method were slightly worse than those for the DWT denoising filter for an SNR of 20 dB and a PCC of 0 dB, the results for the proposed method were better than those for the other methods. This also indicates that the proposed method has room for improvement, especially with respect to the choice of filters with dynamic parameters. No more than, from the improvement of the denoising ability of the SG filter with a hybrid technology point of view, the proposed hypothesis is successfully verified because even if a signal with very high quality is input, the improvement can still be visible.

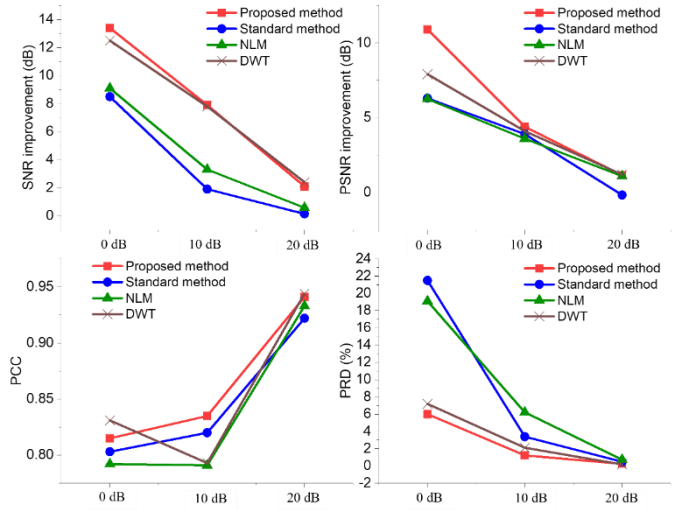

Figure 5.2.8 Denoising effects by the four methods examined in the present study

In addition, the proposed method is different from the DWT method, which decomposes the VAG signal using a high-pass filter and low-pass filter [159]. The proposed method decomposes the signal using EEMD, which involves only the amplitude components and not the frequency components. Because the ultimate goal of the present study is to apply the VAG signal to the clinical diagnosis of knee disorders, the proposed method can guarantee the VAG signal quality while beneficial for frequency-domain feature extraction in the next stage. Thus, we collected VAG signals of the abnormal knee and verified the practicality of the proposed method.

These VAG signals from the abnormal knee were also turned into input signals by adding white noise, as mentioned before. Their SNR improvements are shown in the left of Figure 5.2.9.

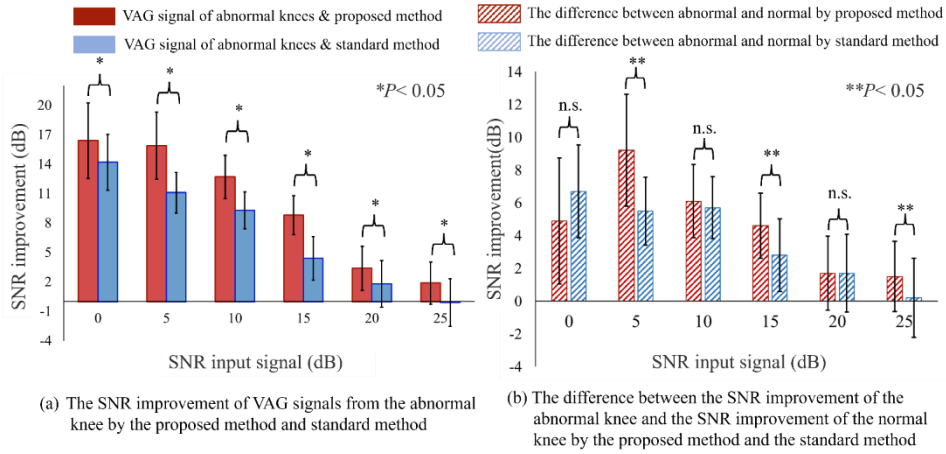

(a) The SNR improvement of VAG signals from the abnormal knee by the proposed method and standard method

(b) The difference between the SNR improvement of the abnormal knee and the SNR improvement of the normal knee by the proposed method and the standard method

Figure 5.2.9 The SNR improvement of VAG signals in normal and abnormal knees by proposed method and standard method

We can find that, the SNR improvements of the proposed method are more significant than the standard method for all SNR input signals of abnormal knee (for all P-values less than 0.05 and a maximum P-value of 0.027, by Friedman test.) The right of Figure 5.2.9 also indicates that the VAG signal of the abnormal knee is more easily to obtain an SNR improvement than the VAG signal of the normal knee both the proposed method and the standard method. The reason is the signal with steeper slopes, and sharper peaks are more easily denoised. In addition, we also compared the difference of SNR improvement between abnormal knees and normal knees by the proposed method and the standard method. The proposed method is lower than the standard method only when the SNR of the input signal is 0 dB, and the others are higher or equal to the standard method. After Friedman test as far as possible in 5 dB 15 dB 25 dB has significance, the others are not significant. The Figure 5.2.10 shows a comparison figure of the VAG signal of an abnormal knee before and after denoising processing.

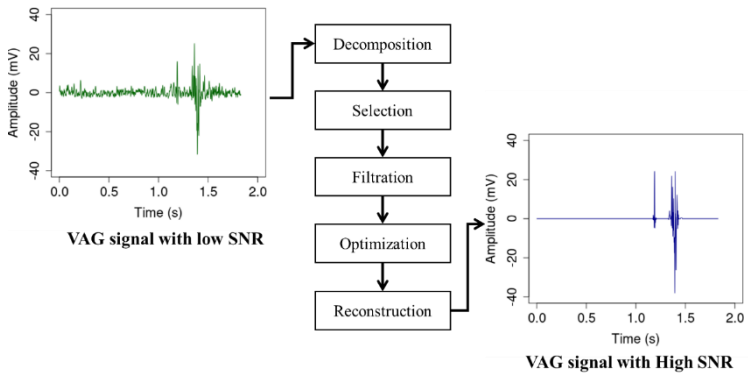

Figure 5.2.10 The VAG signal of an abnormal knee before and after denoising processing

As can be seen in the Figure 5.2.10, the VAG signal of the abnormal knee is more aggressive denoising than the VAG of the normal knee when the default ACO makes the filter optimization.

Therefore, the parameters of the ACO need to be adjusted to make it less reserved when processing the VAG signal of a normal knee. Finally, a simple comparison of the noise reduction effect of the different parameter values. A noisy VAG signal normal knee with length 5000 and SNR of 5 dB was the input. The denoised results are presented in Figure 5.2.11.

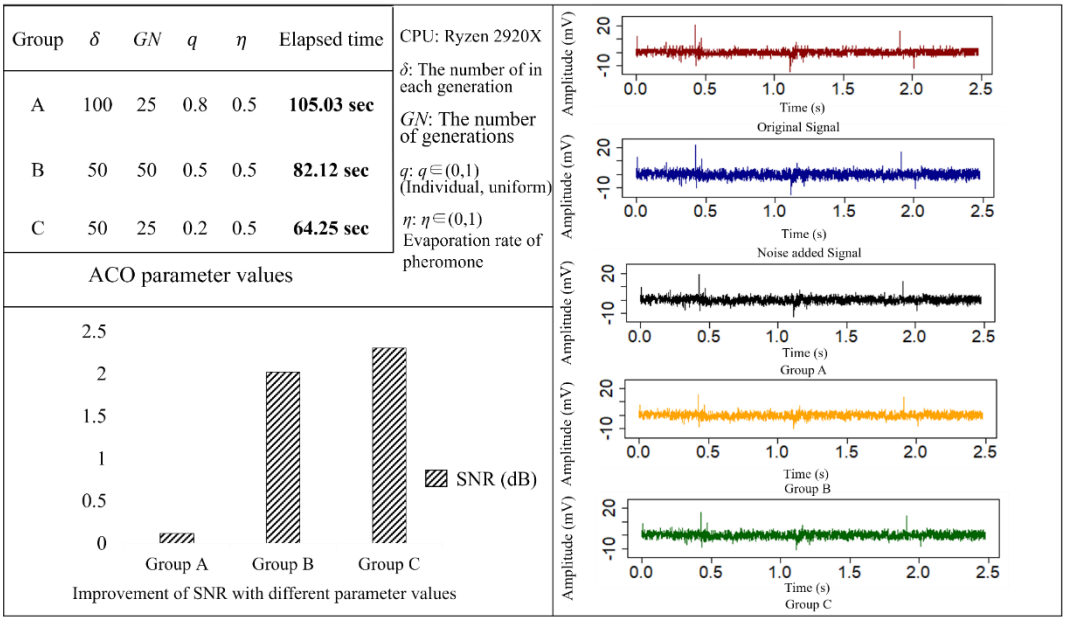

Figure 5.2.11 Denoising effects by different parameter's values of ACO

We found that increasing each generation takes more time than increasing the number of generations in the proposed method, and too many ants or generations will not bring better effects. Conversely, the parameter most affects the SNR improvement is q, which is of increased relevance to individuals or uniform distribution. For the VAG signal, increased relevance to uniform distribution can further improve signal quality. We hope that these recommended parameter values can be helpful when using the proposed method to process similar signals.

Although the proposed hybrid technology showed many benefits in this study, there are still some limitations. First, although the EEMD solves the mode mixing problem of EMD, there is room for improvement in decomposition. Future studies should investigate how the decomposition and reorganization of the signal can affects changes in the signal structure. The dynamic parameters of the SG filter can reduce any lost amplitude l to make the denoised signal closer to the real signal. Additionally, future studies should investigate the use of dynamic gain to repair any lost signal amplitude. Therefore, additional research is needed to improve and enhance noise reduction algorithms in the future.

In addition, for VAG signals, what is more important than noise reduction is how to keep noise out. Because, no matter how perfect the noise reduction filter is the real data will be lost, and this is not what we want to see. Therefore, it is necessary to minimize the noise generated in the experiment, starting from the method of sensor attachment, and considering the aspect of sitting and standing

movements.

5.2.4 Conclusion of this section

Noise interference in medical signals has become a significant problem, plaguing the advancement of emerging medical diagnoses. This interference has slowed the application of emerging diagnostic technologies. In particular, this is true for biological signals such as the mechanomyogram (MMG) and VAG signals. Although some noise can be traceable, such as that produced by body movements, and can be filtered out after signal component analysis, the source of most noise is uncertain. It may come from environmental interference, non-target biological signals, or electronic components, which are mixed and are usually referred to simply as random noise.

In the present study, based on the hybrid technology of EEMD and the SG filter, a combined ACO algorithm denoising method is proposed, and the improvement in the SNR of the VAG signal is verified. The results show that the proposed method rejects noise while ensuring that the real signal is retained. Overall, the denoising performance of the proposed method is better than the reference methods in terms of the VAG signal of either normal or abnormal knees.

Furthermore, the proposed method significantly improves the stability of the VAG signal quality and lays a foundation for the feature extraction and classification models that follow. This is attributed to the fact that the proposed hybrid technique does not need to modify the frequency components in any step, which is also a significant contribution of this study. Although there are limitations in the computational burden, the technique is still expected to extend the VAG signal to clinical applications.

The hybrid technique proposed in this study has not been isolated but has grown with the advancement of computer technology in recent years. The outstanding performance of the proposed method must rely on the ACO optimization algorithm and powerful calculations for support. As computer technology continues to advance, the process for this hybrid filtering method will become more efficient. This will ensure that denoising ability will become key to the advancement of biological signal processing technology.

5.3 Post-processing Algorithm for Removing Soft-tissue Movement Artifacts from Vibroarthrographic Knee-joint Signal

5.3.1 Introduction of this Section

The knee joint is a complex hinge-synovia structure that connects the lower leg to the thigh. It comprises a femur, a patella, a tibia, ligaments, meniscus, and cartilage. The knee is the largest joint and one of the most critical parts of the body, playing a vital role in lower-limb movement. However, it is very vulnerable to injury and wear, because it supports almost all bodyweight while providing normal movement[160].

Osteoarthritis (OA) occurs with cartilage degradation, breakdown, and damage characterized by loss of function and biochemical integrity of the joint cartilage [161].OA primarily affects people over 60 years, which causes pain and impacts normal life functions [162]. OA is complicated to treat, and surgery is often the only effective option. However, during the early grades of OA, physical therapy can relieve pain and delay deterioration. Thus, it is important to diagnose OA during its early stages accurately.

A new non-invasive diagnostic method can be achieved by collecting vibroarthrographic (VAG) signals of cartilage using an accelerometer or microphone placed on the skin surface. Details of the VAG signal can be associated with pathological conditions of the knee joint [81] and has achieved good results in distinguishing OA Grades III or IV according to the Kellgren–Lawrence Grading System [163,164]. However, VAG signal diagnoses at early stages of OA are not reliably discernable, because, during those early grades, the signal is weak and is highly susceptible to noise. The most substantial noise is caused by soft-tissue movement artifact signals. STMA is mechanical vibrations created by movements and friction of muscle, fat, and other soft tissue. The frequency is usually below 100 Hz [165]. During flexion and extension movements of the knee joint or standing movements, STMA signals from the quadriceps femoris and triceps surae interfere with the VAG signals of the articular cartilage, causing the baseline to wander. The state-of-the-art method in baseline wander removal are used adaptive filter to correct like Savitzky–Golay filter or notch filter [166]. These methods are commonly used in electrocardiogram signal processing, but are not very suitable for VAG signals, and need to be manually adjusted later. Therefore, we propose a post-processing method that can remove the STMA noise in the VAG signal and improve the accuracy of OA diagnosis.

In this paper, we measure the similarity of the removed STMA signal and the directly acquired STMA signal using a structural similarity index, the Pearson correlation coefficient, and the dynamic

time-warping distance to evaluate the proposed method. In addition, the proposed method can also be used in signal processing that is susceptible to baseline wander, such as electrocardiogram or electrooculogram. The diagnostic accuracy improvement of related diseases will be promising.

5.3.2 Data Acquisition

We employ a piezoelectric sensor (7BB-27-4L0, Murata) for VAG detection using a 16-bit resolution at an 8,000-Hz sampling rate with an accelerometer (TSND151, ATR) for collecting single STMAs with 16-bit resolution at a 200-Hz sampling rate.

We recruited some volunteers with knee discomfort without intense pain as subjects and obtained 36 sets of VAG data, of which 21 sets were from subjects over 60-years of age. None of these 21 sets senior subjects had been clinically diagnosed with OA by X-ray, but according to the questionnaire results there was a high probability that they were positive at early stages of OA.

The VAG sensor is fixed onto the skin over the tibia 10-cm below the Patella of the subject. The accelerometer set on the muscle side in the same horizontal position. The test subject, arms crossed over chest, is required to stand up from a sitting position. This movement is recorded by an electronic goniometer, as shown in Figure 5.3.1.

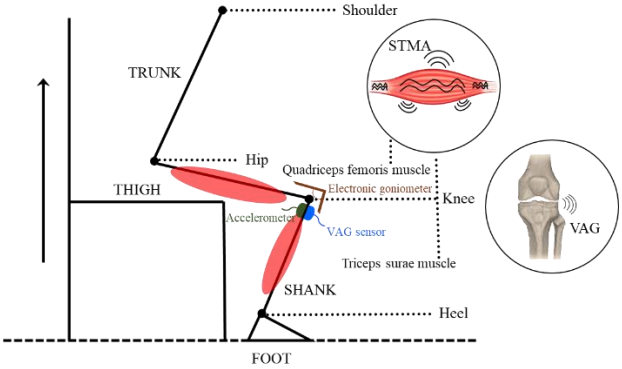

Figure 5.3.1. Measurement of VAG signal, STMA signal, and knee-joint angle

4.3.3 Methodology

When collecting VAG signals, STMA noise, random noise, and ambient interference are plentiful [88]. Usually, in a signal, the low-frequency part is the outline, and the high-frequency part is the noise and details. However, STMA is a type of baseline wander, which is a low-frequency noise, making it very difficult to remove.

So, the order of noise removal should be to remove the high- frequency and then the low-frequency. This is because the difference between the details and the high-frequency noise of the VAG signal is not obvious. We must separate noise from details carefully before deal with the baseline wander.

5.3.3.1 Random Noise and Ambient Interference Removal

First, we should remove random noise and ambient interference from the VAG signal. Then, use the

stationary wavelet transform (SWT) for denoising. The SWT overcomes the lack of translation invariance of the discrete wavelet transform (DWT) [167]. The SWT method in this paper involves the following steps:

a. Application of SWT to the raw VAG using a Haar wavelet as the basis function with decomposition up to 5 levels.
b. Application of fixed-form hard thresholding and unscaled white noise.
c. Reconstruction of the decomposed signal to obtain a cleaned signal.

The cleaned signal will still contain the baseline wander caused by STMA noise. The next step will remove it.

5.3.3.2 Soft-tissue Movement Artifact Noise Removal

The zero-crossing rate (ZCR) of a signal frame is the rate of sign-changes of the signal during the frame [168]. It reflects the number of times the signal changes value from positive to negative divided by the length of the frame. The ZCR is defined according to the following equation:

Let $x_i(n) = 0,1 \cdots N-1$ be the samples of the i^{th} frame.

$$Z(i) = \frac{1}{2N} \sum_{n=0}^{N-1} \left| \text{sgn}\left[x_i(n)\right] - \text{sgn}\left[x_i(n-1)\right] \right| \qquad \text{Equation 5.3.1}$$

Where

$$\text{sgn}\left[x_i(n)\right] = \begin{cases} 1, x_i(n) \geq 0 \\ -1, x_i(n) < 0 \end{cases} \qquad \text{Equation 5.3.2}$$

The moving-average filter is a simple finite impulse response filter commonly used for smoothing an array of the sampled signal. The filter acts with inadequate frequency-domain response and excellent time-domain response, usually removing the baseline wander [169]. The difference equation for an M-point discrete-time moving-average filter with input represented by the vector, b, and the averaged output vector, p, is

$$p[n] = \frac{1}{M} \sum_{k=0}^{M-1} b[n-k] \qquad \text{Equation 5.3.3}$$

The steps for removing STMA noise using the proposed method is as follows:

a. Application of DWT to the cleaned signal with a Haar wavelet as the basis function and decomposition up to 9 levels.
b. Calculate the ZCR value of each detail.
c. The first n details with ZCR values smaller than the threshold value is filtered using a moving-average filter, and the remaining details are retained.
d. The STMA noise is reconstructed by summing the processed details.
e. Subsampling the STMA noise to 200 Hz.

In our algorithm, the threshold value of the ZCR is set to 0.1 to more easily extract STMA noise from

the details. Because the moving-average filter is a low-pass filter, the pass part is chosen instead of the residual part when reconstructing STMA noise. The downsampling of the reconstructed signal to 200 Hz is for later comparison with the collected STMA signal by the accelerometer

5.3.4 Evaluation Method

Figure 5.3.2 shows a sample raw VAG signal denoising using the SWT method. It is difficult to find the difference between (B) and (C) just by observing the wave. Thus, we must introduce some methods, which are often used to evaluate the noise reduction result of audio signal or image signal [170].

We selected the root-mean-square error (RMSE), mean absolute error (MAE), peak signal-to-noise ratio (PSNR), and signal-to-noise ratio (SNR) to evaluate the noise reduction.

Similarity comparison is also important between the removed STMA noise with the collected STMA signal. The higher similarity, the baseline wander removal is more successful. During collection, owing to the noise caused by limb movements, we apply a 4th-order Savitzky–Golay filter to denoise the amplified STMA signal, and we also ignore the attenuation caused by different acquisition positions. The results are shown in the next section.

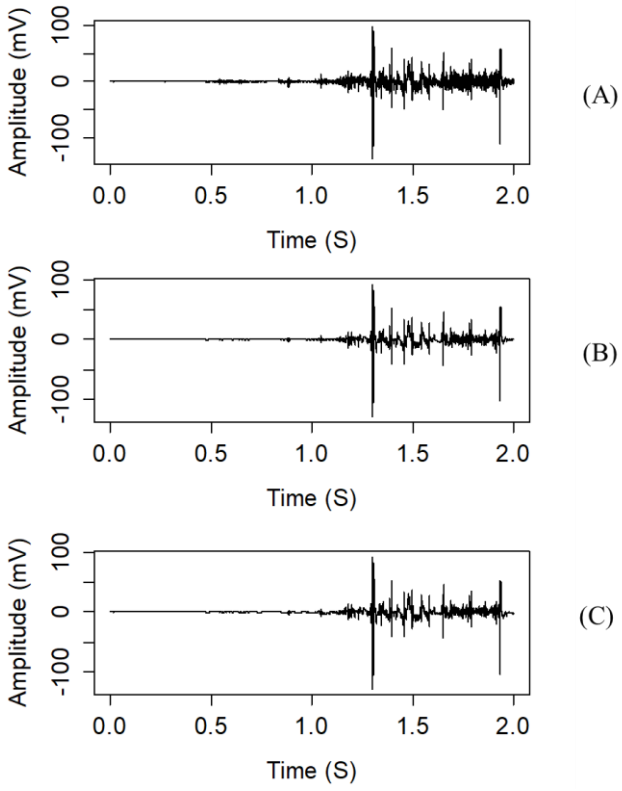

Figure 5.3.2 (A) Sample raw VAG single; (B) VAG signal after removing random noise and ambient interference; (C) VAG signal after removing STMA noise

5.3.5 Result

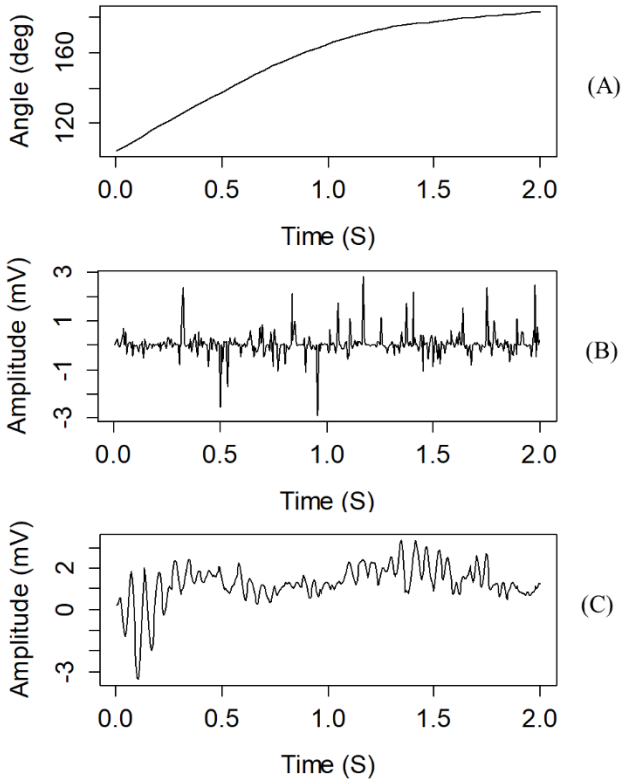

Figure 5.3.3 (A) Knee-joint angle is collected using an electronic goniometer; (B) STMA noise is reconstructed by downsampling; (C) the STMA signal is collected by the accelerometer.

From Figure 5.3.3, it is difficult to find the similarity between (B) and (C). Thus, we must break down the signal into 0.5s intervals and compare the similarity as shown in Table 5.3.1.

Table 5.3.1 Similarity of STMA Signal and STMA Noise

Metric	**Time (s)**				
	0–2.0	0–0.5	0.5–1	1–1.5	1.5–2.0
Angle change (deg)	86.67	46.47	23.76	13.11	3.674
SSIM	0.07869	0.0186	0.15087	0.05932	0.00378
PCC	0.05655	0.00786	0.10779	0.06189	−0.00715
DTW Distance (mV)	309.25	122.67	110.14	133.65	107.84

The higher structural similarity index (SSIM) value and the Pearson correlation coefficient (PCC) indicate higher similarity. By contrast, a higher dynamic time-warping (DTW) distance value indicates a lower similarity.

From Table 5.3.1, we observe that the 0–0.5-s knee-angle change is the most dramatic, but it gradually decreases. At 1.5–2.0 s, there is a slight angle change. The highest SSIM and PCC values appear within 0.5–1 s, whereas the lowest higher DTW distance value appears within 1.5–2.0 s.
We collected 21 sets of data for denoising using our proposed method and obtained results before and after processing. Then, we used a 2nd-order Savitzky–Golay filter for comparison [171].

Table 5.3.2 Comparison of the Average Value of Metrics Obtained Denoising 21 Raw VAG Signals.

Metric	STMA noise was not removed (only SWT method)	STMA noise was removed (after the SWT method)	
		proposed method	2nd Savitzky–Golay filters
MAE	2.1885	1.92085	2.1348
MSE	9.8434	7.97055	8.70885
PSNR (dB)	36.88	41.25	38.04
SNR (dB)	10.29	13.19	11.74

As can be seen from Table 5.3.2, by the proposed method, the maximum PSNR and SNR values were obtained. Furthermore, minimum MAE and MSE values were obtained. All were calculated by the raw signal.

5.3.6 Discussion

The similarity between the STMA noise extracted by the proposed method and the STMA signal collected by the accelerometer is not very high. This is because the transmission of STMA signals in biological tissue is attenuated, and there are different speeds of soft tissue and bone transmission. Therefore, there is a time difference in the arrival of the signals. However, signal similarity could be detected using DTW, even with different transmission speeds. Thus, we split the signal into four segments to calculate the DTW distance, finding that the second and fourth segments have higher similarity with transmission-speed influences.

Another reason is that the action of standing up causes a giant swing of the body, leading to interference with the acquisition of STMA signals. From Table 5.3.1, we find that the lowest SSIM and PCC values appear at the beginning and end of actions. This is because the volume of the soft-tissue changes and inertia caused by the start and stop actions caused the wave to drift.

The weight of the accelerometer is also a factor that should be considered. The mass of the accelerometer is 27 g, the mass of the VAG sensor is 6.5 g, and the mass ratio is 4.15. A lighter accelerometer would be more sensitive to STMA signals, but it would also be more susceptible to noise interference.

Our method obtains good results compared with the reference method of Table 5.3.2. A smaller error

indicates consistency with the original signal, whereas a higher SNR indicates that noise reduction achieved results. Furthermore, the proposed method outperforms the existing techniques by successfully correct baseline wander, meanwhile, almost no effect on the details of the VAG signal.

However, the result of denoising by the proposed method is not as high as expected. It can be seen from Figure. 5.3.4, that the L^2, elative-error norm does not make a significant difference.

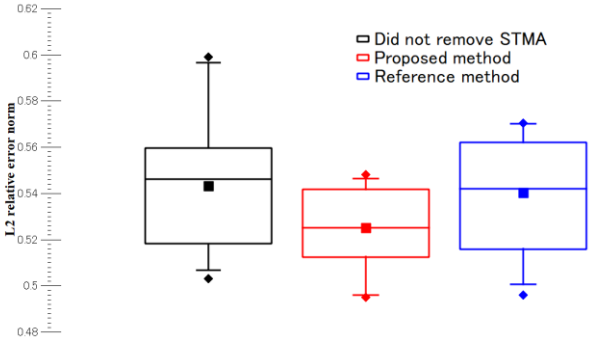

Figure 5.3.4 Boxplot of L^2 relative-error norm

Because the previous SWT method achieves decent noise reduction, the minimum value of the relative error of the reconstructed signal by the proposed method is nearly the same as the reference method. However, the maximum and average values of relative error are lower to explain the proposed method as effective, although it is limited. The best evaluation method is to manually add the STMA signal collected by the accelerometer to a clean signal and then calculate the SNR and error. This is work for a future paper.

In addition, there is a recent emerging technique to diagnose disease by measuring vibrations in muscle tissue known as MMG[89]. This coincides with the theme of this study, STMA is the displacement of muscle and fat, and is one of the future research directions of our team.

5.3.7 Conclusion of this section

We proposed a method to remove STMA noise from VAG signals and compared the similarity between the extracted STMA noise and the STMA signal collected by an accelerometer. We obtained good STMA noise reduction, but the similarity was not as good as expected. Thus, we split the signal in the time domain and calculated the similarity. We showed that the deformation and movement of soft tissues generated STMA and interfered with VAG signals. Therefore, this study should assist future studies seeking the construction of a knee OA diagnostic system based on VAG signals.

Chapter6

Feature Extraction and Classification

6.1 A Brief Review about Feature Extraction and Classification of VAG Signals

6.1.1 Feature Extraction

Feature extraction has many applications in machine learning, pattern recognition, and signal analysis. Feature extraction of the signals starts from pre-processed data and constructs informative and non-redundant derived values called feature values.

When feature extraction is applied to diagnose knee disorder based on the VAG signal (classification), it can be considered as a dimensionality reduction process for the complete VAG signal. Naturally, relying on just one or a few feature values is not enough to completely restore the original signal, so careful consideration is needed when choosing a feature extraction method.

The most common features are statistical features that are often extracted in the time domain.

A. Time domain features:

(A-1) Basic statistical features: including mean, standard deviation, root mean square (RMS), and shape coefficient.

(A-2) Higher-order statistical features: including the fourth-order moments (kurtosis) and third-order moments (skewness) of the biological signal.

Frequency domain features and information entropy features are also common feature extraction techniques.

B. Frequency domain features:

(B-1) Decomposes the function into frequency components using the Fourier transform and Fourier series.

(B-2) Includes amplitude features (amplitude spectrum) and phase features (phase spectrum).

C. Information entropy features:

(C-1) It is a measure of how much information is emitted by a VAG signal.

(C-2) Includes time domain entropy and frequency domain entropy

Since the VAG signal is an emerging biomedical signal in the clinical field, the feature extraction technique for its suitability is still referenced to other types of biomedical signals, as shown in Figure 5.1.1.

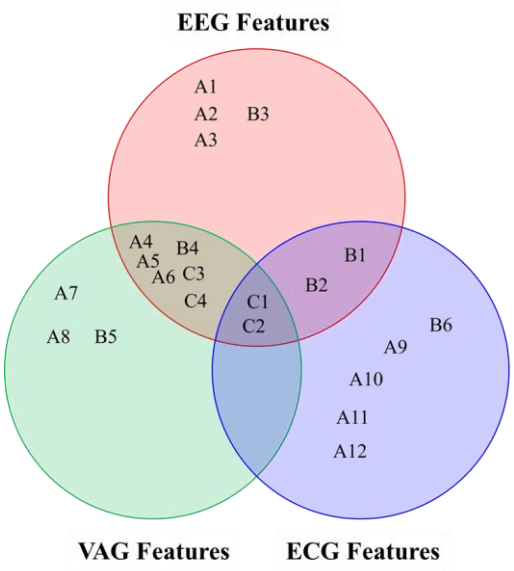

Number	Time domain (A)	Frequency domain (B)	Entropy-based (C)
1	RMS amplitude	Peak frequency	Shannon Entropy
2	Slope	Total spectrum	Spectral Entropy
3	Complexity	Mean power spectrum	SVD Entropy
4	Zero crossings	Median frequency	Fisher entropy
5	Kurtosis	Autoregressive Coefficients	
6	Skewness	Max Power Spectrum Density	
7	Mean Absolute Value		
8	Simple Square Integral		
9	4th Power		
10	Curve Length		
11	Nonlinear Energy		
12	The mean of RR intervals		

Figure 6.1.1 Suitability of feature extraction maneuvers in various biomedical signals

In addition to the above feature extraction methods, a new feature extraction method is proposed in this study, which will be introduced in the next section.

6.1.2 Classification Method

Though the first thing that comes to mind when it comes to classification methods today is machine learning-based classification methods, the most traditional way of classification is based on classical programming. The major difference between these two is whether the model used for classification is inductively summarized by humans or by machines, as shown in Figure 6.1.2

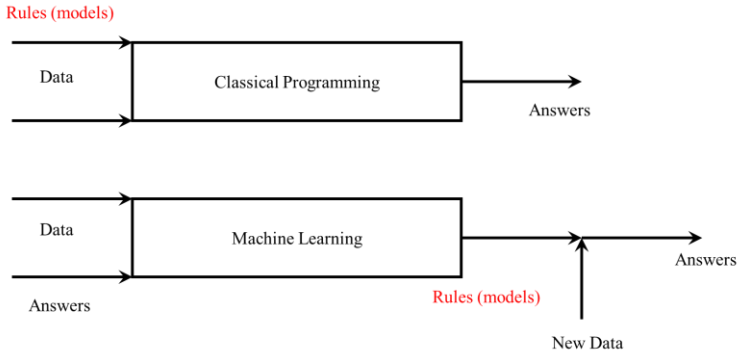

Figure 6.1.2 Two different ways of thinking about classification

Although data-driven mechanical learning classification methods have unparalleled performance and accuracy advantages over traditional classification methods, their interpretability is slightly lacking[172]. When VAG signals can be widely used for clinical diagnosis of the knee, the medical-ethical risks associated with a black-box model that is not understandable to doctors are more serious than expected. In this study, the interpretability of some common machine learning models is ranked,

as shown in Figure 6.1.3.

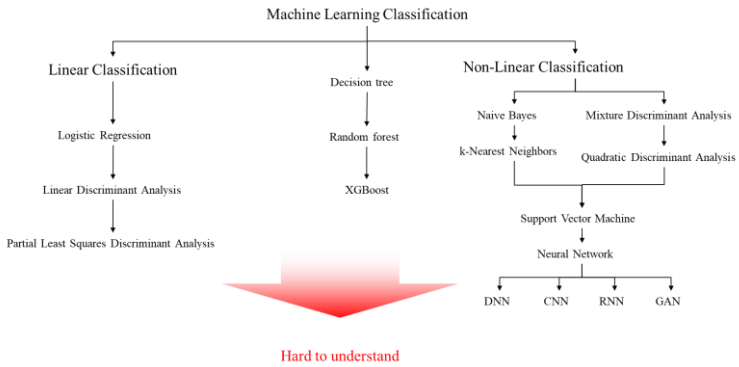

Figure 6.1.3 The interpretability of some common machine learning models

6.1.3 Conclusion of this Section

Classification based on feature engineering and machine learning is a new technique with many imperfections. In particular, the independence of the extracted features and the interpretability of the classification model are yet to be studied. However, this technology, combined with VAG signals, will occupy an important place in the future of next-generation medical diagnostics as a frontier technology for biomedical signal analysis methods.

6.2 A Plant Root System Algorithm Based on Swarm Intelligence for One-dimensional Biomedical Signal Feature Engineering

6.2.1 Introduction of this Section

1D biomedical signals are commonly used in the medical field and integral to clinical diagnosis and treatment. For example. The electrocardiogram (ECG) is commonly used for the diagnosis of heart-related diseases and the electroencephalogram (EEG) is used to detect sleep quality or the mental state[173,174]. Not only the electrical-based biomedical signals have good performance, but also magnetic-based, vibration-based, and acoustic-based biomedical signals are also making a splash in clinical applications[54,175,176]. On the other hand, with increasingly shorter sampling intervals and longer signal lengths, the analysis of 1D biomedical signals without computer assistance has come to the limit for researchers.

Although there are many kinds of computer-assisted 1D biomedical signal analysis, the cutting-edge analysis method is machine learning classification[177]. There is supervision classification, which is a machine learning technique that helps doctors improve diagnostic accuracy by training classifiers with features in biomedical signals [178,179]. This technique is very effective for complex and large datasets, and a well-designed classifier training model combined with some high-quality dataset features can often yield unexpectedly good results. However, the feature extraction method is not as highly versatile as model building, thus related research is less attention. Consequently, this study noted this weakness.

As a matter of fact, traditional and classical methods for feature extraction of 1D biomedical signals are not rare. For ECG signals, the curve length of the signal in the time domain and total spectral power in the frequency domain are both common features for classification[109]. For electromyography (EMG), a common biomedical signal uses the Shannon entropy as the EMG feature for classification in clinical fields[180].

These features may seem adequate, but the Naive Bayes classifier, which is the base of machine learning theory, requires that each condition be independent when the classification process. In other words, the biomedical signal features drawn from classical feature engineering techniques are not correlated with each other[181]. This independence between features is undoubtedly difficult to achieve because both time-domain and frequency-domain features can always be connected to each other by some operations and inverse operations. Fortunately, swarm intelligence computing seems to have opened up a new vision for feature engineering. When a feature based on swarm intelligence is

extracted, the new feature has distinguishing independence. This is because each member of the swarm participates in the choice, and the operations and transformations of the choice process are irreversible.

The swarm intelligence algorithm is famous for the ant colony algorithm[182]. The bee colony algorithm has been developed because of the swarming and social nature of bees[183]. Nowadays, dozens of named swarm intelligence algorithms are known, and many of them, such as particle swarm systems, have been applied to feature selection[184]. In this work, a swarm intelligence algorithm based on a plant root system (PRS) is proposed and tried to be applied to feature engineering.

Holker et al. [185,186] hypothesized that the root system of plants is a swarm intelligence system and that such systems are not limited to animals and humans. According to this hypothesis, root apices communicate with each other through electrical signals or chemical pheromones and then build a massive “brain-like” system in the underground world [187]. Within the complex root system, independent roots acquire water and nutrients through cooperation. At the same time, to support proper growth and development, the root system smartly competes with other root systems and chooses to start a “war” when it has an advantage or retreat when it is at a disadvantage[185,188]. Specifically for this work, the proposed PRS approach mimics the growth of plant roots, where the root apices cooperate to absorb as much of the sustaining nutrients as possible.

In our proposed approach, the base features used by the selected machine-learning model to classify biomedical signals are equivalent to nutrients in the digitized soil. These base features are features obtained from common feature extraction methods. In addition to these base features, the sum of the nutrients absorbed during growth serves as a first auxiliary feature; the growing area of the root system is the second auxiliary feature. These auxiliary features are referred to as PRS auxiliary features. In the model training process, the most significant advantage of the PRS features based on swarm intelligence is that they are not only ideally independent (i.e., they have low correlation with the other features), but they are also highly correlated with the dependent variable. The independence of the PRS features derives from the brain-like structure of the root system, where the co-determination of root tips reduces the correlation with the base features.

The advantages of this study are the PRS auxiliary features of biomedical signals are obtained from the proposed algorithm. The PRS features are appended to the training set, the decreased correlation between features results in a decrease in bias and variance and an increase in the accuracy of classification by machine learning. The biggest highlight of this study is that the PRS algorithm has universality for feature engineering of most 1D biomedical signals. This technology also enables 1D biomedical signals to become more competitive in the clinical field by improving the accuracy of machine learning classification.

6.2.2 Method

6.2.2.1 Extraction of base features

The growth of natural plants requires suitable soil; similarly, extraction of PRS features requires digitized soil composed of base features. When extracting base features, time-domain features are generally preferred to frequency-domain features and nonlinear features. For 1D biomedical signals with a non-stationary nature, the time-domain feature involves a lighter computational burden and has stronger reliability than nonlinear features [189]. Moreover, time-domain features also avoid the risk of spectral leakage caused by signal decomposition and is more dependable than frequency-domain features [190].

Time-domain feature selection is an extremely important process for base feature extraction. The number of features needs to be carefully considered: too few features will limit the growth of the root system, while too many features may adversely affect the performance of the classifier [191]. To comprise the set of base features, we selected 12 features that have relatively low computational complexity and that have been successfully used for classification with a high degree of accuracy [126,192,193]. Definitions of the base features are given in Table 6.2.1, where x_n represents the 1D biomedical signal in segment $\bar{x}$, N is the length of signal, and $\bar{x}$ is the average value of x_n.

Table 6.2.1 Time-domain features list

Base features	Definition	Equation
Standard deviation (STD)	$\mathrm{STD}=\sqrt{\frac{1}{N}\sum_{i=1}^{N}\left\lvert x_i-\frac{1}{N}\sum_{i=1}^{N}x_i\right\rvert^2}$	Equation 6.2.1
Variance of signal (VAR)	$\mathrm{VAR}=\frac{1}{N-1}\sum_{n=1}^{N}x_n^2$	Equation 6.2.2
Root mean square (RMS)	$\mathrm{RMS}=\sqrt{\frac{1}{N}\sum_{n=1}^{N}x_n^2}$	Equation 6.2.3
Skewness (SKW)	$\mathrm{SKW}=\frac{1}{N}\sum_{n=1}^{N}\left(x_n-\bar{x}\right)^3/\left(\frac{1}{N}\sum_{n=1}^{N}\left(x_n-\bar{x}\right)^2\right)^{3/2}$	Equation 6.2.4
Kurtosis (KURT)	$\mathrm{KURT}=\frac{1}{N}\sum_{n=1}^{N}\left(x_n-\bar{x}\right)^4\cdot\left(\frac{1}{N}\sum_{n=1}^{N}\left(x_n-\bar{x}\right)^2\right)^2$	Equation 6.2.5
Mean absolute value (MAV)	$\mathrm{MAV}=\frac{1}{N}\sum_{n=1}^{N}\left\lvert x_n\right\rvert$	Equation 6.2.6
Zero crossing (ZC)	$\mathrm{ZC}=\sum_{n=1}^{N-1}\left[\mathrm{sgn}\left(x_n\times x_{n+1}\right)\cap\left\lvert x_n-x_{n+1}\right\rvert\geq\ \text{threshold}\ \right]$	Equation 6.2.7

Slope sign change (SSC)	$\mathrm{SSC}=\sum_{n=2}^{N-1}\left[f\left[\left(x_n-x_{n-1}\right)\times\left(x_n-x_{n+1}\right)\right]\right]$ $f(x)=\begin{cases}1, & \text{if } x\geq \text{ threshold}\\ 0, & \text{otherwise}\end{cases}$	Equation 6.2.8
Willison amplitude (WAMP)	$\mathrm{WAMP}=\sum_{n=1}^{N-1} f\left(\left\lvert x_n-x_{n+1}\right\rvert\right)$ $f(x)=\begin{cases}1, & \text{if } x\geq \text{ threshold}\\ 0, & \text{otherwise}\end{cases}$	Equation 6.2.9
Simple Sign Integral (SSI)	$\mathrm{SSI}=\sum_{n=1}^{N}\left\lvert x_n\right\rvert^2$	Equation 6.2.10
Non-linear energy (NLE)	$NLE\left(x_n\right)=\frac{1}{N-2}\sum_{i=2}^{N-1}x_n(i)^2-x_n(i-1)x_n(i+1)$	Equation 6.2.11
Waveform length (WL)	$\mathrm{WL}=\sum_{n=1}^{N-1}\left\lvert x_{n+1}-x_n\right\rvert$	Equation 6.2.12

Among the 12 features comprising the set of base features, the most basic are the statistical features. These include variance (VAR) and standard deviation (STD), the most common statistics; the root mean square (RMS) amplitude, a statistical measure of the magnitude of a time-varying quantity; skewness (SKW), a measure of the asymmetry of the probability distribution of a real-valued random variable; kurtosis (KURT), the scaled form of the fourth moment and a measure of "peakedness"; and mean absolute value (MAV), which is similar to the average rectified value.

Three features related to frequency are also included: zero crossing (ZC), when the amplitude value of a signal crosses the zero-amplitude axis; slope sign change (SSC), representing the frequency information of a signal in the time domain; and Willison amplitude (WAMP), the sum of the difference between the signal amplitude for two adjacent samples.

The final three features are indicators of energy and complexity: The simple sign integral (SSI) is determined as the energy of a signal segment; nonlinear energy (NLE) is the approximative energy of signal amplitude; and waveform length (WL) serves as a measure of signal complexity.

6.2.2.2 Features sorting

For the development of a root system, the site where the seed is planted needs nutritious soil. In this study, the distribution of nutrients is equivalent to the distribution of the base features.

Each element $\beta_{m,n}$ of the base features set $B_{m\times n}\langle\rangle$ needs to be sorted. Before this is done, the dataset must be normalized using a scaling technique in the pre-processing stage to eliminate scale differences among the various elements when sorting. In this study, min-max normalization is to scale the data in the range [0,1]. The advantage of this method is that it can maintain the relationships that exist among the original data [194]. Here, the min-max normalization based on the features set $\dot{B}_{m\times n}\langle\rangle$ can be shown as

$$\dot{B}_{m\times n}\langle\rangle = \frac{\beta_{m,n} - B\langle\rangle_{\min}}{B\langle\rangle_{\max} - B\langle\rangle_{\min}} \qquad \text{Equation 6.2.13}$$

where n = 1, 2, …, 12 and m = 1, 2, …, length of β_n .

Feature importance measurement, or feature selection, provides the means by which the initial number of features can be reduced by eliminating those features with a low importance score for improving the performance of the classifier [195]. In this study, we chose not to delete features, but rather to sort features based on their worth score. To establish a feature's worth score, we measured the information gain associated with the feature; the features with higher worth scores were those closer to the center location. Information gain was first shown in a decision tree and used to rank the priority of feature nodes; this was then expanded and applied to our importance measurement [196].

Let the class label of a feature have two distinct values defining binary classes $\{C_1, C_2\}$. $\mathrm{Info}(\dot{B})$, also known as the entropy of $\dot{B}_{m\times n}\langle\rangle$, can be defined as follows:

$$\mathrm{Info}(\dot{B}) = -p_1 \log_2(p_1) - p_2 \log_2(p_2) \qquad \text{Equation 6.2.14}$$

where p_1, p_2 is the nonzero probability that an arbitrary tuple in $\dot{B}_{m\times n}\langle\rangle$ belongs to class C_1, C_2 and is estimated by $|C_{1 \text{ or } 2,\dot{B}}| / |\dot{B}|$.

Since each feature column $\dot{\beta}_n$ is a set of discontinuous values, these discrete values of $\dot{\beta}_n$ need to be split into two sets using an unsupervised algorithm. The K-means clustering method is a good choice for partitioning the given data set into k groups, where k represents the two groups pre-specified by the analyst [197]. In this study, this process is repeated 25 times to produce lower within-cluster variation and a more stable result. Each $\dot{\beta}_{m,n}$ now belongs to splitting set $\{s_n^1, s_n^2\}$ and has a class label. Then the expected information required to classify the tuple from $\dot{B}$ based on feature $\dot{\beta}_n$ is

$$\mathrm{Info}_{\dot{\beta}_n}(\dot{B}) = \sum_{i=1}^{2} \frac{|\dot{B}_{s_n^i}|}{|\dot{B}|} \times \mathrm{Info}\left(\dot{B}_{s_n^i}\right) \qquad \text{Equation 6.2.15}$$

$$\mathrm{Gain}\left(\dot{\beta}_n\right) = \mathrm{Info}(\dot{B}) - \mathrm{Info}_{\dot{\beta}_n}(\dot{B}) \qquad \text{Equation 6.2.16}$$

The $\dot{\beta}_n$ with the highest information gain is chosen to replace the center of $\{\dot{\beta}_1, \dot{\beta}_2, .., \dot{\beta}_{12}\}$, and the other features are sorted, one-by-one, from the center to the two sides, with decreasing information gain. In this way, a sorted base feature set is obtained.

6.2.2.3 Generating nutritious soil based on features

In this study, the digitized soil consisting of the sorted base features set cannot have only width and not depth. Therefore, continuous feature discretization is necessary (from scalar to vector). In this process, equal width interval binning is perhaps the most common method to discretize data for producing nominal values from continuous features [198]. With this binning method, if a feature a is observed to have values bounded by $a_{\max}$ and $a_{\min}$, then the method computes k equally sized bin

widths

$$\delta = \frac{a_{\max} - a_{\min}}{k}$$ Equation 6.2.17

and constructs bin boundaries at $a_{\min} + j\delta$ where j = 1, 2, … , k-1. In order to be closer to the natural environment of the root system, we set k = 15.

In addition, the vertical distribution of soil nutrients should follow, to the extent possible, the laws of nature. Most nutrients are concentrated in the shallowest layer and decrease with depth since nutrients return to the soil through biomedical cycles [199]. Thus, the discrete feature set $d_{15\times12}$ is arranged in decreasing order from top to bottom. On the other hand, the horizontal distribution of nutrients is associated with the crustal movement. The kernel convolution values τ_A and τ_B are used to calculate the reconstituted nutrient distributions.

The nutritional reconstructions are divided into two types: τ_A affects the nutrient distribution from shallower layers, while τ_B affects the nutrient distribution from deeper layers. The convolution kernel is then be defined as

$$\tau_A = \frac{1}{2}\begin{bmatrix} 1 & 1 & 1 \\ 0 & 1 & 0 \\ 0.5 & 0.5 & 0.5 \end{bmatrix}$$ Equation 6.2.18

$$\tau_B = \frac{1}{2}\begin{bmatrix} 0.5 & 0.5 & 0.5 \\ 0 & 1 & 0 \\ 1 & 1 & 1 \end{bmatrix}$$ Equation 6.2.19

The nutritious soil used to generate the root system is written as $D_{15\times12}$, which results from the convolution of $d_{15\times12}$ with kernel τ_A and τ_B. The calculated target matrix requires zero-padding with size one before each convolution.

The completed soil with the mineral nutrition generation process is shown in Figure 6.2.1. Hereinafter, the matrix for the distribution of nutrients in the soil will be referred to as the “nutrient matrix.”

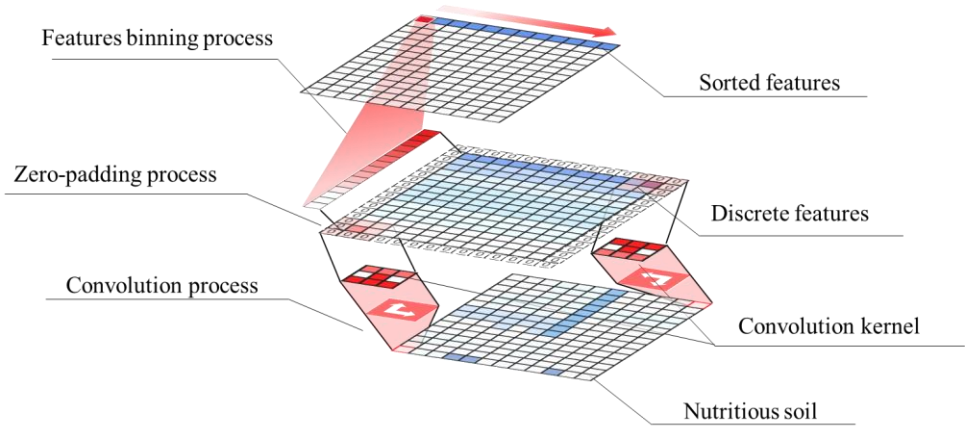

Figure 6.2.1 Soil with the mineral nutrition generation process

6.2.2.4 Plant root system algorithm

In plants, the radicle, or primary root, is first organ to emerge from the seed coat. Before the first leaf grows, the energy needed by the cotyledon for root development all comes from the seed itself. Additional inorganic nutrition (including water) is also essential; only a small part of this nutrition comes from the seed itself, with the remainder coming from the surrounding soil containing mineral nutrients [200,201] The rule inherent in the genes of higher plants is to develop a sufficiently large first leaf and sufficiently long roots before the energy stored in the seeds is exhausted. The algorithm we propose follows this same rule. Since organic matter cannot be synthesized through photosynthesis before the first leaf has grown, the task is to absorb more mineral nutrients by growing a sufficient root system using limited energy (root division) in a limited time. Hereinafter, the matrix distribution for the roots in the soil will be referred to as the "root matrix."

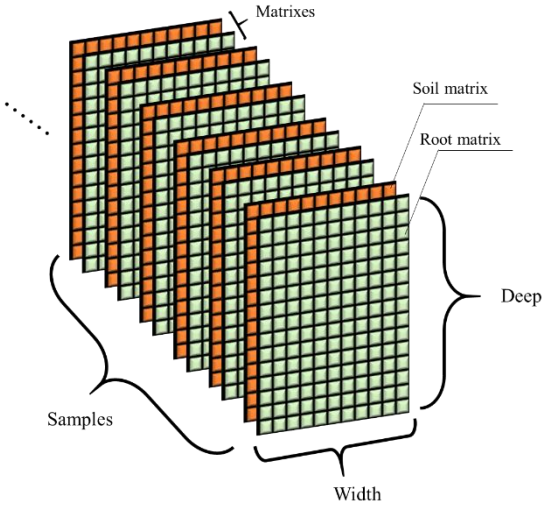

Figure 6.2.2 A 4D data tensor of biomedical signals

In our proposed approach, the above natural processes need to be transformed into a data processing program. First, the root matrix and the nutrient matrix form a 4-dimensional tensor, as shown in Figure 6.2.2. The initial root matrix is a zero matrix, where the upper center location assigning values can create a radicle matrix. To absorb more nutrients, the rule of root division is to preferentially proliferate at the location of the global maximum in the mapping nutrient matrix; at the same time, location neighbor root-tips are necessary. The radicle matrix, photosynthetic day, and daily root division are then available as parameters to be modified. The development process can be characterized by the root distribution area and total nutrient absorption. Figure 6.2.3 shows the natural process and digital process of building a brain-like root system. In Figure 6.2.3, we can see that the growth of digital roots is dependent on the base features. Usefully, by drawing out PRS features from the brain-like root system, correlation with the base features is reduced.

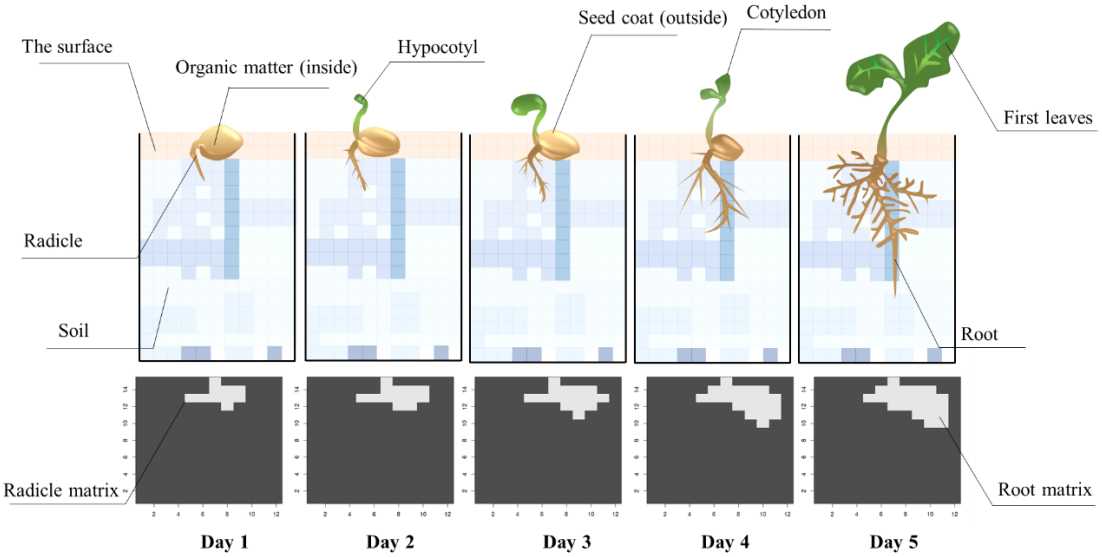

Figure 6.2.3 The natural process and digital process of building brain-like root systems.

The growth process of the roots can be written as pseudocode, as shown in Table 6.2.2. In the proposed algorithm, the core steps of root development involve seeking the global maximum location of the nutrient matrix map relative to the root matrix location using a tensor of the base features set of a biomedical signal. The entire root system makes its decisions jointly in brain-like fashion to improve total nutrient absorption.

Table 6.2.2 Plant root system algorithm

Algorithm 1 Plant root system

Input:
  $\mathbb{DR}_{x\times y}$: distribution of the radicle in the soil (initial root matrix); ▷x, y are the number of rows and columns of the distribution matrix respectively
  $\mathbb{DN}_{x\times y}$: distribution of nutrients in the soil (nutrient matrix);
Output: ▷
  na : nutrients absorbed by the roots;
  A : root distribution area;
$na \leftarrow 0$; ▷ $\mathbb{R}_{x\times y}$: distribution of the growing root in the soil (root matrix)
$\mathbb{R}_{x\times y} \leftarrow \mathbb{DR}_{x\times y}$;
for $i = 1 \rightarrow day$ **do** ▷ day is the days for first leaf to appear
  for each $\mathbb{R}_{[x^{th},y^{th}]} = 1$ **do** ▷ $x^{th} \in (1,2,\cdots x) y^{th} \in (1,2\cdots y)$
    $m \leftarrow \left\{\mathbb{DN}_{[x+1^{th},y^{th}]}, \mathbb{DN}_{[x-1^{th},y^{th}]}, \mathbb{DN}_{[x^{th},y+1^{th}]}, \mathbb{DN}_{[x^{th},yth-1]}\right\}$; ▷ $\mathbb{R}_{[x^{th},y^{th}]} \in \mathbb{R}_{x\times y}$ $\mathbb{N}_{[x^{th},y^{th}]} \in \mathbb{DN}_{x\times y}$
  return m to $\mathbb{M}$; ▷ $\mathbb{M}$ is a matrix
  end for each
  decreasing sort $\mathbb{M}$ **to** M; ▷M is a vector
  for $j = 1 \rightarrow l$ **do**; $(l \leq$ length of $M)$ ▷ l is a limit of root division in one day
    $M[j]$ **mapping back to** $\left[x^{th}, y^{th}\right]$; ▷$\left[x^{th}, y^{th}\right]$ is a location of the matrix
    if $\mathbb{R}_{[x^{th},y^{th}]} \neq 1$ **do**
      $\mathbb{R}_{[x^{th},y^{th}]} \leftarrow 1$;

19 $na \leftarrow \begin{cases} 0, M[j]=0 \\ \dfrac{M[j]}{1+|M[i]|}+0.49, M[j]\neq 0 \end{cases}$ ▷absorption rate

20 **end if**

21 **do** na ++;

22 **return** na **and** $\mathbb{R}_{x\times y}$ ▷na is the first output

23 **end for**

24 **do** $\dot{\mathbb{R}} \leftarrow \mathbb{R}$ ▷the root extraction as polygon

25 **do** $A \leftarrow area(\dot{\mathbb{R}})$; ▷ area of the polygon A is the second output

26 **return** A;

27 **end procedure**

In this procedure, the roots distribution can be drawn in a coordinate system as a polygon. The area of this polygon serves as a feature. For the polygon area calculation, we used the tool developed by Bourke [202], which is one of the most well-known of such tools. The procedure outputs two results: the total amount of nutrients absorbed during root system development, designated the nutrition feature (NF), in row 24 of Table. 6.2.2, and the area of the roots distribution, designated the root feature (RF), in row 27 of Table. 6.2.2. Both are referred to as PRS features.

$$A=\frac{1}{2}\sum_{i=0}^{N-1}\left(p_i q_{i+1}-p_{i+1}q_i\right) \qquad \text{Equation 6.2.20}$$

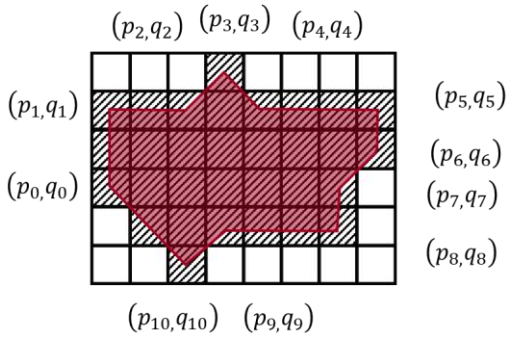

Figure 6.2.4 An example of a 10-vertex closed polygon constructed from a root matrix

The calculation of NF and RF is shown as na (nutrient amount) and A (area), respectively, in Table 6.2.2. The calculation of A is derived from Equation 6.2.20 and Figure 6.2.4, where the polygon is closed and made up of line segments between N vertices (p_i , q_i), i = 0 to $N-1$.

Incorporating the extracted PRS features into the unprocessed base features set produces the set for classification, composed of 14 features. Lastly, the final features set is obtained by again performing a min-max normalization.

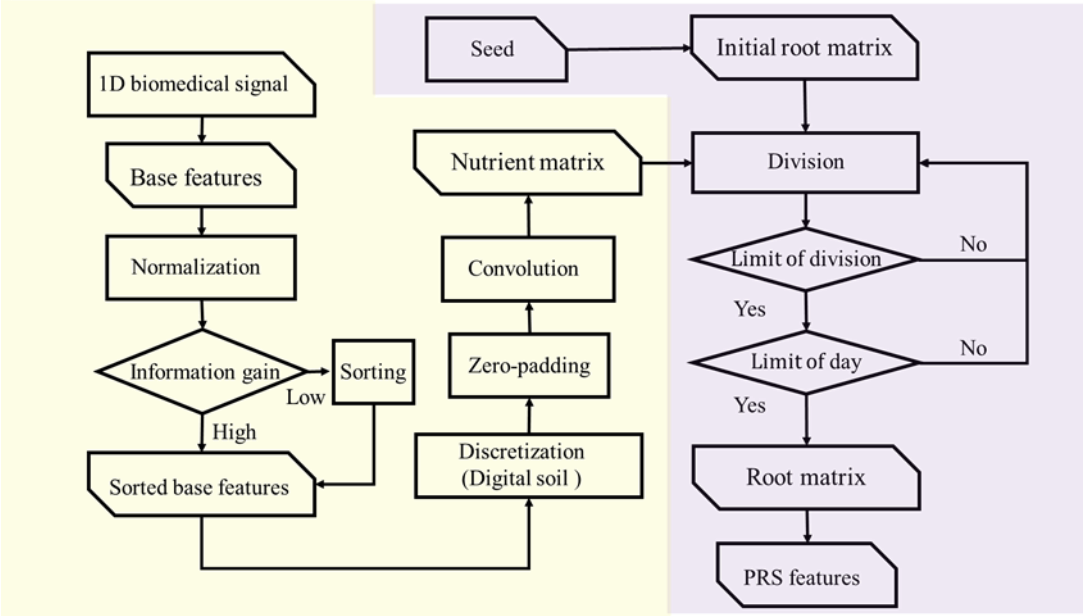

Figure 6.2.5 A flowchart from data processing (left) to algorithm implementation (right)

At the end of this section, the flowchart in Figure 6.2.5, is used to re-explain the process of extracting PRS features. The entire process is divided into two parts. The first part is to make a nutrient matrix of the common features. The core idea of this part is how to make a digitized soil with an appropriate size and nutrient distribution by mathematical calculation between the features. The second part is the development of the root matrix through the nutrient matrix and the seed. The core idea of this part is to limit the root division rule for radicles by parameters.

6.2.3 Datasets and evaluation methods

In this study, the accuracy of various classifiers is used for evaluation. The key measurable for each classifier is the change in accuracy before and after adding the root-based features to the original feature set. Accuracy, also known as the correct rate, is often used in epidemiology [203]. For a sample, a correct classification is true, and an incorrect classification is false. The sum of the number of correct samples divided by the sum of all samples is the accuracy. Accuracy is usually a percentage. A result is closer to 100% will be more correct.

$$\text{Accuracy} = \frac{TP + TN}{TP + FP + TN + FN} \qquad \text{Equation 6.2.21}$$

where TP = True positive, FP = False positive, which is true and false for positive samples. TN = True negative; FN = False negative, which is true and false for negative samples.

6.2.3.1 Datasets

When selecting a dataset of biomedical signals, a non-stationary signal is preferred. In fact, nearly all biomedical signals are non-stationary since the human system is always in dynamic equilibrium under the regulation of the brain [204]. Accordingly, three biomedical signals were selected in our

study: the vibroarthrographic signal (VAG), which is the vibration signal generated by the friction between the knee cartilage during flexion-extension movement to detect knee joint disorder[54,55]; the EMG of the forearm, which is the electrical signal generated by the extensor carpi radialis longus during the fist-relax movement [205]; and the audio signal collected via a smartphone web app [176] of a cough coming from lungs and airways that may or may not be affected by COVID-19. All the above signals are binary class signals—young or old for the VAG signals, rest or fist for the EMG signals, and positive or negative for the cough sound signals. Table 6.2.3 describes the properties of these signals in detail.

Table 6.2.3 Properties of the biomedical signals

Dataset	Signal type	Class	Sample size	Sampling rate	Length	Noise reduction
VAG of knee joint	Vibration signal	2	144	2000 Hz	3k–5k	Yes
EMG of hand	Electrical signal	2	72	1000 Hz	3k–5k	No
Sound of coughing	Sound signal	2	121	22.5 kHz	60k–80k	No

6.2.3.2 Evaluating the PRS features

6.2.3.2.1 Verification by different classifiers

Generally speaking, the selection of classifiers for feature testing should follow the principle of interpretability, excluding black boxes to the extent possible[206]. As the principal linear classifier in this study, we chose the logistic regression (LR) model. LR has been widely used in classification problems and offers the benefit of outputting probabilities. However, an LR classifier is also limited by these probabilities. A result of 51% or even 99% pointing to a given class can produce mismatching [206,207]. In contrast to LR, which focuses on maximizing the probability of group membership, a support vector machine (SVM) seeks to find the separating hyperplane that maximizes the distance of the closest points to the margin. Since the feature sets involve more than 12 dimensions, we chose a polynomial kernel-based nonlinear SVM as the main nonlinear classifier in the study. In addition, we used linear discriminant analysis (LDA) and quadratic discriminant analysis (QDA) as complementary classifiers to the LR and SVM classifiers. Together, these four kinds of machine learning-based classifiers were used to test the feature set.

6.2.3.2.2 Extraction method for the comparison set features

Feature extraction methods for biomedical signals commonly use both time-domain features and frequency-domain features. Since all the base features in this study are time-domain features, we used two frequency-domain features to complete our comparison feature set [109]. Specifically, we used max power spectrum density (MaxPSD) and median power spectrum density (MedPSD) as the auxiliary features to the base features in the comparison set. The two frequency-feature extraction techniques were based on the Fourier transform [109]. By incorporating the extracted MaxPSD and

MedPSD measures into the unprocessed base features set, the comparison set included the same number of features (14) as the experimental set. As a final step, the comparison set was normalized using min-max normalization. Having established the comparison set, we then proceeded to compare the accuracy of the PRS sets and the comparison set.

Implementation of the signal processing, feature engineering, the PRS algorithm, and the classifiers was supported by RStudio and related packages [208–211].

6.2.4 Results

Four datasets were input into each of the classification models chosen for the study: The first was the base set containing only the 12 time-domain features, which are described in Table 6.2.1. The second (base + NF) and third (base + RF) sets each contain one PRS feature and the 12 time-domain features, for a total of 13 features. The last set was the PRS set with all features, 14 in total.

All four datasets from the VAG signal, the EMG signal, and the cough signal were input, one by one, into the LR classifier, the SVM classifier, the LDA classifier, and the QDA classifier. Each classifier was trained with learning rates of 40% to 80% of the full samples (in increments of 10%). The remaining samples were used as test data. Classification accuracy was then calculated using Equation 6.2.21. The results for the VAG signal, EMG signal, and cough signal are summarized in Figures. 6.2.6 – 6.2.8. The vertical coordinate in the figures is the average accuracy of 100 classifications using the various learning rate with one-way ANOVA test after Shapiro test.

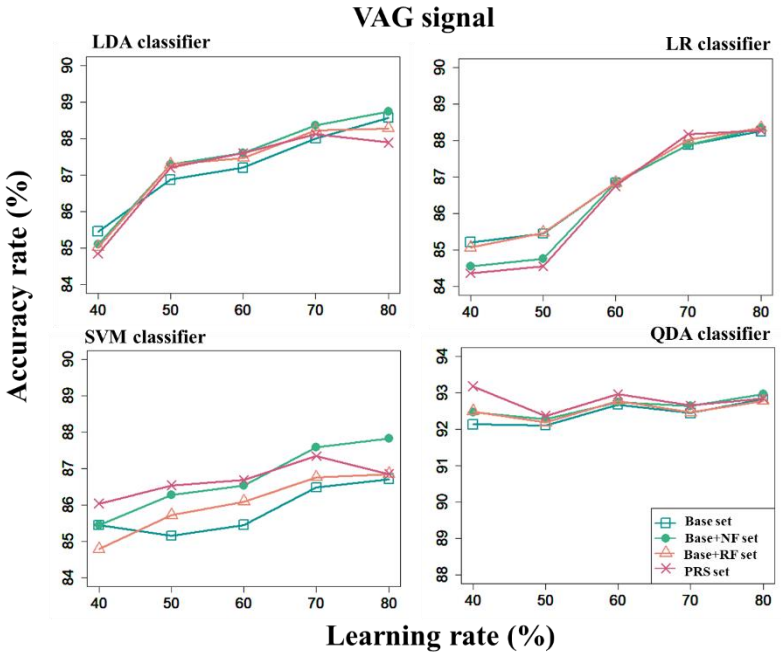

Figure 6.2.6 Accuracy of the VAG signal for the four classifiers (significant, $F \in [4.22, 4.58]$, $p \leq 0.05$)

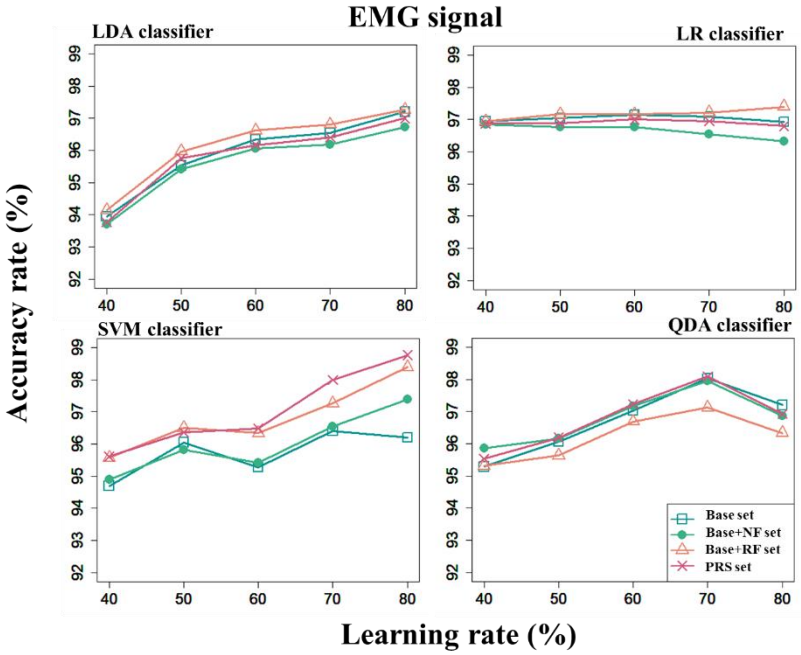

Figure 6.2.7Accuracy of the EMG signal for the four classifiers (50% LR classifier: quasi-significant, $F = 2.296$, $p = 0.0722$; Others: significant, $F \in [4.04, 4.39]$, $p \le 0.05$)

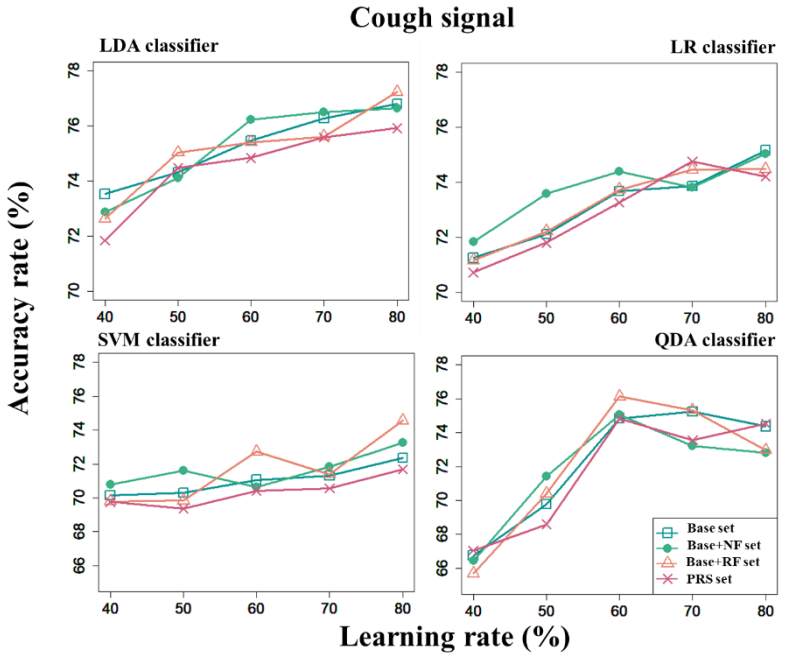

Figure 6.2.8 Accuracy of the Cough signal for the four classifiers (significant, $F \in [4.24, 4.79]$, $p \le 0.05$)

As can be seen in each figure, all input sets for the three types of biomedical signals show an increasing trend in the accuracy rate when the training rate increases. However, the results stand out

most because the sets that include NF feature or RF feature show a greater accuracy than when only the base set is used. This result is consistent with the prediction of this study that the new feature by the algorithm as a control variable that is less correlated with other existing variables, pulling down the correlation between variables overall and reducing the bias in training, and improving classification accuracy.

The details are as follows. First, focus on the VAG signal in Figure 6.2.6, the input sets containing the nutritional feature (NF) tend to perform better. Here, the QDA classifier with the set containing the nutritional and root features has the highest classification accuracy. Further analysis indicates that when the training rate is increased to 80% for the LR classifier, classification accuracy using the base set improves by 3.12%, while that for the base+NF set improves by 3.65%. Figure 6.2.7 indicates that the classification accuracy for the EMG signal is particularly high for all four classifiers, in some cases as high as 98%, a value much higher than the maximum values for the other biomedical signals. The set containing NF or RF possessed a higher accuracy in the vast majority of conditions, but an accident occurred when the QDA classifier was at 80% training rate. Figure 6.2.8 shows that the cough signal is less accurate and regular than the other signals. Here, the largest accuracy improvement in this study occurs at 60% training rate of the QDA classifier, an improvement of about 10% compared to the initial stage. In addition, although the accuracy was monotonically increasing in trend as the training rate increased, there were several monotonic changes in all biomedical signals. This result is most likely due to errors during random sampling, so a repetitive sampling comparison was implemented as the following.

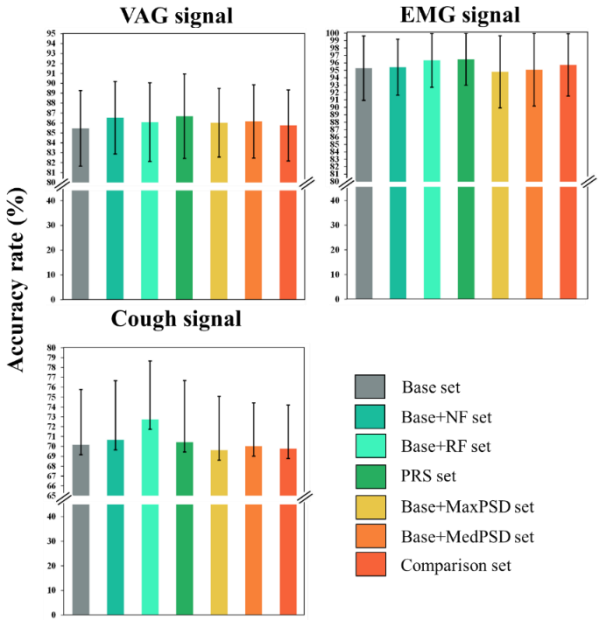

Figure 6.2.9 The accuracy of the PRS sets and comparison sets with a 60% learning rate for the SVM classifier.

The vertical coordinate is the average accuracy for 100 times classification; the error bar indicates the standard deviation ($p \leq 0.05$)

Figure 6.2.9 compares the accuracy of the base set, the sets containing the PRS features, and the sets containing frequency domain features using a 60% learning rate for the SVM classifier. A Tukey multiple comparisons test of means using a 95% family-wise confidence level was performed on the raw data shown in the figure. For the VAG signal, the average differences between the sets containing PRS features, and the base set were all greater than 3.71%; the average differences for the sets containing PRS features and the sets containing the frequency domain features were all greater than 1.63%. All the p-values were less than 0.05. The EMG signal and the cough signal followed this same pattern.

Overall, the results indicate that the sets containing only the base features had a consistently lower accuracy rate and that the sets containing the PRS features had a consistently higher accuracy rate.

6.2.5 Discussion

For VAG signals, the sets containing PRS features showed a maximum accuracy of 93%, which is a higher rate than has been reported in all relevant past studies[54,55]. These results agree with Rauber's (2015) findings, which showed that using only appropriate features could improve the performance of classifiers [191]. For cough signals, although the sets containing PRS features did not achieve the 80% accuracy reported by Chaudhari (2015), who used thousands of samples and deep learning to produce his results, our method achieved 76% accuracy with only one-tenth of the sample size [176]. We were unable to find published classification results for EMG signals; however, we believe that the classification accuracy we achieved of up to 98% is quite satisfactory.

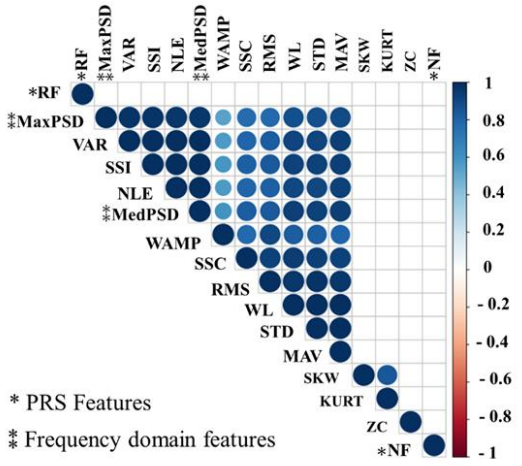

Figure 6.2.10 Correlation between individual features of the EMG signal.

The circle at the intersection of the rows of a feature and the columns of other features represents the correlation between the two features. Positive correlation has a cool tone circle and negative

correlation has a warm tone circle.

The most significant characteristic of this study is its creative use of a swarm intelligence approach to draw out a feature set with exceptionally low correlations by simulating the development of natural plant root systems. The features correlation for the EMG signals is shown in Figure 6.2.10. Surprisingly, two features based on the PRS algorithm have almost zero correlation with the other features. Conversely, the time-domain features and frequency-domain features are more or less correlated with the other features. The low correlation between the PRS features and the other features is due to the different feature extraction methods. The development of the root system is a product of group decision-making in a process that reduces the correlation of the root matrix and the nutrient matrix in a tensor. It is for this reason that the performance of the classifier improves after adding the PRS features.

Another significant advantage of the PRS algorithm is its simplicity and interpretability. Anyone who has seen the root systems of plants in nature can understand and visualize the process of root development. Although the full procedure of the proposed method might appear to be rather lengthy, the algorithm is actually rather lightweight. The construction of the nutrient matrix comprises 2/3 of the work, while the construction of the root matrix and the extraction of PRS features make up the other 1/3. If the length of the biomedical signal does not exceed 100,000 and the sample size is less than 200, the training process can be completed in no more than five minutes.

The proposed PRS algorithm actually performed better than we had first expected. However, we are soberly aware that our study is not perfect and has a number of limitations. First, the rate of accuracy improvement is rather modest for each classification model. As shown in Figures. 6.2.7, a mere 1% improvement in accuracy is not enough to offset the error bar. One possible explanation for this might be a too-small sample size, resulting in inadequate model training [179]. Second, although the overall accuracy using the PRS features tends to be higher than that of the base and classical features sets for each classifier, there are still exceptions, as can be seen in Figures. 6.2.6 – 6.2.8. These phenomena are likely to be related to the possibility that extracting features based on the PRS algorithm does not work well in the presence of outliers. Root growth is based on the values in the soil matrix, which are obtained by performing statistical calculations on the biomedical signals. Mistakes are passed down, causing a reduction in accuracy. This would explain why, in some cases, lower accuracy is obtained at high training rates.

Although PRS has had some success in the field of feature engineering, it will not be limited to this field. Learning from other existing evolutionary algorithms to enhance the generality of them is the next stage of work to be done. In future algorithm comparisons need to be performed not only from classification accuracy, but also from computing speed and rationality.

6.2.6 Conclusion of this Section

Recognizing that existing feature extraction methods are not sufficient to produce biomedical signal classifiers that meet the requirements of clinical application, this research proposes a new swarm intelligence-based algorithm for extracting features to ensure higher classification accuracy. The proposed algorithm is based on the growth of roots in nature and offers good interpretability. Importantly, the features obtained by the PRS algorithm have a very low correlation with traditional features, and the accuracy of classifiers using features extracted by the proposed algorithm is shown to improve. This study lays the groundwork for future research focused on extending the use of biomedical signals from strictly research applications to clinical applications.

Chapter7

Diagnosis of Knee Disorders based on Impact Signals

7.1 Introduction to this Chapter

Osteoarthritis (OA) represents a progressive degradation process. Usually, OA occurs in the knee joint because this joint supports almost the entire weight of a human body and provides motion during walking [54,55,212]. Due to the knee joint being important and vulnerable to injury, the pathology of cartilage, which is the key to dynamic weight-bearing of the knee joint, is of interest to many studies. They have shown a relationship between cartilage damage and the grade of OA; [12,213,214]. Consequently, a common belief is that when knee cartilage is injured by severe trauma or chronic incorrect gait, the normal balance between the damaged part biological repairing and the healthy part biological maintenance of the injured cartilage is hard to keep[215,216]. The imbalance will eventually bring about a localized loss of cartilage thickness, which further deteriorates knee OA.

The diagnosis of cartilage damage without medical equipment is exceedingly tricky, such as palpation. Also, Bacon et al. argue that cartilage thickness loss is weakly associated with knee pain [12]. This means that it is difficult for surgeons and researchers to uncover early signs of cartilage damage from symptoms such as pain. The non-invasive diagnosis of cartilage damage in modern medicine is almost exclusively by magnetic resonance (MR) imaging and ultrasound imaging (UI) [217,218]This clinical diagnostic technique, which started more than a decade ago, has tremendous advantages in terms of diagnostic accuracy. However, the high cost of maintaining equipment and operating by professional staff means diagnosing cartilage damage in the early stages is a heavy financial burden with medical imaging. Throughout all the studies, a reliable and inexpensive measurement technique has not been applied to the clinical field to cartilage damage. This new technology of cartilage diagnosis is expected by the public.

To meet this challenge, we propose a new scheme to determine cartilage damage grade based on changes in the acoustic properties of cartilage. Studies of the acoustic properties of cartilage are not uncommon but monitoring the time-frequency characteristics of regular geometry cartilage prostheses, or ultrasound images are more typical[218,219]. In this study, 3D models have been extracted from the patient's knee joint MR images. The 3D model is then output and assembled into a knee prosthesis in which the cartilages are adjusted according to Outerbridge Grading Systems (OGS) [202]. A measurable impact signal transfers from the calf to the thigh, and the attenuation before and after passing through the cartilage will indicate cartilage damage level. The cartilage can be seen as a viscoelastic material, so measuring and analyzing the vibration absorption in such a thin cartilage prosthesis is the focus of this study[220,221]

Hence, this study decided to analyze the absorbed vibration in both acceleration and jerk dimensions. The continuous Gaber transform (CGT) is used for the time-frequency analysis in the acceleration dimension because it is not prone to resolution degradation (Rene Carmona et al., 1998). On the other hand, the jerk is the differential of acceleration, contains richer information that humans can perceive, and is helpful in engineering[222,223]. Last, using time-frequency analysis of the acceleration combined with singular spectrum analysis of the jerk for cartilage damage grading [224].

The significance of this study is that the technique of grading knee cartilage damage by vibration signal attenuation on a real scale knee prosthesis. The achievements of this study give the public hope for a novel diagnostic technique for non-invasive knee OA caused by cartilage damage. In addition, the impact signal input is cheaper and has weaker power than traditional ultrasound input. Hence, this new technology which does low-cost, high-safety, and not requires a medical background, will bring a new vision to the clinical diagnosis of the knee joint.

7.2 Experiment

7.2.1 Construction of 3D Knee Joint Models by MR Images

MR images are usually in Digital Imaging and Communications in Medicine (DICOM) format, which is the standard for communicating and managing medical imaging information and related data [225]. Since DICOM is a dedicated file for surgeons in diagnostic treatment, it needs to be converted into a Standard Triangulated Language (STL) file for engineering applications. In this study, 3D models of the femur, femoral cartilage, tibia, tibial cartilage, and meniscus in the knee joint were manually extracted from the DICOM drawing by 3D Slicer [216,226]. MR images were obtained from a female patient (76 years old) with mild OA knee, and the Tokyo Metropolitan University ethics committee permission number is H30-80. After that, assemble the knee joint parts in Netfabb (Autodesk), as shown in Figure 7.2.1. In addition, ligaments were not considered due to the MR images' modeling limitations[216].

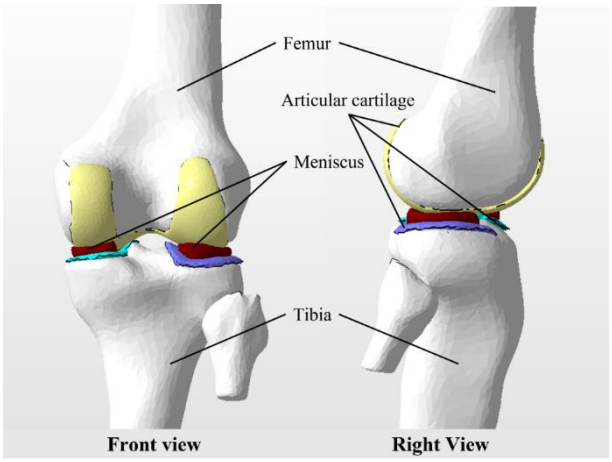

Figure 7.2.1The 3D models manually extracted from MR images of the right knee joint in STL format.

7.2.2 Making of Knee Model

The knee model consists of two parts: the hard tissue part, bones; the soft tissue part is cartilage, meniscus, and other soft tissue. An ideal model knee joint needs to be in an extended position, and the cartilage and meniscus sandwiched between the femur and tibia, surrounded by layers of different soft tissues[55]. However, a model that is closer realistically to human limb presents difficulties in assembling parts and sensors. Therefore, the knee model was simplified and made as follows.

7.2.2.1 The hard tissue part

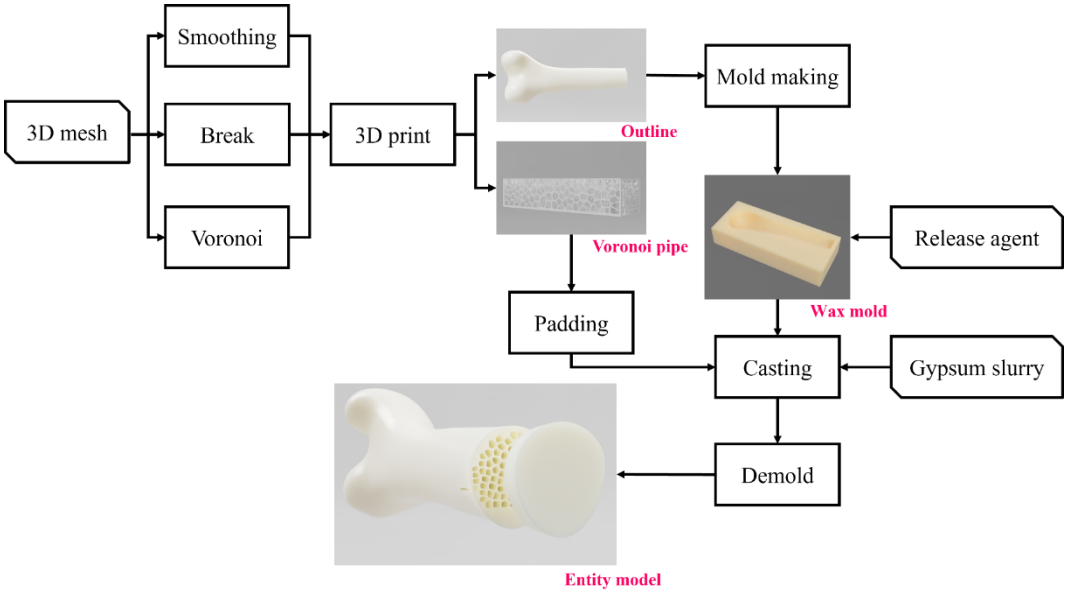

Figure 7.2.2 The process of making femoral and tibial models

The hard tissue part occupies approximately 90% of the transmission path. To make the hard tissue part more realistic, the femur and tibia models were made cautiously in this study, as shown in Figure 7.2.2. Because the vibration signal passing through femur and tibia is unnecessary and a full-sized bone results in a higher center of gravity leading to greater baseline drift, the 3D models were cut off at 25 cm from the condyle of the femur and tibia. The unsmooth areas in the meshes of the femur and tibia obtained by MR imaging, were smoothed by Netfabb and output by the 3D printer (CR-10S PRO, Creality) for mold making. In addition, the bone tissue is in a honeycomb-like matrix structure that affects the bone mineral density (BMD) and is related to knee OA [227]. In this study, the Voronoi pipe was used to construct honeycomb-like structures in the bone tissue. Then, the printer created the Voronoi pipe and padded it into the wax mold and cast it with gypsum slurry (Yoshino-gypsum). Each hard tissue phantom was demolded after drying, of which 15% volume was polylactic acid (PLA, Tinmorry) Voronoi pipe and 85% volume was gypsum.

The BMD for the tibial model is $0.613 g/cm^2$ and for the femoral model is $0.592 g/cm^2$, which is nearer to BMD of the lower limb bones of females aged 50-80 years with mild OA [227].

7.2.2.2 The soft tissue part

Human soft tissues have a viscoelastic model to absorb vibration signals and are divided into categories by location. The meniscus and articular cartilage are summed up as one category and other soft tissues such as muscle and fat are summed up as the other category. The absorbed vibration of the former needs to be measured and analyzed in this study, which is referred to as the target object (TO). The latter's absorbed vibration hinders this study, which is referred to as a futility object (FO).

The TO models were divided from top to bottom into femoral cartilage, meniscus, and tibial cartilage. Although the meniscus is sandwiched between the femoral and tibial cartilages, the cartilage-cartilage contact areas are expanded with meniscus movement. In addition, all of the cartilage-cartilage contact areas are widely perceived to risk becoming damaged in clinical diagnosis. In this study, the medial femoral cartilage was chosen for observation because cartilage-cartilage contact is more complex[228].

The medial femoral cartilage phantom is needed for deriving different pathological symptoms based on OGS in the original model's subsequent processing while being made as realistic as possible. In OGS, the process of cartilage damage is first softening and swelling, then fissuring, and finally exposing the subchondral bone[218].

Knee articular cartilage consists of collagen, proteoglycan, and water. It has a unique biomechanical model that can withstand a greater than bodyweight load without being broken [229,230]. In this study, thermoplastic polyurethane (TPU, Pxmalion), an elastic material with good compression and tensile resistance, was used to create a healthy cartilage phantom in this study. The Young's modulus of the TPU material is 2-5 MPa at room temperature, and that of human cartilage is 1.52 MPa[231,232]. In this study, starting from grade 1, gelatin material in the damaged area replaced the healthy area on the medial femoral cartilage phantom. The damaged area is a projection on the cartilage of an ellipse with a semi-long axis of 10 mm and a semi-short axis of 5 mm. The replacement was designed on a 3D mesh but operated on the model. The composition of gelatin (Morinaga) is animal collagen, similar to human cartilage, but not as tough. The femoral cartilage phantom, as shown in Figure 7.2.3, the Shore hardness of the model in the healthy area (white) is 39.8 and in the diseased area (pink) is 12.4.

The meniscus is the core component of knee joint movement and carries more stress than the cartilage during walking. However, the meniscus and cartilage material composition is almost same [15]. Therefore, the tibial cartilage and meniscal model were made of the same material, thermoplastic polyurethane. As the experiments are planned to be performed under static posture with knee joint extension, the meniscal translocation can be ignored. However, as knee MR images are taken in the unloaded state, the meniscus deformation cannot be ignored[216].

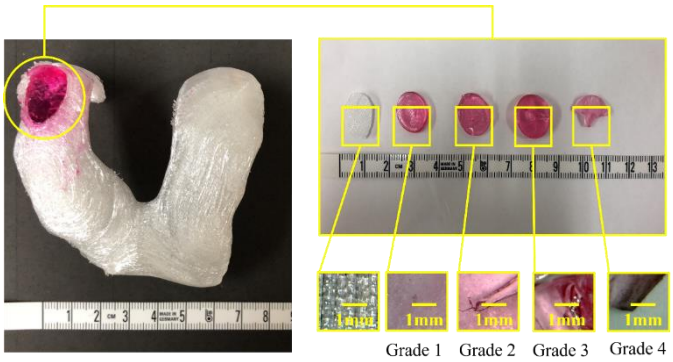

Figure 7.2.3 The cartilage phantom

To ensure the deformability of the meniscus is preserved while meniscus translocation is limited, a good strategy is to fix the meniscus and tibial cartilage together for a 3D printout. We combined the meniscus and tibial cartilage into one mesh based on the relative positions in the unloaded state. Subsequently, the printed tibial cartilage and meniscus phantom were separated partially along the contact surface of the meniscus and tibial cartilage with a heat knife (HS, Huanyu), leaving only one circle on the geometric center of the meniscus for fixation, as shown in Figure 7.2.4.

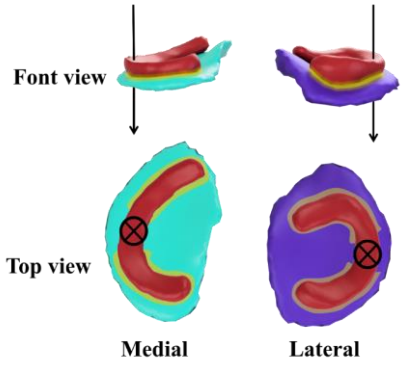

Figure 7.2.4 The lateral and medial meniscus are fixed to the lateral and medial tibial cartilage.

The fat and muscle belonging to other soft tissues tightly wrap around the knee joint and support the body. While fat-muscle tissues can protect the knee, a thick layer of fat overloads the knee, causing damage to the cartilage and meniscus [108,233]. The fat-muscle tissues can be considered as a membrane stretched tightly over the cylindrical frame of the knee. The membrane impacting causes a surface vibration, which is called a two-dimensional wave. However, fat-muscle tissues are a typical viscoelastic body with thickness, and only extremely weak vibrations are caused by equilibrium perturbation. Since viscoelasticity attenuates the two-dimensional mechanical and vibration waves, covering the entire knee model with a fat-muscle tissue phantom is unwieldy[234]. Therefore, the fat-muscle tissue phantoms as FO are retained only at the input and output points of the impact signal. Polyurethane gel (PU-gel, Proseven) is a skin-like material used as a fat-muscle tissue model. The thickness of the tissue models was different because the hit point was at the calf, and the measurement point was at the thigh. We used the muscle fat thickness of adult females as a baseline and cut the

thickness down slightly to better match the fat-muscle tissue phantom of Asian females [235,236]. The thickness of the fat muscle tissue model was set at 10 mm and 4 mm on the thigh and calf, respectively.

7.2.3 Assembly of Knee Model and Sensors

7.2.3.1 Assembly of knee model

The knee model was assembled in a standing position, as shown in Figure 7.2.5. First, two 6 mm diameter holes were opened 10 mm below the femoral model cut-off surface in the sagittal and coronal planes. Two beams of the same diameter and length were then passed through the holes mentioned above. Two rubber bands with diameters of 3 mm connected the femoral model to the stands through the beam, and the femoral condyles were vertical to the ground due to gravity. In addition, the compressive stress between the femur and tibia can be changed by varying the number of hanging weights.

The standing position tibial model was inserted into a silicone-gel-filled box and placed directly below the femoral model after curing the silicone gel, which same as the tibia is fixed by the foot and ankle joint in standing position. After that, the fat-muscle tissue phantoms were secured with rubber bands to the femur and tibia models, respectively, at 15 cm from the knee joint contact surface. In addition, the boxes and stands were made heavy to ensure their stability.

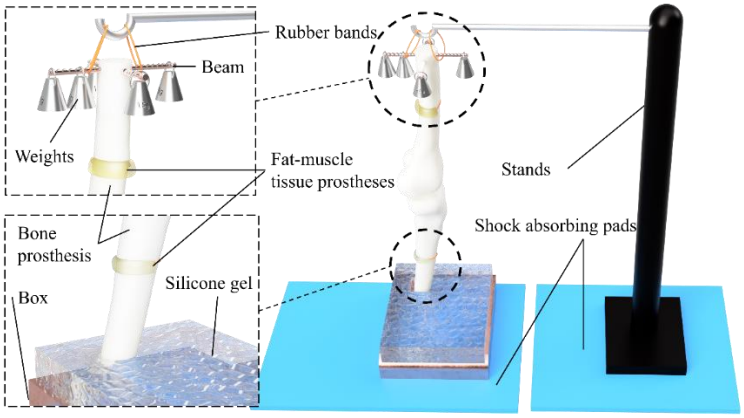

Figure 7.2.5 Assembly of knee joint model

The cartilage phantom and bone model were attached using self-tapping screws, as shown in Figure. 7.2.6. In this case, the femoral cartilage was fixed with three screws, and the medial tibial cartilage and lateral tibial cartilage were fixed using only one screw. Finally, when no weights are hanging from the beams, the stand is adjusted to a height using a film-type force sensor (FSR400, INTERLINK) where the femoral cartilage (damage area) is in contact with the meniscus, but the stress is close to

$0 g / mm^2$.

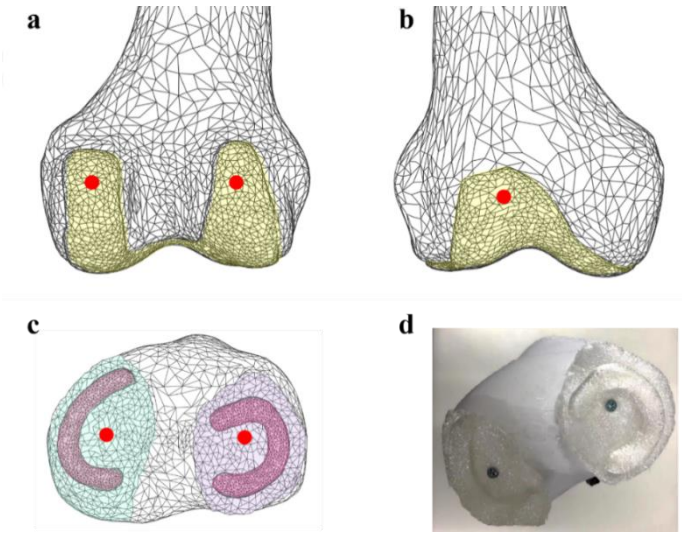

Figure 7.2.6 In a, b, c, the red points are the connection points, and d is a photo of the cartilage phantom and the bone model in a fix.

7.2.3.2 Put on sensors to the knee model

In this study, the primarily used sensors were acceleration and force sensors. Among them, the aforementioned force sensors are mainly used to measure the stress caused by the load, while acceleration sensors are used to obtain vibration signals, which are the core signals. The sensor was placed on the knee model, as shown in Figure 7.2.7.

The two force sensors (A2 and B2) are film-type force sensors clamped by the femoral cartilage and meniscus, which are used to measure the medial and lateral stresses. The stress signals were collected by an analog-to-digital converter (ADC2) (4224, Picoscope) and stored on a computer.

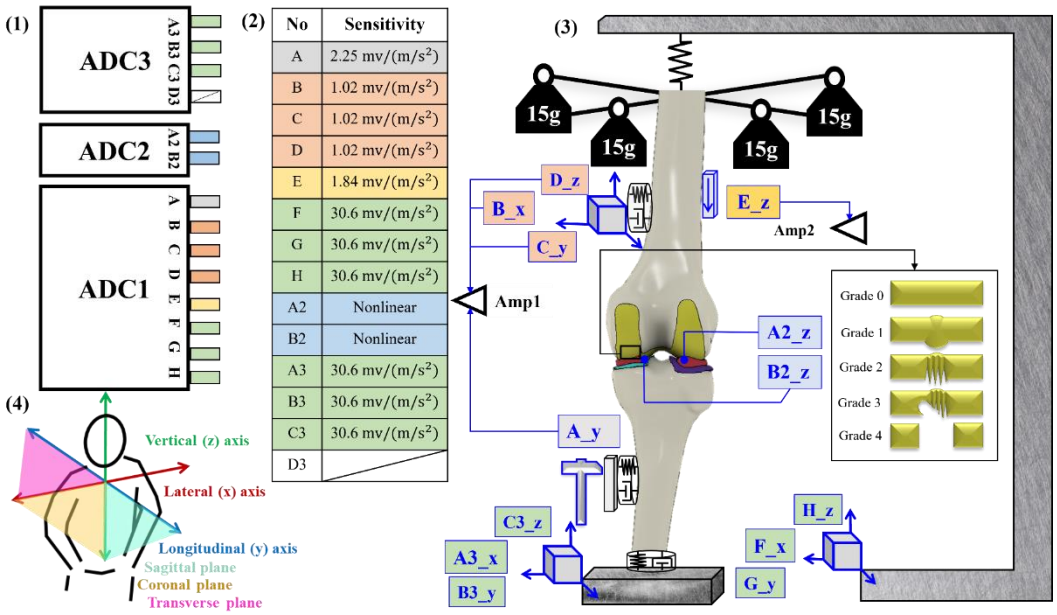

Figure 7.2.7 The diagram of sensors attached to the knee joint model.

Conversely, four types of acceleration sensors are applied in this study. The impact hammer (086C03, PCB) is a hammer (A) with a built-in acceleration sensor that generates an impact signal by hitting an aluminum plate (20 mm×35 mm×5 mm) attached to the surface of the fat-muscle tissue phantom in tibial models. The impact hammer has an interchangeable impact chip in the head that can be hit to produce different frequency impact signals. In this study, an aluminum impact chip was used to obtain a higher-frequency input signal. Three accelerometers (353B16, PCB) belonging to the second type, that are connected to an adapter and fixed to the surface of fat-muscle tissue phantoms at the femoral model monitor output signals. The three acceleration sensors (B, C, and D) are perpendicular to each other in the spatial coordinate system, and one of them is parallel to gravity. To reduce circuit interference, four-channel signal conditioning (482C05, PCB) was used to filter and amplify the input and output signals, which were then stored by the ADC1 (4824, Picoscope) to the computer.

The remaining two types of accelerometers were prepared to collect reference signals. The first reference signal comes from the acceleration sensor (BW21SG2, FUJICERA) attached to the femoral model next to fat-muscle tissue phantoms. The sensor (E) is fixed to the femoral model by a double-sided adhesive in a direction parallel to gravity and compares the attenuation of the signal through the fat-muscle tissue phantom. The electrical charge is converted into voltage signals by the charge amplifier (CA201, FUJICERA) and then saved to the computer by ADC1 (4824, Picoscope).

The last type includes two triaxial acceleration sensors (KXR94-2050, Kionix) built-in amplifiers. These two sensors are fixed by a double-sided adhesive to the stand that hung the femoral model (F, G, H) and the box (A3, B3, C3) that holds the tibial model, respectively. They are used to detect the baseline drift from the hitting by a hammer and then saved to the computer by ADC1 and ADC3 (6254BD, Hantek).

In addition to the sensors, the weights were hung on the beams inserted into the femoral model. We mentioned earlier the no-load option, in which the stress between the meniscus and femoral cartilage is zero. On the flip side, the load option uses sixteen 15 g weights evenly hung on each beam branch. At this time, the cartilage and meniscus are deformed by compressive stress and the contact surface becomes larger. The reason for choosing 240 g as the load is the prosthetic material of healthy cartilage; diseased cartilage and meniscus are softer than the real one.

7.3 Signal Acquisition and Signal Processing

The impact hammer hits an aluminum plate located in the tibial model, producing impact signals. The impact signals are picked up by accelerometers located at different positions of the knee model and converted to digital signals at a sampling rate of 20 kHz and a vertical resolution of 12 bits. However, the vertical resolution of the accelerometer leaving the knee model is only 8 bits, and a trigger control multiple channels.

7.3.1 Signal Acquisition

When the experiment started, we first measured the stress of the femoral model with different Outerbridge grades under a 240 g load by the film-type force sensors. Because the knee joint model under load leads to displacement, which in turn brings about an imbalance of stresses in the medial and lateral zones, resulting in errors. Then, the medial and lateral stresses are balanced by adjusting the position of the weights on the beam. Calibration of the static baseline is required after all sensors are connected in a state of equilibrium stress.

Subsequently, the force sensors were removed, and the same experimenter used the impact hammer to hit the aluminum plate ten times with the same strength on different OGS grades of the femoral cartilage phantom. The experiment with no load was the same as above, except that the stress measurement step was skipped.

Although the experiment in this study is similar to the modal analysis experiment, it is not the same. The differences are not only due to differences in equipment and methods, but also in human damage. Considering the cartilage as a viscoelastic object, which makes it difficult to observe the frequency response, it is a challenge to arrange enough acceleration sensors in such a narrow area of the knee, and to input a sufficiently strong impact signal to allow observation of the frequency response.

7.3.2 Signal Processing

An ideal impact signal can be obtained when the hammer contacts the aluminum plate with an infinitely small duration, which can cause a constant amplitude in the frequency domain. Moreover, as an input signal, the impact signal is damped by a different part of the knee model during the transmission process. However, all parts were unchanged except for the femoral cartilage phantom in the whole knee model, and the femoral cartilage phantom was changed by OGS grade. Therefore, digital signal processing between the output and input signals makes it possible to obtain vibration signals absorbed by the cartilage with different OGS values. The signal processing process is illustrated in Figure 7.3.1.

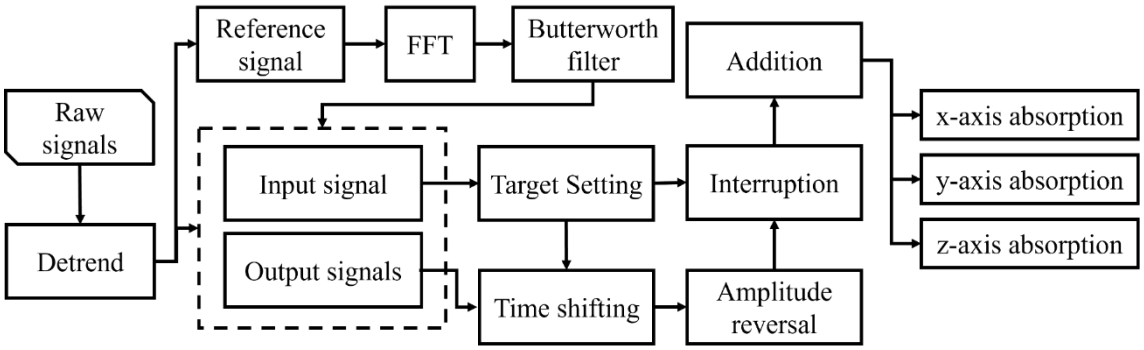

Figure 7.3.1 The filtered input signal and the output signal are processed in the time domain, with

the input signal in 1D space and the output signal in 3D space.

The signal processing can be described as follows: First, the linear trends in the raw signals are removed by the least-squares method [237]. Because the mass of the knee model is much smaller than the weight of a real person, hammering can cause interference from shaking. Subsequently, a fast Fourier transform combined with a Butterworth filter is required to remove the shaking in the frequency domain. These shakes were measured as reference signals by acceleration sensors attached to the stand and the box, and spectral energy was focused at 2-4 Hz. Because the real signal needs to be preserved as much as possible, a 6th order band-stop filter is applied to the input and output signals. Subsequently, to correct the delay, the maximum amplitude of the input signal was used as the target, and the output signals were shifted to the target in the time domain. Finally, to obtain the differences, the amplitude of the output signals is reversed and interrupted to the same length as the input signal. Then, the output signals are added to the input signal to obtain three vibration signals absorbed in a three-dimensional space.

The signal processing in this study does not involve high-frequency noise reduction because the knee model is primarily static. There is only one band-stop filter that removes the baseline drift caused by the hammering.

7.3.3 Signal Analysis

7.3.3.1 Time and frequency analysis of absorbed vibration signal

In signal analysis, time–frequency analysis is a body of techniques and methods used for characterizing and transient signals whose statistics vary over time. For normal time-frequency analysis, wavelet transform (WT) and Hilbert-Huang transform (HHT) are common choices for ensuring better time-domain resolution and frequency domain resolution of transient signals [55,238]. However, the calculated quantity was not friendly. In particular, a large number of samples, owing to the high sampling rate, require a large amount of computing time. To solve this problem, we extend to the continuous Gaber transform (CGT), based on the previously used short-time Fourier transform (STFT), to achieve the same time-frequency resolution with fewer calculations[54,239]. The Gabor transform of a signal x(t) is defined by the following equation:

$$G_x(t, f) = \int_{-\infty}^{\infty} e^{-\pi(\tau-t)^2} e^{-i2\pi f\left(\tau-\frac{t}{2}\right)} x(\tau) d\tau \qquad \text{Equation 7.3.1}$$

where the Gaussian function $e^{-\pi(\tau-t)^2}$ is regarded as a window function. Because its infinite range lacks practicality, its significance level distribution is often chosen as the new range. The equation can be simplified as:

$$G_x(t,f) \simeq \sqrt[4]{\sigma}\int_{t-\frac{1.9143}{\sqrt{\sigma}}}^{t+\frac{1.9143}{\sqrt{\sigma}}} e^{-\sigma\pi(\tau-t)^2} e^{-i2\pi f\left(\tau-\frac{t}{2}\right)} x(\tau)\,d\tau \qquad \text{Equation 7.3.2}$$

where σ is used to control the window width to hundred.

Because the CGS-based time-frequency analysis has good resolution in both the time and frequency domains, this study decided to use the distribution of the spectrum energy in the low-frequency zone as a characterization. That is, the duration of the component is more than 50% of the maximum spectral energy and below 2kHz.

7.3.3.2 Singular spectrum analysis of the absorbed jerk signal

The jerk is the rate at which the acceleration changes with respect to time, and it can be defined in differential terms as a vector.

$$\vec{j} = \frac{d\vec{a}}{dt} = \frac{d^2\vec{v}}{dt^2} = \frac{d^3\vec{s}}{dt^3} \qquad \text{Equation 7.3.3}$$

Where, $\vec{a}, \vec{v}, \vec{s}$ are acceleration, velocity, displacement, respectively.

The jerk as a differential of acceleration is considered to have richer information, and the study also decided to analyze the absorption of the jerk signal by the knee model. Because jerk sensors are not commercially available as a standard product, we decided to use acceleration to calculate the jerk using the discrete derivative method with a gain value.

$$y(t_n) = K\left(\frac{x(t_n) - x(t_{n-1})}{T_s}\right) \qquad \text{Equation 7.3.4}$$

where K is the gain value and T_s is a fixed discrete step size, both of which are set to one. However, because the differentiation is too sensitive to noise, an 11 order Savitzky–Golay (SG) filter is used before differentiation.

Although jerk has applications in aeronautical engineering and earthquake science, it is less analyzed by time-frequency analysis because of the lack of physical definition in classical mechanics [222,240]. Therefore, this study analyzes the jerk signal with a singular spectrum to supplement the high-dimensional information not available in CGT analysis.

Singular spectrum analysis (SSA) is a practical technique for time-series analysis and forecasting. It is amazing as a principal component analysis (PCA) for extracting information from time series. Slightly different from PCA, it performs better on short and nonstationary signals that contain more noise [241,242]. In this step, the SSA is used to extract the oscillation component of the jerk signal for the power around the highest oscillation point evaluation.

The basic SSA can be simply described as follows[242]. The obtained jerk signal $Y_N = (y_1, \ldots, y_N)$ can

be constructed as L-lagged vectors $Y_i = \left(y_i, \ldots, y_{i+L-1}\right)^{\mathrm{T}}, i = 1, 2, \ldots, K$ through a window of length L, where $K = N - L + 1$. Subsequently, these vectors can make up a trajectory matrix $\mathbb{Y}$. Subsequently, the eigenanalysis of matrix $\mathbb{Y}\mathbb{Y}^{\mathrm{T}}$ (equivalently, the singular value decomposition of the matrix $\mathbb{Y}$) yields a collection of L eigenvalues and eigenvectors. A combination of these eigenvectors determines an r-dimensional subspace $\mathbb{L}^{r}$ in $\mathbb{R}^{L}, r < L$. The L-dimensional data $\{\mathrm{Y}_1, \ldots, \mathrm{Y}_k\}$ were then projected onto the subspace $\mathbb{L}^{r}$. Some Hankel matrices $\mathbb{Y}^{*}$ are restructured by averaging over the diagonals, which approximates to $\mathbb{Y}$. Finally, the time series $Y_N^{*}\left(y^{*}, \ldots, y_N^{*}\right)$, which has a one-to-one correspondence with the matrix Y^{*}, provides an approximation of either the whole series Y_N or a particular component of Y_N.

Although there are four steps in the SSA algorithm, embedding, decomposition, grouping, and reconstruction, only two parameters, window length L and grouping index r, are involved. To extract the oscillation component better, we chose 50 as the window length and 1–3 as the grouping index because of the weaker weight correlation. Because the oscillation component of the jerk signal remains transient, the sum of squares of 50 steps before and after its highest oscillation point is used as the evaluation of power in this study, and the details are as follows.

$$m = \arg\max_{t_n} \left\{ g\left(t_n\right) \right\} \qquad \text{Equation 7.3.5}$$

$$p = \begin{cases} \sum_{j=1}^{100} \left[g(j)^2 \right]; m \le 50 \\ \sum_{j=m-50}^{m+50} \left[g(j)^2 \right]; m > 50 \end{cases} \qquad \text{Equation 7.3.6}$$

where $g(\mathrm{t}_n)$ is the oscillation component drawn from the jerk signal $\mathrm{y}(\mathrm{t}_n)$ by the SSA. where p refers to the energy of the oscillation component. In this study, the arithmetic sum of the powers of the oscillation components in the three axes was used as an OGS grade feature.

7.3.3.3 Statistical analysis

Statistical analysis was performed for data analysis in this study. Owing to the small sample size in this study, we chose to use nonparametric statistics after the Shapiro-Wilk test found that it did not follow a regular distribution. The Friedman test was used for multiple comparisons in this study, and a confidence interval of 95% was set. In addition, the healthy group was set as the control group, and the other grades were designated as the test group for the Steel-Dwass test, again with 95% confidence intervals.

7.4 The result and discussion

One set of acceleration signals is absorbed by the knee joint model, as shown in Fig. 7.4.1.

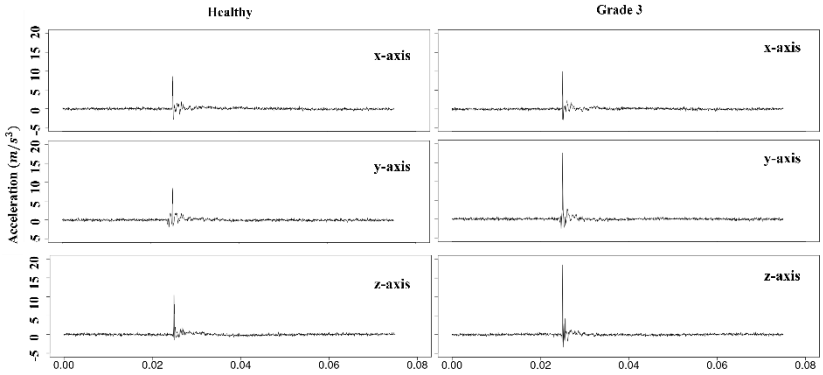

Figure 7.4.1 the absorbed acceleration signal in three directions by a knee joint model with grade 3 cartilage

Apart from a slight difference in the amplitude strength, there is no significant difference in the vibration signal being absorbed in healthy cartilage and in the cartilage of grade 3, such as trend and sparseness. Therefore, some statistical features were computed to replace visual observation. The most commonly used features of biosignal are zero-crossing, kurtosis, and skewness, which have been successfully used in the feature extraction process with high efficiency. In the present study, the rate of directional change of the signal varies with the cartilage phantom by zero-crossing, and the slope of the signal also varied with the cartilage phantom, as determined by kurtosis and skewness. Although the statistical signal analysis results are insufficient to distinguish between cartilage damage grades, they provide some direction for moving forward.

After the CGT-based time-frequency analysis of the acceleration signals, the energy spectra were obtained. A typical energy spectrum is presented in Figure 7.4.2. The energy spectrum was observed, and it showed the duration of the high-energy components is different in the low-frequency area. The area of a polygon constructed from the duration and frequency of the high-energy components seems to be a good classification feature.

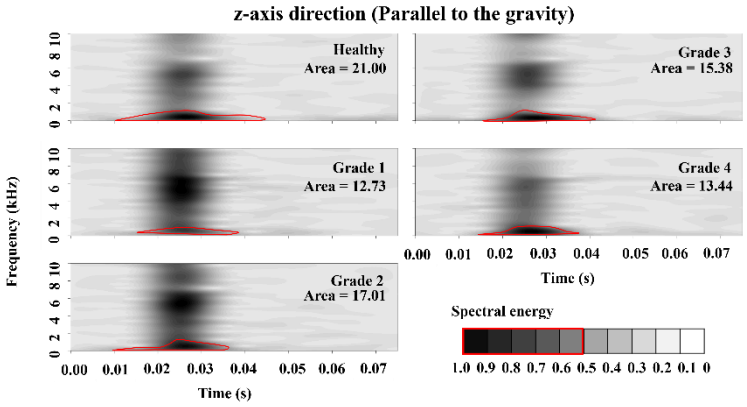

Figure 7.4.2 A typical CGT time-frequency energy spectrum of an acceleration signal in the z-axis direction.

The analysis of the energy spectrum area for all samples was statistically calculated and is shown in Figure 7.4.3. In the low-frequency region of the x-axis, the high-energy area decreased and then increased with the deterioration of cartilage damage. On the y-axis, the high-energy area of healthy cartilage was greater than that of the damaged cartilage, which was statistically significant except for grade 2. In the z-axis, the high-energy area of healthy cartilage was greater than that of grade 1 cartilage and was statistically significant. However, multiple comparisons performed on all samples in each axis showed no statistical significance.

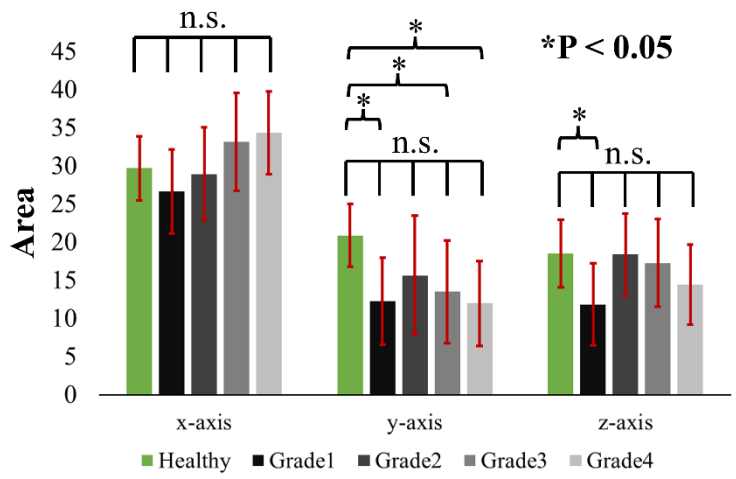

Figure 7.4.3 The mean of the area of the high-energy spectrum in the low-frequency area at 3 directions for all signal samples.

This result does not follow the expectations of this study because we can see in Fig. 7.4.3 that the shapes of the dark enclosed areas can be used as a classification. However, the enclosed areas were inadequate for classification. One speculation is that perhaps the flat space of the energy spectrum consisting of time and frequency is restricted by Heisenberg's uncertainty principle of signal analysis. It is possible to start with a complexity aspect that may have enormous progress in the future. In

addition, the instantaneous frequency also seems to have the potential to be used as a feature and deserves further investigation.

Then, a set of jerk signals were computed to show in Fig. 7.4.4.

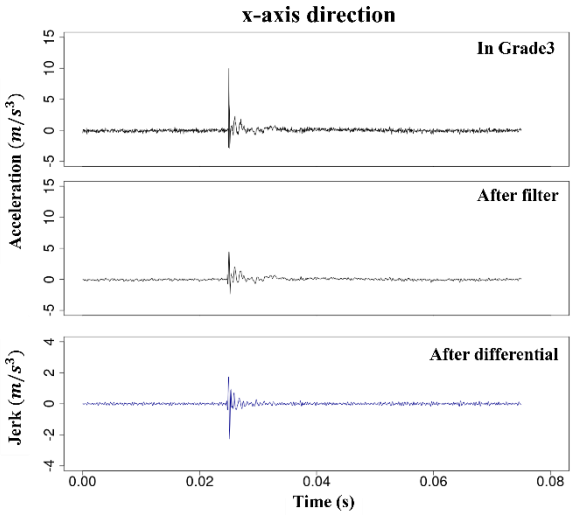

Figure 7.4.4 The signal in the position is the acceleration signal in the x-axis direction on the knee joint model with grade 3 cartilage.

In Figure 7.4.4, the raw acceleration signal contains high-frequency noise. If the acceleration signal without noise reduction is differentiated into a jerk signal, the high-frequency noise component will remain in the newly generated jerk signal and cause interference. Therefore, the jerk signal obtained after SG filtering can be used for the subsequent SSA analysis. The reason for not choosing the time-frequency analysis here is not only that the previous CGS analysis did not achieve the expected results, but also because of the inadequate physical definition of the jerk signal. After SSA analysis, the original jerk signal can be decomposed into trend, oscillation, and noise components. Because the jerk signal is instantaneous, the trend component is meaningless and the noise component hinders the signal analysis, we only choose the oscillation component as the object of analysis. The oscillation components in the x-axis direction for a typical set of jerk signals are shown in Figure. 7.4.5.

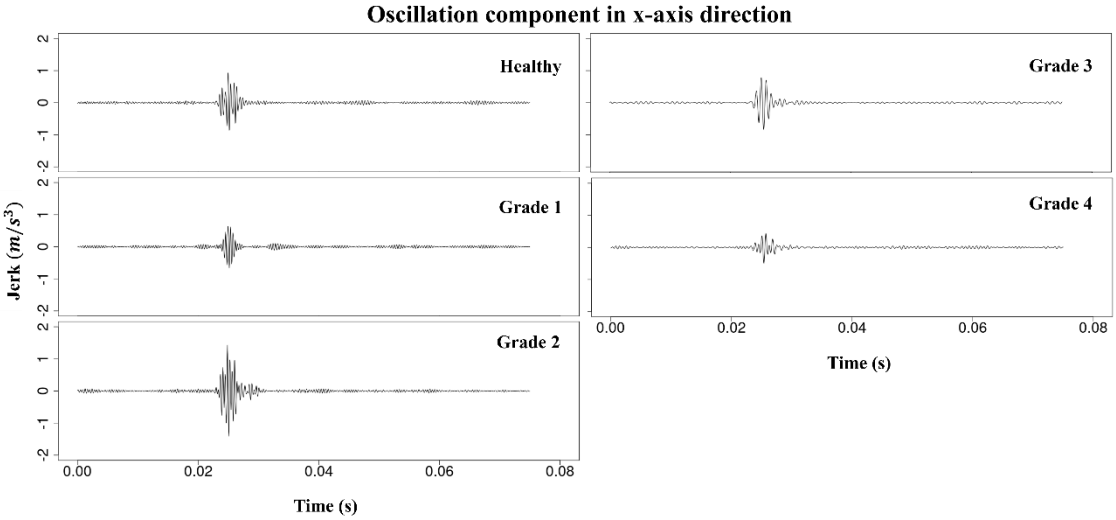

Figure 7.4.5 A typical set of oscillation components of the jerk signal in the x-axis direction.

It was observed that the oscillation component was perfectly extracted for each OGS grade. However, some noise components, almost negligible, are interspersed in the sub-signal. The sub-signals containing only oscillation components in the x -,y -, and z-axes were extracted by SSA. The power sums were calculated as described in a previous method. Statistical analysis was performed, as shown in Figure 7.4.6.

These results were as expected. The classification ability of the proposed jerk signal oscillation component based in this study for different OGS-grade knee models is significant. The observation can see that the power of the oscillation component decreases with the deterioration of the damaged cartilage from grade 1 to grade 4. Although the variability between grade 1 and healthy subjects was not significant, there was a statistically significant difference with the other grades. Moreover, multiple comparisons performed on all samples showed statistical significance.

This study is an attempt to diagnose knee cartilage loss using impact signals based on a real-scale knee joint model with different OGS-grade cartilage phantoms. Despite the results achieved in this study, there are limitations in the fabrication of the knee joint model and signal analysis. The first is the realism of the knee joint model. Owing to the material cost and machining difficulty, we simplified the knee-joint model, which can affect future experiments on real knees not achieving expected goals. Second, the data samples for signal processing were limited to ten because damaged cartilage made with gelatin materials changed in properties with the loss of moisture.

In addition, this study focuses on amplitude attenuation and does not extend to modal analysis. Because not only motion structures are far less likely to cause injury due to resonant frequencies than brain and visceral structures, but also difficult to input an impact signal safety and large enough to observe the frequency response.

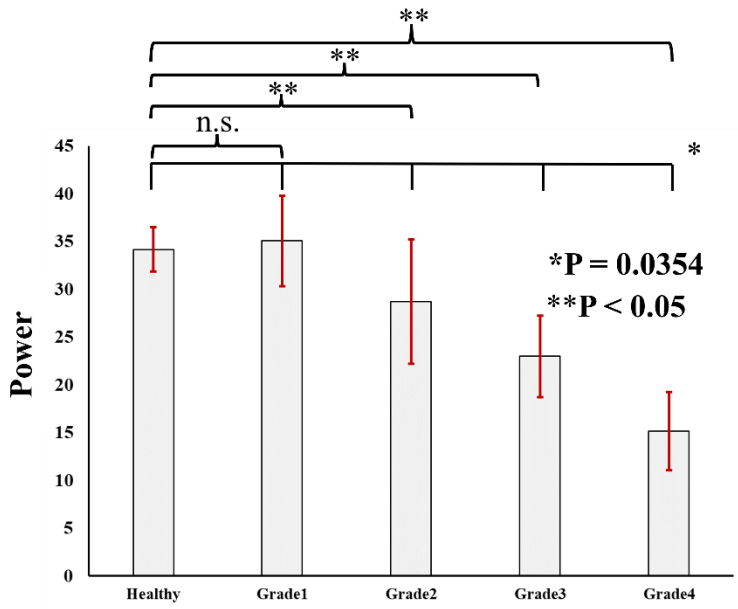

Figure 7.4.6 The mean value of the power around the highest oscillation point of the jerk signal for different OGS grades cartilage phantom.

Finally, it is important to discuss how to extend this experiment from the knee model to a real knee joint. First, the participants were required to lie flat on the test bench and a constant force from the foot with a vertical force to ensure contact between the cartilage, because the results obtained without load in this study were poor. Finally, MR images are required to verify the results of the experiment on a real knee.

7.5 Conclusion of this Chapter

The considerable pain caused by knee OA in patients led us to focus on non-invasive diagnostic techniques for knee cartilage damage. Subsequently, a hypothesis is proposed for determining the OGS grade of cartilage damage by impact signals and experimented on a hand-made knee model for verification. Furthermore, the CGT-based time-frequency analysis and SSA-based analysis of the jerk signal could find some features that could be characterized as different OGS grades of cartilage damage. These features give confidence to the present study in transferring this hypothesis to a real knee cartilage diagnosis. The proposed method and results of this study certainly offer hope for new non-invasive knee cartilage diagnostic techniques.

Chapter8

Conclusion

"If you want to find the secrets of the universe, think in terms of energy, frequency and vibration."

Nikola Tesla

8.1 Review of this dissertation

The hypotheses and goals given in the Chapter 1 of this dissertation and answered in the remaining chapters. Although the answers not perfect, lay the foundation and indicate the direction for future research related to VAG signals. Let us first review what problems have been tackled in this dissertation.

The first problem is the VAG signal collection. It's definitely not easy to collect VAG signals in an efficient, stable, low-interference, safe and easy-to-operate way. To address this thorny problem, I had developed a VAG signal collection system based on a piezoelectric ceramic diaphragm that can be easily used by people with non-medical backgrounds[72]. I put this solution in the first position because I know that only when there are many enough devices and widespread enough can the progress of VAG signal analysis technology be continuously advanced.

The second case is the VAG signal in clinical applications. To give a solution, the VAG signal was really applied in clinical experiments. The first example is the use of VAG signals obtained from accelerometers to classify the OA grade of patients who have been diagnosed with knee OA[55]. In the second case, the VAG signal was further attempted to classify the age of the knee, as the symptoms of an early OA knee were consistent with the symptoms of an aging knee. The results continue to be favorable, and the VAG signal is seen to have the potential to be applied to a large number of patients who are not effectively diagnosed early knee OA and thus have to opt for surgery[54]. I have demonstrated through the above two cases, which have been experimentally verified, that VAG signals can be used to systematically diagnose knee disorders.

To further improve the accuracy of VAG signals in clinical diagnosis, I decided to start with VAG signal processing. In fact, the pre-processing and processing of the VAG signal includes many small items such as correction of baseline drift, cropping and noise reduction. In which the most challenging is the noise reduction problem, if I can solve the VAG signal noise reduction problem can be said to be 50% success. There is a lot of noise mixed into the VAG signal, mainly uncorrelated and high frequency noise. Although it can be dealt with by conventional cutoff frequency filters, it will lead to the loss of details of the real signal. Therefore, I propose the use of ACO-EEMD, using hybrid

techniques and optimizing techniques to soften the noise. The proposed filter improves the SNR of VAG signals in normal and abnormal knees, which is useful for the application of classification of knee disorders[243].

In addition to improving the diagnostic accuracy of VAG signals in the signal processing phase, it is also possible in the feature engineering and classification model building phase. The VAG signal, as a time series, is amenable to a generalized classification model, and all that needs to be noted is that it needs to be selected based on the extracted features. Therefore, feature engineering is more important than models for classification. Since current classification models for machine learning are of Bayesian type, individual events need to be independent, i.e., independence of the extracted features. Thus, the feature of plant root system (PRS) based on swarm intelligence was proposed. This PRS feature is less correlated with other statistical or higher order statistical based features and can be used as an auxiliary feature to reduce the error and bias in the classification model and improve the diagnostic accuracy[146].

Considering that the VAG signal is a low amplitude signal, I tried to propose a hypothesis using an external source of vibration as a diagnostic method for knee disorders. The classical KL grading of knee OA is based on the gap size between the femur and tibia, then the thickness change of the cartilage is an important depending early grade of knee OA. Thus, the hypothesis is that the attenuation of an impact signal before and after passing through the knee determines the thickness of the cartilage. Thus, the hypothesis is that the attenuation of an impact signal before and after passing through the knee cartilage determines the thickness of the cartilage [244].

8.2 Summary of this dissertation

Although this dissertation had made many contributions to the research and development of VAG signal-related techniques, these solutions still have notable limitations and challenges. This section reviews these limitations of solutions and gives Suggestions

In VAG signal collection devices, piezoelectric ceramic diaphragms were used. Although it is very thin, it still does not fit the soft tissues of the body completely. Therefore, a soft piezoelectric sensor is recommended for collecting VAG signals. In addition, the device has only two channels of 12bit, and the sampling rate is capped at 2000Hz, and higher performance chips should be considered for future device improvements. The interface of this device only collects signals and stores data. An ideal system should have both collection and analysis functions.

Although good diagnostic accuracy of knee OA and aging knee was obtained in the clinical application experiment of VAG signal, it is still not sufficient for medical field application for surgeons. VAG signals, as biomedical signals, are good at pre-diagnosis and long-term monitoring, such as heart rate and blood pressure. Therefore, the future research direction of VAG signal must be miniaturization, wireless and wearable. The place where VAG signals will shine in the future should be in medical

checkup centers and community hospitals to predict damage and aging of joints, so that some painless joint diseases can receive precise diagnosis at an early stage.

Processing and analysis of VAG digital signals, including pre-processing, feature engineering, and model building. Although several algorithms are proposed in this study to enhance the diagnostic accuracy of VAG signals through digital signal processing techniques, the solutions carry a heavy computational burden while obtaining a part of reliable results. With the increasing length and size of data today, the speed of digital processing determines the range of applications for biomedical signals. In the future development of algorithms regarding VAG signal processing, there is a need to focus on the computational burden, as not all health centers can be equipped with a supercomputer.

Finally, I would like to discuss this hypothesis about the use of impact signals to diagnose cartilage loss. A typical device for diagnosis using an external vibration source is the ultrasound image, which uses the reflection of high-frequency sound in different soft tissues to image. In the present hypothesis, it is the attenuation of the instantaneous vibration signal that is the object of study. This method, although successful in solid model knees, cannot yet be tried on real knees due to safety problems. The best object to this hypothesis is the phenomenon of concussion.

8.3 Future-work to this dissertation

All the work in this dissertation can be said to set a foundation and framework for biomedical signals represented by VAG signals, and many details need to be added in the future.

1. Design of sensors and electronic circuits

A medical device that can be used in clinical applications must have reliable sensors and electronic circuits. Therefore, the next phase aims to develop the device as one that can be truly applied in the clinical field. A jerk sensor and accompanying circuitry are considered as future sensors for the VAG signal.

2. Development of interpolation algorithm

Almost all time series signals encounter occasions of missing values or outliers. When these gap values are not many and the signal cannot be re-collected, the interpolation method is seems particularly important. The next phase aims to interpolate the signal based on the causality before and after the gaps in the signal, combined the approximation theory.

3. Finding new applications

In this dissertation, all applications of VAG signals are designed for the knee joint. Although it is indeed that knee joint disease is the most vulnerable to failure of all joints, it is also important to look for possible applications of VAG signals on other fields from advancing the technology.

4. Others

There are still many points for improvement when using VAG devices to collect and analyze VAG signals. For example, the choice of sensor attachment position and the choice of target disease. These

improvements cannot be accomplished by one person or one research team, but require the support and help of the entire medical and engineering communities.

8.4 Conclusion of this dissertation

This dissertation was initially motivated by my extended interest in biomedical signaling study. In my survey of the literature, I found that so many patients with knee disorders are incapacitated because they are not diagnosed in a timely manner or cannot afford the prohibitive cost of medical imaging. VAG signals have the potential to save them.

In this study, the vibrations and sounds produced by the joints in question are both traditional and advanced. Traditional in that doctors have been diagnosing patients through these phenomena for centuries; advanced in that we can use sensors and computers to estimate the disease behind the sounds and vibrations.

Furthermore, the medical device creation, the experimental design of VAG signal collection, and the new algorithm development improved the accuracy of normal knee and abnormal knee to 90%. This study constructs a complex system of VAG signal from time series analysis to clinical application, which makes VAG signal really an important part of non-invasive diagnosis of knee joint. Although the VAG signal has shown a slight improvement in application ability under this study, it is still slightly naive compared to medical image based diagnostic techniques. This dissertation has written hundreds of pages of research on VAG signals, but the contribution is less than one thousandth of its real properties, and the potential of VAG signals is still waiting to be exploited in future.

Bibliography

[1] WHO, WHOQOL: Measuring Quality of Life, (n.d.). https://www.who.int/tools/whoqol (accessed September 30, 2021).

[2] A.A. Kiadaliri, C.J. Lamm, M.G. de Verdier, G. Engström, A. Turkiewicz, L.S. Lohmander, M. Englund, Association of knee pain and different definitions of knee osteoarthritis with health-related quality of life: A population-based cohort study in southern Sweden, Health and Quality of Life Outcomes. 14 (2016) 1–7. https://doi.org/10.1186/s12955-016-0525-4.

[3] B.M. Alkan, F. Fidan, A. Tosun, Ö. Ardıçoğlu, Quality of life and self-reported disability in patients with knee osteoarthritis, Modern Rheumatology. 24 (2014) 166–171. https://doi.org/10.3109/14397595.2013.854046.

[4] M. Suka, K. Yoshida, The National Burden of Musculoskeletal Pain in Japan, The Clinical Journal of Pain. 25 (2009) 313–319. https://doi.org/10.1097/AJP.0b013e31818c00c5.

[5] C. Milner, Functional Anatomy for Sport and Exercise, Routledge, 2008. https://doi.org/10.4324/9780203886205.

[6] G.L. Smidt, Biomechanical analysis of knee flexion and extension, Journal of Biomechanics. 6 (1973) 79–92. https://doi.org/10.1016/0021-9290(73)90040-7.

[7] D.T. Felson, C.E. Chaisson, C.L. Hill, S.M.S. Totterman, M.E. Gale, K.M. Skinner, L. Kazis, D.R. Gale, Increasing Prevalence of Knee Pain and Symptomatic Knee Osteoarthritis: Survey and Cohort Data, Annals of Internal Medicine. (2017) 541–549.

[8] F. Eckstein, F. Cicuttini, J.-P. Raynauld, J.C. Waterton, C. Peterfy, Magnetic resonance imaging (MRI) of articular cartilage in knee osteoarthritis (OA): morphological assessment, Osteoarthritis and Cartilage. 14 (2006) 46–75. https://doi.org/10.1016/j.joca.2006.02.026.

[9] J.A. Vallotton, R.A. Meuli, P.F. Leyvraz, M. Landry, Comparison between magnetic resonance imaging and arthroscopy in the diagnosis of patellar cartilage lesions, Knee Surgery, Sports Traumatology, Arthroscopy. 3 (1995) 157–162. https://doi.org/10.1007/BF01565475.

[10] D.R. Eyre, The collagens of articular cartilage, Seminars in Arthritis and Rheumatism. 21 (1991) 2–11. https://doi.org/10.1016/0049-0172(91)90035-X.

[11] D.R. Eyre, M.A. Weis, J.J. Wu, Articular cartilage collagen: An irreplaceable framework?, European Cells and Materials. 12 (2006) 14.

[12] K. Bacon, M.P. LaValley, S.R. Jafarzadeh, D. Felson, Does cartilage loss cause pain in osteoarthritis and if so, how much?, Annals of the Rheumatic Diseases. 79 (2020) 1105–1110. https://doi.org/10.1136/annrheumdis-2020-217363.

[13] Medical Topia Soka, (n.d.). https://www.mtopia.jp/orthopedics/sports_orthopedics/index04.html (accessed October 2, 2021).

[14] A. Suponenkovs, Z. Markovics, A. Platkajis, Computer Analysis of Knee by Magnetic Resonance Imaging Data, Procedia Computer Science. 104 (2017) 354–361. https://doi.org/10.1016/j.procs.2017.01.145.

[15] E.K. Danso, J.T.J. Honkanen, S. Saarakkala, R.K. Korhonen, Comparison of nonlinear mechanical properties of bovine articular cartilage and meniscus, Journal of Biomechanics. 47 (2014) 200–206. https://doi.org/10.1016/j.jbiomech.2013.09.015.

[16] K.A. Athanasiou, J. Sanchez-Adams, Engineering the Knee Meniscus, Synthesis Lectures on Tissue Engineering. 1 (2009) 1–97. https://doi.org/10.2200/S00186ED1V01Y200903TIS001.

[17] M. Englund, A. Guermazi, L.S. Lohmander, The Meniscus in Knee Osteoarthritis, Rheumatic Disease Clinics of North America. 35 (2009) 579–590. https://doi.org/10.1016/j.rdc.2009.08.004.

[18] J.T. Badlani, C. Borrero, S. Golla, C.D. Harner, J.J. Irrgang, The Effects of Meniscus Injury on the Development of Knee Osteoarthritis, The American Journal of Sports Medicine. 41 (2013) 1238–1244. https://doi.org/10.1177/0363546513490276.

[19] S. Chen, P. Fu, H. Wu, M. Pei, Meniscus, articular cartilage and nucleus pulposus: a comparative review of cartilage-like tissues in anatomy, development and function, Cell and Tissue Research. 370 (2017) 53–70. https://doi.org/10.1007/s00441-017-2613-0.

[20] Stanford health care, (n.d.). https://stanfordhealthcare.org/medical-conditions/bones-joints-and-muscles/knee-ligament-injury/types.html (accessed October 3, 2021).

[21] J.C. HUGHSTON, A.F. EILERS, The Role of the Posterior Oblique Ligament in Repairs of Acute Medial (Collateral) Ligament Tears of the Knee, The Journal of Bone & Joint Surgery. 55 (1973) 923–940. https://doi.org/10.2106/00004623-197355050-00002.

[22] M. Favero, R. Ramonda, M.B. Goldring, S.R. Goldring, L. Punzi, Early knee osteoarthritis, RMD Open. 1 (2015) 1–7. https://doi.org/10.1136/rmdopen-2015-000062.

[23] A.I.Kapandji, Physiology of the Joints, Vol.2, 7th ed, HANDSPRING PUB LTD, 2019.

[24] Range of Motion After Joint Replacement Surgery, (n.d.). https://peerwell.co/blog/range-of-motion-after-joint-replacement-surgery/ (accessed November 3, 2021).

[25] J. Goodfellow, D. Hungerford, M. Zindel, Patello-femoral joint mechanics and pathology. 1. Functional anatomy of the patello-femoral joint, The Journal of Bone and Joint Surgery. British Volume. 58-B (1976) 287–290. https://doi.org/10.1302/0301-620X.58B3.956243.

[26] S. Fathy, M. el Messiry, Study of the Effect of Cyclic Stress on the Mechanical Properties of Braided Anterior Cruciate Ligament (ACL), Journal of Textile Science & Engineering. 06 (2016). https://doi.org/10.4172/2165-8064.1000252.

[27] Knee pain, MAYO CLINC. (2021). https://www.mayoclinic.org/diseases-conditions/knee-pain/symptoms-causes/syc-20350849?p=1 (accessed November 3, 2021).

[28] M.D. Kohn, A.A. Sassoon, N.D. Fernando, Classifications in Brief: Kellgren-Lawrence

Classification of Osteoarthritis, Clinical Orthopaedics & Related Research. 474 (2016) 1886–1893. https://doi.org/10.1007/s11999-016-4732-4.

[29] J.H. Kellgren, J.S. Lawrence, Radiological Assessment of Osteo-Arthrosis, Annals of the Rheumatic Diseases. 16 (1957). https://doi.org/10.1136/ard.16.4.494.

[30] Y. Matsui, Y. Kadoya, K. Uehara, A. Kobayashi, K. Takaoka, Rotational deformity in varus osteoarthritis of the knee: analysis with computed tomography., Clinical Orthopaedics and Related Research. (2005) 147–51. https://doi.org/10.1097/01.blo.0000150465.29883.83.

[31] N.A. Segal, A. Guermazi, Advances in visualization of knee cartilage and meniscal morphology with standing computed tomography, Osteoarthritis and Cartilage. 24 (2016). https://doi.org/10.1016/j.joca.2016.01.559.

[32] W.M. Oo, M.T. Bo, Role of Ultrasonography in Knee Osteoarthritis, JCR: Journal of Clinical Rheumatology. 22 (2016). https://doi.org/10.1097/RHU.0000000000000436.

[33] K. Nagai, T. Nakamura, F.H. Fu, The diagnosis of early osteoarthritis of the knee using magnetic resonance imaging, Annals of Joint. 3 (2018). https://doi.org/10.21037/aoj.2018.12.05.

[34] T.I. Alves, G. Girish, M. Kalume Brigido, J.A. Jacobson, US of the Knee: Scanning Techniques, Pitfalls, and Pathologic Conditions, RadioGraphics. 36 (2016) 1759–1775. https://doi.org/10.1148/rg.2016160019.

[35] S. Bianchi, C. Martinoli, Ultrasound of the Musculoskeletal System, Springer Berlin Heidelberg, Berlin, Heidelberg, 2007. https://doi.org/10.1007/978-3-540-28163-4.

[36] Yuan Ling, Normal knee MRI - 10 year old male, (n.d.). https://radiopaedia.org/cases/normal-knee-mri-10-year-old-male (accessed November 6, 2021).

[37] K. Rönn, N. Reischl, E. Gautier, M. Jacobi, Current Surgical Treatment of Knee Osteoarthritis, Arthritis. 2011 (2011) 1–9. https://doi.org/10.1155/2011/454873.

[38] W.G. Kernohan, D.E. Beverland, G.F. McCoy, A. Hamilton, P. Watson, R. Mollan, Vibration arthrometry, Acta Orthopaedica Scandinavica. 61 (1990). https://doi.org/10.3109/17453679008993071.

[39] C.F. Walters, THE VALUE OF JOINT AUSCULTATION., The Lancet. 213 (1929). https://doi.org/10.1016/S0140-6736(00)79189-6.

[40] C.B. Frank, R.M. Rangayyan, G.D. Bell, Analysis of knee joint sound signals for non-invasive diagnosis of cartilage pathology, IEEE Engineering in Medicine and Biology Magazine. 9 (1990). https://doi.org/10.1109/51.62910.

[41] W.E. BLODGETT, Auscultation of the Knee Joint, The Boston Medical and Surgical Journal. 146 (1902). https://doi.org/10.1056/NEJM190201161460304.

[42] F.W. MERCER, AN IMPROVED STETHOSCOPE., JAMA: The Journal of the American Medical Association. XXX (1898). https://doi.org/10.1001/jama.1898.72440620040034.

[43] H. FISCHER, E.W. JOHNSON, Analysis of sounds from normal and pathologic knee joints., Archives of Physical Medicine and Rehabilitation. 42 (1961).

[44] M.L. Chu, I.A. Gradisar, M.R. Railey, G.F. Bowling, An electro-acoustical technique for the detection of knee joint noise., Medical Research Engineering. 12 (1976).

[45] M.L. Chu, I.A. Gradisar, M.R. Railey, G.F. Bowling, Detection of knee joint diseases using acoustical pattern recognition technique, Journal of Biomechanics. 9 (1976). https://doi.org/10.1016/0021-9290(76)90149-4.

[46] R.A.B. Mollan, G.W. Kernohan, P.H. Watters, Artefact encountered by the vibration detection system, Journal of Biomechanics. 16 (1983). https://doi.org/10.1016/0021-9290(83)90126-4.

[47] R.M. Rangayyan, C.B. Frank, G.D. Bell, R. Smith, Analysis of knee joint sound signals, in: Proceedings of the Annual International Conference of the IEEE Engineering in Medicine and Biology Society, IEEE, 1988. https://doi.org/10.1109/IEMBS.1988.94951.

[48] J. INOUE, Y. NAGATA, K. SUZUKI, Measurement or Knee Joint Sounds by Microphone, Journal of UOEH. 8 (1986). https://doi.org/10.7888/juoeh.8.307.

[49] G. McCoy, J. McCrea, D. Beverland, W. Kernohan, R. Mollan, Vibration arthrography as a diagnostic aid in diseases of the knee. A preliminary report, The Journal of Bone and Joint Surgery. British Volume. 69-B (1987). https://doi.org/10.1302/0301-620X.69B2.3818762.

[50] Peng Cheng, B. Oelmann, Joint-Angle Measurement Using Accelerometers and Gyroscopes—A Survey, IEEE Transactions on Instrumentation and Measurement. 59 (2010). https://doi.org/10.1109/TIM.2009.2024367.

[51] R. Williamson, B.J. Andrews, Detecting absolute human knee angle and angular velocity using accelerometers and rate gyroscopes, Medical & Biological Engineering & Computing. 39 (2001). https://doi.org/10.1007/BF02345283.

[52] K. Equbal, P. Dutta, S. Nageswaran, Feature Extraction and Classification of VAG Signal of Human Knee for Early Diagnosis of Chondromalacia Patella, in: 2021. https://doi.org/10.1007/978-981-15-8221-9_273.

[53] Y. Wu, Knee Joint Vibroarthrographic Signal Processing and Analysis, Springer Berlin Heidelberg, Berlin, Heidelberg, 2015. https://doi.org/10.1007/978-3-662-44284-5.

[54] R. Gong, H. Ohtsu, K. Hase, S. Ota, Vibroarthrographic signals for the low-cost and computationally efficient classification of aging and healthy knees, Biomedical Signal Processing and Control. 70 (2021) 103003. https://doi.org/10.1016/j.bspc.2021.103003.

[55] R. GONG, K. HASE, H. GOTO, K. YOSHIOKA, S. OTA, Knee osteoarthritis detection based on the combination of empirical mode decomposition and wavelet analysis, Journal of Biomechanical Science and Engineering. 15 (2020) 20-00017-20–00017. https://doi.org/10.1299/jbse.20-00017.

[56] N. Tanaka, M. Hoshiyama, Vibroarthrography in patients with knee arthropathy, Journal of

Back and Musculoskeletal Rehabilitation. 25 (2012) 117–122. https://doi.org/10.3233/BMR-2012-0319.

[57] A. Samani, R.E. Andersen, L. Arendt-Nielsen, P. Madeleine, Discrimination of knee osteoarthritis patients from asymptomatic individuals based on pain sensitivity and knee vibroarthrographic recordings, Physiological Measurement. 41 (2020) 055002. https://doi.org/10.1088/1361-6579/ab8857.

[58] K.S. Kim, J.H. Seo, C.G. Song, An Acoustical Evaluation of Knee Sound for Non-invasive Screening and Early Detection of Articular Pathology, Journal of Medical Systems. 36 (2012). https://doi.org/10.1007/s10916-010-9539-3.

[59] K. Umapathy, S. Krishnan, Modified Local Discriminant Bases Algorithm and Its Application in Analysis of Human Knee Joint Vibration Signals, IEEE Transactions on Biomedical Engineering. 53 (2006). https://doi.org/10.1109/TBME.2005.869787.

[60] A. Khamparia, B. Pandey, F. Al-Turjman, P. Podder, An intelligent IoMT enabled feature extraction method for early detection of knee arthritis, Expert Systems. (2021). https://doi.org/10.1111/exsy.12784.

[61] P. Madeleine, R.E. Andersen, J.B. Larsen, L. Arendt-Nielsen, A. Samani, Wireless multichannel vibroarthrographic recordings for the assessment of knee osteoarthritis during three activities of daily living, Clinical Biomechanics. 72 (2020) 16–23. https://doi.org/10.1016/j.clinbiomech.2019.11.015.

[62] C.-S. Shieh, C.-D. Tseng, L.-Y. Chang, W.-C. Lin, L.-F. Wu, H.-Y. Wang, P.-J. Chao, C.-L. Chiu, T.-F. Lee, Synthesis of vibroarthrographic signals in knee osteoarthritis diagnosis training, BMC Research Notes. 9 (2016) 352. https://doi.org/10.1186/s13104-016-2156-6.

[63] S. Krishnan, R.M. Rangayyan, Denoising knee joint vibration signals using adaptive time-frequency representations, in: Engineering Solutions for the Next Millennium. 1999 IEEE Canadian Conference on Electrical and Computer Engineering (Cat. No.99TH8411), IEEE, n.d. https://doi.org/10.1109/CCECE.1999.804930.

[64] D.S. Watson, J. Krutzinna, I.N. Bruce, C.E. Griffiths, I.B. McInnes, M.R. Barnes, L. Floridi, Clinical applications of machine learning algorithms: beyond the black box, BMJ. (2019). https://doi.org/10.1136/bmj.l886.

[65] S.H. Rahangdale, A.K. Mittra, Vibroarthrographic Signals De-Noising Using Wavelet Subband Thresholding, (2013) 286–289.

[66] A. Łysiak, A. Froń, D. Bączkowicz, M. Szmajda, Vibroarthrographic Signal Spectral Features in 5-Class Knee Joint Classification, Sensors. 20 (2020) 5015. https://doi.org/10.3390/s20175015.

[67] D. Bączkowicz, E. Majorczyk, K. Kręcisz, Age-Related Impairment of Quality of Joint Motion in Vibroarthrographic Signal Analysis, BioMed Research International. 2015 (2015) 1–7.

https://doi.org/10.1155/2015/591707.

[68] S. Yang, S. Cai, F. Zheng, Y. Wu, K. Liu, M. Wu, Q. Zou, J. Chen, Representation of fluctuation features in pathological knee joint vibroarthrographic signals using kernel density modeling method, Medical Engineering and Physics. 36 (2014) 1305–1311. https://doi.org/10.1016/j.medengphy.2014.07.008.

[69] Y.T. Chiang, C.H. Lu, C.C. Tuan, T.F. Lee, Y.C. Huang, M.C. Chen, Non-invasive detection of sound signals for diagnosis of ligament injuries around knee based on mel-frequency cepstrum, Frontiers in Artificial Intelligence and Applications. 274 (2015) 1940–1949. https://doi.org/10.3233/978-1-61499-484-8-1940.

[70] Y. TOZAWA, K. HASE, S. OTA, T. SAKAI, A basic study on diagnosis method of knee osteoarthritis by articular sound, The Proceedings of Conference of Kanto Branch. 2014.20 (2014) _10210-1_-_10210-2_. https://doi.org/10.1299/jsmekanto.2014.20._10210-1_.

[71] F. Weinberg, The history of the stethoscope., Canadian Family Physician Medecin de Famille Canadien. 39 (1993) 2223–4.

[72] K. Hase, R. Gong, S. Ota, Knee osteoarthritis diagnostic system(Japanese patent application), No.2021-105755, 2021.

[73] V.J. VIGORITA, Orthopaedic pathology, Lippincott Williams & Wilkins., 2008.

[74] J. Martel-Pelletier, Pathophysiology of osteoarthritis, Osteoarthritis and Cartilage. 96 (1999) 371–373.

[75] J.W. Prescott, M. Pennell, T.M. Best, M.S. Swanson, F. Haq, R. Jackson, M.N. Gurcan, An automated method to segment the femur for osteoarthritis research, Proceedings of the 31st Annual International Conference of the IEEE Engineering in Medicine and Biology Society: Engineering the Future of Biomedicine, EMBC 2009. (2009) 6364–6367. https://doi.org/10.1109/IEMBS.2009.5333257.

[76] R.S. Fife, K.D. Brandt, E.M. Braunstein, B.P. Katz, K.D. Shelbourne, L.A. Kalasinski, S. Ryan, Relationship between arthroscopic radiographic evidence of joint space of the knee, Arthritis & Rheumatism. 34 (1991) 377–382.

[77] L. Shamir, S.M. Ling, W.W. Scott, A. Bos, N. Orlov, T.J. MacUra, D.M. Eckley, L. Ferrucci, I.G. Goldberg, Knee X-ray image analysis method for automated detection of osteoarthritis, IEEE Transactions on Biomedical Engineering. 56 (2009) 407–415. https://doi.org/10.1109/TBME.2008.2006025.

[78] D. Bączkowicz, E. Majorczyk, K. Kręcisz, Age-related impairment of quality of joint motion in vibroarthrographic signal analysis, BioMed Research International. 2015 (2015). https://doi.org/10.1155/2015/591707.

[79] D. Coggon, I. Reading, P. Croft, M. McLaren, D. Barrett, C. Cooper, Knee osteoarthritis and obesity, International Journal of Obesity. 25 (2001) 622–627.

https://doi.org/10.1038/sj.ijo.0801585.

[80] K. Sinusas, Osteoarthritis:Diagnosis and treatment, American Family Physician. 85 (2012) 49–56. https://doi.org/10.1136/bmj.1.5222.355-a.

[81] C.B. Frank, R.M. Rangayyan, G.D. Bell, Analysis of Knee Joint Sound Signals for Non-Invasive Diagnosis of Cartilage Pathology, IEEE Engineering in Medicine and Biology Magazine. 9 (1990) 65–68. https://doi.org/10.1109/51.62910.

[82] and J.S.Lawrence. Kellegren, J. H., Radiological assessment of osteoarthritis, Ann Rheum Dis. 16.4 (1957) 494–501.

[83] P.M.M. Cashman, R.I. Kitney, M.A. Gariba, M.E. Carter, Automated techniques for visualization and mapping of articular cartilage in MR images of the osteoarthritic knee: A base technique for the assessment of microdamage and submicro damage, IEEE Transactions on Nanobioscience. 1 (2002) 42–51. https://doi.org/10.1109/TNB.2002.806916.

[84] D.W. Polly, J.J. Callaghan, R.A. Sikes, J.M. McCabe, K. McMahon, C.G. Savory, The accuracy of selective magnetic resonance imaging compared with the findings of arthroscopy of the knee, Journal of Bone and Joint Surgery - Series A. 70 (1988) 192–198. https://doi.org/10.2106/00004623-198870020-00005.

[85] W.G. Kernohan, D.E. Beverland, G.F. Mccoy, A. Hamilton, P. Watson, R. Mollan, Vibration arthrometry, Acta Orthopaedica. 61 (1990) 70–79. https://doi.org/10.3109/17453679008993071.

[86] S. Ota, R. Fujita, N. Segawa, R. Tanaka, S. Inagawa, T. Sakai, Clinical analytical vibroarthrography method for classifying patients with knee osteoarthritis, Osteoarthritis and Cartilage. 27 (2019) S115–S116. https://doi.org/10.1016/j.joca.2019.02.171.

[87] D.B. Percival, Wavelet Methods for Time Series Analysis, Cambridge University Press, 2010.

[88] S. Cai, Y. Wu, N. Xiang, Z. Zhong, J. He, L. Shi, F. Xu, Detrending knee joint vibration signals with a cascade moving average filter, Proceedings of the Annual International Conference of the IEEE Engineering in Medicine and Biology Society, EMBS. (2012) 4357–4360. https://doi.org/10.1109/EMBC.2012.6346931.

[89] M.A. Islam, K. Sundaraj, R.B. Ahmad, N.U. Ahamed, Mechanomyogram for Muscle Function Assessment: A Review, PLoS ONE. 8 (2013). https://doi.org/10.1371/journal.pone.0058902.

[90] N.E. Huang, Z. Shen, S.R. Long, A NEW VIEW OF NONLINEAR WATER WAVES: The Hilbert Spectrum, Annual Review of Fluid Mechanics. 31 (1999) 417–457. https://doi.org/10.1146/annurev.fluid.31.1.417.

[91] N.E. Huang, Z. Shen, S.R. Long, M.C. Wu, H.H. Snin, Q. Zheng, N.C. Yen, C.C. Tung, H.H. Liu, The empirical mode decomposition and the Hubert spectrum for nonlinear and non-stationary time series analysis, Proceedings of the Royal Society A: Mathematical, Physical and Engineering Sciences. 454 (1998) 903–995. https://doi.org/10.1098/rspa.1998.0193.

[92] M.T. Gencoglu, M. Uyar, Prediction of flashover voltage of insulators using least squares support vector machines, Expert Systems with Applications. 36 (2009) 10789–10798. https://doi.org/10.1016/j.eswa.2009.02.021.

[93] J.A.K. Suykens, L. Lukas, P. van Dooren, B. de Moor, J. Vandewalle, Least Squares Support Vector Machine Classifers: a Large Scale Algorithm, European Conference on Circuit Theory and Design. (1999) 839–842.

[94] W.H. Land, X. Qiao, D.E. Margolis, W.S. Ford, C.T. Paquette, J.F. Perez-Rogers, J.A. Borgia, J.Y. Yang, Y. Deng, Kernelized partial least squares for feature reduction and classification of gene microarray data, BMC Systems Biology. 5 (2011) S13. https://doi.org/10.1186/1752-0509-5-S3-S13.

[95] J. Fan, S. Upadhye, A. Worster, M ETHODOLOGY (ROC) curves, Can J Emerg Med. 8 (2006) 19–20.

[96] W. Zhu, N. Zeng, N. Wang, Sensitivity, specificity, accuracy, associated confidence interval and ROC analysis with practical SAS® implementations., Northeast SAS Users Group 2010: Health Care and Life Sciences. (2010) 1–9.

[97] Y. Athavale, S. Krishnan, A telehealth system framework for assessing knee-joint conditions using vibroarthrographic signals, Biomedical Signal Processing and Control. 55 (2020) 101580. https://doi.org/10.1016/j.bspc.2019.101580.

[98] S. Nalband, A. Prince, A. Agrawal, Entropy-based feature extraction and classification of vibroarthographic signal using complete ensemble empirical mode decomposition with adaptive noise, IET Science, Measurement and Technology. 12 (2018) 350–359. https://doi.org/10.1049/iet-smt.2017.0284.

[99] G. Peat, R. McCarney, P. Croft, Knee pain and osteoarthritis in older adults: A review of community burden and current use of primary health care, Annals of the Rheumatic Diseases. 60 (2001) 91–97. https://doi.org/10.1136/ard.60.2.91.

[100] S.A. Haq, F. Davatchi, Osteoarthritis of the knees in the COPCORD world, International Journal of Rheumatic Diseases. 14 (2011) 122–129. https://doi.org/10.1111/j.1756-185X.2011.01615.x.

[101] K. Magnusson, J. Kumm, A. Turkiewicz, M. Englund, A naturally aging knee, or development of early knee osteoarthritis?, Osteoarthritis and Cartilage. 26 (2018) 1447–1452. https://doi.org/10.1016/j.joca.2018.04.020.

[102] D. Scott, A. Kowalczyk, Osteoarthritis of the knee, BMJ Clinical Evidence. 2007 (2007).

[103] D.J. Hunter, A. Guermazi, G.H. Lo, A.J. Grainger, P.G. Conaghan, R.M. Boudreau, F.W. Roemer, Evolution of semi-quantitative whole joint assessment of knee OA: MOAKS (MRI Osteoarthritis Knee Score), Osteoarthritis and Cartilage. 19 (2011) 990–1002. https://doi.org/10.1016/j.joca.2011.05.004.

[104] J.S. Richman, J.R. Moorman, Physiological time-series analysis using approximate entropy and sample entropy maturity in premature infants Physiological time-series analysis using approximate entropy and sample entropy, Americal Journal of Physiology Heart and Circulatory Physiology. 278 (2000) H2039–H2049.

[105] S. Krishnan, R.M. Rangayyan, Automatic de-noising of knee-joint vibration signals using adaptive time-frequency representations, Medical and Biological Engineering and Computing. 38 (2000) 2–8. https://doi.org/10.1007/BF02344681.

[106] Y. Wu, S. Yang, F. Zheng, S. Cai, M. Lu, M. Wu, Removal of artifacts in knee joint vibroarthrographic signals using ensemble empirical mode decomposition and detrended fluctuation analysis, Physiological Measurement. 35 (2014) 429–439. https://doi.org/10.1088/0967-3334/35/3/429.

[107] B.H. Tracey, E.L. Miller, Nonlocal Means Denoising of ECG Signals, IEEE Transactions on Biomedical Engineering. 59 (2012) 2383–2386. https://doi.org/10.1109/TBME.2012.2208964.

[108] R. Gong, K. Hase, H. Goto, K. Yoshioka, Post-processing algorithm for removing soft-tissue movement artifacts from vibroarthrographic knee-joint signal, in: 2020 42nd Annual International Conference of the IEEE Engineering in Medicine & Biology Society (EMBC), IEEE, 2020: pp. 936–939. https://doi.org/10.1109/EMBC44109.2020.9176271.

[109] Chengyu Liu;Jianqing Li, Feature Engineering and Computational Intelligence in ECG Monitoring, Springer Singapore, Singapore, 2020. https://doi.org/10.1007/978-981-15-3824-7.

[110] Martha Refugio Ortiz-Posadas, Pattern Recognition Techniques Applied to Biomedical Problems, Springer International Publishing, 2020. https://doi.org/10.1007/978-3-030-38021-2.

[111] N. Befrui, J. Elsner, A. Flesser, J. Huvanandana, O. Jarrousse, T.N. Le, M. Müller, W.H.W. Schulze, S. Taing, S. Weidert, Vibroarthrography for early detection of knee osteoarthritis using normalized frequency features, Medical & Biological Engineering & Computing. 56 (2018) 1499–1514. https://doi.org/10.1007/s11517-018-1785-4.

[112] M. Hudelmaier, C. Glaser, J. Hohe, K.H. Englmeier, M. Reiser, R. Putz, F. Eckstein, Age-related changes in the morphology and deformational behavior of knee joint cartilage, Arthritis and Rheumatism. 44 (2001) 2556–2561. https://doi.org/10.1002/1529-0131(200111)44:11<2556::AID-ART436>3.0.CO;2-U.

[113] C.R. Reid, P.M.C. Bush, N.H. Cummings, D.L. McMullin, S.K. Durrani, A review of occupational knee disorders, Journal of Occupational Rehabilitation. 20 (2010) 489–501. https://doi.org/10.1007/s10926-010-9242-8.

[114] C. Johnson, Measuring Pain. Visual Analog Scale Versus Numeric Pain Scale: What is the Difference?, Journal of Chiropractic Medicine. 4 (2005) 43–44.

https://doi.org/10.1016/S0899-3467(07)60112-8.

[115] S.M. Ling, L.P. Fried, E.S. Garrett, M. yu Fan, T. Rantanen, J.M. Bathon, Knee osteoarthritis compromises early mobility function: The Women's Health and Aging Study II, Journal of Rheumatology. 30 (2003) 114–120.

[116] P.E. Bijur, W. Silver, E.J. Gallagher, Reliability of the visual analog scale for measurement of acute pain, Academic Emergency Medicine. 8 (2001) 1153–1157. https://doi.org/10.1111/j.1553-2712.2001.tb01132.x.

[117] S. Ota, A. Ando, Y. Tozawa, T. Nakamura, S. Okamoto, T. Sakai, K. Hase, Preliminary study of optimal measurement location on vibroarthrography for classification of patients with knee osteoarthritis, Journal of Physical Therapy Science. 28 (2016) 2904–2908. https://doi.org/10.1589/jpts.28.2904.

[118] S. Achelis, Technical Analysis from A to Z, 2nd Edition, 2nd Editio, McGraw-Hill Education, 2013.

[119] A.R. Merletti, P. Torino, Standards for Reporting EMG Data, Journal of Electromyography and Kinesiology. 25 (2015) I–II. https://doi.org/10.1016/s1050-6411(15)00221-7.

[120] P. Singh, G. Pradhan, S. Shahnawazuddin, Denoising of ECG signal by non-local estimation of approximation coefficients in DWT, Biocybernetics and Biomedical Engineering. 37 (2017) 599–610. https://doi.org/10.1016/j.bbe.2017.06.001.

[121] E. Estrada, H. Nazeran, G. Sierra, F. Ebrahimi, S.K. Setarehdan, Wavelet-based EEG denoising for automatic sleep stage classification, CONIELECOMP 2011 - 21st International Conference on Electronics Communications and Computers, Proceedings. (2011) 295–298. https://doi.org/10.1109/CONIELECOMP.2011.5749325.

[122] P. Nguyen, J.M. Kim, Adaptive ECG denoising using genetic algorithm-based thresholding and ensemble empirical mode decomposition, Information Sciences. 373 (2016) 499–511. https://doi.org/10.1016/j.ins.2016.09.033.

[123] K. Dabov, R. Foi, V. Katkovnik, K. Egiazarian, BM3D image denoising with shape-adaptive principal component analysis, Proc. Workshop on Signal Processing with Adaptive Sparse Structured Representations. (2009) 6.

[124] B. Yang, A STUDY OF INVERSE SHORT-TIME FOURIER TRANSFORM Bin Yang Chair of System Theory and Signal Processing , University of Stuttgart , Germany, System. (2008) 3541–3544.

[125] Q. Hu, Q. Zhang, X.S. Si, A.S. Qin, Q.H. Zhang, Fault Diagnosis Based on Multi-Scale Redefined Dimensionless Indicators and Density Peak Clustering with Geodesic Distances, IEEE Access. 8 (2020) 84777–84791. https://doi.org/10.1109/ACCESS.2020.2989460.

[126] B.R. Nayana, P. Geethanjali, Analysis of Statistical Time-Domain Features Effectiveness in Identification of Bearing Faults From Vibration Signal, IEEE Sensors Journal. 17 (2017)

5618–5625. https://doi.org/10.1109/JSEN.2017.2727638.

[127] X. Zhang, J. Zhou, Multi-fault diagnosis for rolling element bearings based on ensemble empirical mode decomposition and optimized support vector machines, Mechanical Systems and Signal Processing. 41 (2013) 127–140. https://doi.org/10.1016/j.ymssp.2013.07.006.

[128] A. Delgado-Bonal, A. Marshak, Approximate entropy and sample entropy: A comprehensive tutorial, 2019. https://doi.org/10.3390/e21060541.

[129] Z. Yu, H. Chen, J. Liuxs, J. You, H. Leung, G. Han, Hybrid κ-Nearest Neighbor Classifier, IEEE Transactions on Cybernetics. 46 (2016) 1263–1275. https://doi.org/10.1109/TCYB.2015.2443857.

[130] S. Nalband, A. Prince, A. Agrawal, Entropy-based feature extraction and classification of vibroarthographic signal using complete ensemble empirical mode decomposition with adaptive noise, IET Science, Measurement and Technology. 12 (2018) 350–359. https://doi.org/10.1049/iet-smt.2017.0284.

[131] Y. Wu, P. Chen, X. Luo, H. Huang, L. Liao, Y. Yao, M. Wu, R.M. Rangayyan, Quantification of knee vibroarthrographic signal irregularity associated with patellofemoral joint cartilage pathology based on entropy and envelope amplitude measures, Computer Methods and Programs in Biomedicine. 130 (2016) 1–12. https://doi.org/10.1016/j.cmpb.2016.03.021.

[132] A.A. Vandervoort, A.J. McComas, Contractile changes in opposing muscles of the human ankle joint with aging, Journal of Applied Physiology. 61 (1986) 361–367. https://doi.org/10.1152/jappl.1986.61.1.361.

[133] E. Simoneau, A. Martin, J. Van Hoecke, Muscular performances at the ankle joint in young and elderly men, Journals of Gerontology - Series A Biological Sciences and Medical Sciences. 60 (2005) 439–447. https://doi.org/10.1093/gerona/60.4.439.

[134] K. Keller, M. Engelhardt, Strength and muscle mass loss with aging process. Age and strength loss, Muscles, Ligaments and Tendons Journal. 3 (2013) 346–350. https://doi.org/10.11138/mltj/2013.3.4.346.

[135] S. Lahmiri, M. Boukadoum, A weighted bio-signal denoising approach using empirical mode decomposition, Biomedical Engineering Letters. 5 (2015) 131–139. https://doi.org/10.1007/s13534-015-0182-2.

[136] V.S. Chouhan, S.S. Mehta, Total Removal of Baseline Drift from ECG Signal, in: 2007 International Conference on Computing: Theory and Applications (ICCTA'07), IEEE, 2007: pp. 512–515. https://doi.org/10.1109/ICCTA.2007.126.

[137] F.E. Grubbs, Sample Criteria for Testing Outlying Observations, The Annals of Mathematical Statistics. 21 (1950) 27–58. https://doi.org/10.1214/aoms/1177729885.

[138] H.E. Salzer, Lagrangian Interpolation at the Chebyshev Points xn, cos (/n), = 0(1)n; some Unnoted Advantages, The Computer Journal. 15 (1972) 156–159.

https://doi.org/10.1093/comjnl/15.2.156.

[139] D.W. Jackson, T.M. Simon, H.M. Aberman, Symptomatic Articular Cartilage Degeneration, Clinical Orthopaedics and Related Research. 391 (2001) S14–S25. https://doi.org/10.1097/00003086-200110001-00003.

[140] D.B. Percival, A.T. Walden, Wavelet Methods for Time SeriesAnalysis, Cambridge University Press, Cambridge, 2000. https://doi.org/10.1017/CBO9780511841040.

[141] Rithu James, Harsha A, Liza Annie Joseph, Mixed Noise Removal by Processing of Patches, Proceedings of Engineering and Technology Innovation. (2020) 32–41. https://doi.org/10.46604/peti.2020.6082.

[142] A. Sundar, V. Pahwa, C. Das, A new method for denoising knee joint vibroarthrographic signals, in: 2015 Annual IEEE India Conference (INDICON), IEEE, 2015: pp. 1–5. https://doi.org/10.1109/INDICON.2015.7443443.

[143] J. Rahul, M. Sora, L.D. Sharma, An overview on biomedical signal analysis, in: International Journal of Recent Technology and Engineering, 2019: pp. 206–209.

[144] M.E. Torres, M.A. Colominas, G. Schlotthauer, P. Flandrin, A complete ensemble empirical mode decomposition with adaptive noise, in: 2011 IEEE International Conference on Acoustics, Speech and Signal Processing (ICASSP), IEEE, 2011: pp. 4144–4147. https://doi.org/10.1109/ICASSP.2011.5947265.

[145] P.A. Vikhar, Evolutionary algorithms: A critical review and its future prospects, in: 2016 International Conference on Global Trends in Signal Processing, Information Computing and Communication (ICGTSPICC), IEEE, 2016: pp. 261–265. https://doi.org/10.1109/ICGTSPICC.2016.7955308.

[146] R. Gong, K. Hase, A Plant Root System Algorithm Based on Swarm Intelligence for One-dimensional Biomedical Signal Feature Engineering, ArXiv.Org. (2021). http://arxiv.org/abs/2108.00214.

[147] L. Li, Z. Fang, Y. Ma, B. Wang, H. Dong, Z. Zhang, Research on Traffic Signal Timing Method Based on Ant Colony Algorithm and Fuzzy Control Theory, Proceedings of Engineering and Technology Innovation. 11 (2019) 21–29.

[148] R. Carter,Mancini, Bruce, Op Amps for Everyone, Elsevier, 2009. https://doi.org/10.1016/B978-1-85617-505-0.X0001-4.

[149] B. Boashash, Time-Frequency Signal Analysis and Processing, Elsevier, 2016.

[150] Z. WU, N.E. HUANG, ENSEMBLE EMPIRICAL MODE DECOMPOSITION: A NOISE-ASSISTED DATA ANALYSIS METHOD, Advances in Adaptive Data Analysis. 01 (2009) 1–41. https://doi.org/10.1142/S1793536909000047.

[151] M. Tanweer, K.A.I. Halonen, Development of wearable hardware platform to measure the ECG and EMG with IMU to detect motion artifacts, in: 2019 IEEE 22nd International

Symposium on Design and Diagnostics of Electronic Circuits & Systems (DDECS), IEEE, 2019: pp. 1–4. https://doi.org/10.1109/DDECS.2019.8724639.

[152] R. GONG, K. HASE, H. GOTO, K. YOSHIOKA, S. OTA, Knee osteoarthritis detection based on the combination of empirical mode decomposition and wavelet analysis, Journal of Biomechanical Science and Engineering. 15 (2020) 20-00017-20–00017. https://doi.org/10.1299/jbse.20-00017.

[153] R. Schafer, What Is a Savitzky-Golay Filter? [Lecture Notes], IEEE Signal Processing Magazine. 28 (2011) 111–117. https://doi.org/10.1109/MSP.2011.941097.

[154] S. Dubnov, Generalization of Spectral Flatness Measure for Non-Gaussian Linear Processes, IEEE Signal Processing Letters. 11 (2004) 698–701. https://doi.org/10.1109/LSP.2004.831663.

[155] K. Socha, M. Dorigo, Ant colony optimization for continuous domains, European Journal of Operational Research. 185 (2008) 1155–1173. https://doi.org/10.1016/j.ejor.2006.06.046.

[156] A. Sundar, C. Das, V. Pahwa, Denoising Knee Joint Vibration Signals Using Variational Mode Decomposition, in: 2016: pp. 719–729. https://doi.org/10.1007/978-81-322-2755-7_74.

[157] S. Poornachandra, N. Kumaravel, Subband-Adaptive Shrinkage for Denoising of ECG Signals, EURASIP Journal on Advances in Signal Processing. 2006 (2006) 081236. https://doi.org/10.1155/ASP/2006/81236.

[158] N. Tanaka, M. Hoshiyama, ARTICULAR SOUND AND CLINICAL STAGES IN KNEE ARTHROPATHY, Journal of Musculoskeletal Research. 14 (2011) 1150006. https://doi.org/10.1142/S0218957711500060.

[159] G. Tzanetakis, G. Essl, P. ~R. Cook, Audio Analysis using the Discrete Wavelet Transform, in: Proceedings of the WSES International Conference Acoustics and Music: Theory and Applications (AMTA 2001), 2001: pp. 318–323.

[160] S.P. Messier, D.J. Gutekunst, C. Davis, P. DeVita, Weight loss reduces knee-joint loads in overweight and obese older adults with knee osteoarthritis, Arthritis and Rheumatism. 52 (2005) 2026–2032. https://doi.org/10.1002/art.21139.

[161] B. Haviv, S. Bronak, R. Thein, The complexity of pain around the knee in patients with osteoarthritis, Israel Medical Association Journal. 15 (2013) 178–181.

[162] D.I. Rhon, K.G. Perez, S.L. Eskridge, Risk of post-traumatic knee osteoarthritis after knee injury in military service members, Musculoskeletal Care. 17 (2019) 113–119. https://doi.org/10.1002/msc.1378.

[163] K. Kręcisz, D. Bączkowicz, Analysis and multiclass classification of pathological knee joints using vibroarthrographic signals, Computer Methods and Programs in Biomedicine. 154 (2018) 37–44. https://doi.org/10.1016/j.cmpb.2017.10.027.

[164] C.S. Shieh, C.D. Tseng, L.Y. Chang, W.C. Lin, L.F. Wu, H.Y. Wang, P.J. Chao, C.L. Chiu, T.F. Lee, Synthesis of vibroarthrographic signals in knee osteoarthritis diagnosis training, BMC

Research Notes. 9 (2016) 1–10. https://doi.org/10.1186/s13104-016-2156-6.

[165] S. Fukuhara, S. Watanabe, H. Oka, Novel mechanomyogram/electromyogram hybrid transducer measurements reflect muscle strength during dynamic exercise — Pedaling of recumbent bicycle, Advanced Biomedical Engineering. 7 (2018) 47–54. https://doi.org/10.14326/abe.7.47.

[166] Z.D. Zhao, Y.Q. Chen, A new method for removal of baseline wander and power line interference in ECG signals, Proceedings of the 2006 International Conference on Machine Learning and Cybernetics. 2006 (2006) 4342–4347. https://doi.org/10.1109/ICMLC.2006.259082.

[167] R. Naga, S. Chandralingam, T. Anjaneyulu, K. Satyanarayana, Denoising EOG signal using stationary wavelet transform, Measurement Science Review. 12 (2012) 46–51. https://doi.org/10.2478/v10048-012-0010-0.

[168] A.P. Theodoros Giannakopoulos, Introduction to Audio Analysis, 2014.

[169] C. Wu, Y. Zhang, C. Hong, H. Chiueh, Implementation of ECG signal processing algorithms for removing baseline wander and electromyography interference, Proceedings of 2016 8th IEEE International Conference on Communication Software and Networks, ICCSN 2016. (2016) 118–121. https://doi.org/10.1109/ICCSN.2016.7586631.

[170] C. Wu, Y. Zhang, C. Hong, H. Chiueh, Implementation of ECG signal processing algorithms for removing baseline wander and electromyography interference, in: 2016 8th IEEE International Conference on Communication Software and Networks (ICCSN), IEEE, 2016. https://doi.org/10.1109/ICCSN.2016.7586631.

[171] N. Rastogi, R. Mehra, Analysis of Savitzky-Golay filter for baseline wander cancellation in ECG using wavelets, International Journal of Engineering Sciences & Emerging Technologies. 6 (2013) 2231–6604.

[172] D. v. Carvalho, E.M. Pereira, J.S. Cardoso, Machine Learning Interpretability: A Survey on Methods and Metrics, Electronics. 8 (2019) 832. https://doi.org/10.3390/electronics8080832.

[173] M. Gertsch, The ECG, Springer Berlin Heidelberg, Berlin, Heidelberg, 2004. https://doi.org/10.1007/978-3-662-10315-9.

[174] S. Zschocke, E.-J. Speckmann, eds., Basic Mechanisms of the EEG, Birkhäuser Boston, Boston, MA, 1993. https://doi.org/10.1007/978-1-4612-0341-4.

[175] C.J. Stam, Use of magnetoencephalography (MEG) to study functional brain networks in neurodegenerative disorders, Journal of the Neurological Sciences. 289 (2010) 128–134. https://doi.org/10.1016/j.jns.2009.08.028.

[176] G. Chaudhari, X. Jiang, A. Fakhry, A. Han, J. Xiao, S. Shen, A. Khanzada, Virufy: Global Applicability of Crowdsourced and Clinical Datasets for AI Detection of COVID-19 from Cough Audio Samples, (2020).

[177] X.-W. Wang, D. Nie, B.-L. Lu, Emotional state classification from EEG data using machine learning approach, Neurocomputing. 129 (2014) 94–106. https://doi.org/10.1016/j.neucom.2013.06.046.

[178] Z. Obermeyer, E.J. Emanuel, Predicting the Future — Big Data, Machine Learning, and Clinical Medicine, New England Journal of Medicine. 375 (2016) 1216–1219. https://doi.org/10.1056/NEJMp1606181.

[179] S.B. Kotsiantis, I.D. Zaharakis, P.E. Pintelas, Machine learning: A review of classification and combining techniques, Artificial Intelligence Review. 26 (2006) 159–190. https://doi.org/10.1007/s10462-007-9052-3.

[180] C.J. Gallego Duque, L.D. Munoz, J.G. Mejia, E. Delgado Trejos, Discrete wavelet transform and k-nn classification in EMG signals for diagnosis of neuromuscular disorders, in: 2014 XIX Symposium on Image, Signal Processing and Artificial Vision, IEEE, 2014: pp. 1–5. https://doi.org/10.1109/STSIVA.2014.7010171.

[181] E. Keogh, Naive bayes classifier, Accessed: Nov. 5 (2006) 2017.

[182] S. Mirjalili, Ant Colony Optimisation, in: Studies in Computational Intelligence, 2019: pp. 33–42. https://doi.org/10.1007/978-3-319-93025-1_3.

[183] R. Akbari, R. Hedayatzadeh, K. Ziarati, B. Hassanizadeh, A multi-objective artificial bee colony algorithm, Swarm and Evolutionary Computation. 2 (2012) 39–52. https://doi.org/10.1016/j.swevo.2011.08.001.

[184] X.-F. Song, Y. Zhang, Y.-N. Guo, X.-Y. Sun, Y.-L. Wang, Variable-Size Cooperative Coevolutionary Particle Swarm Optimization for Feature Selection on High-Dimensional Data, IEEE Transactions on Evolutionary Computation. 24 (2020) 882–895. https://doi.org/10.1109/TEVC.2020.2968743.

[185] F. Hölker, C. Wolter, E.K. Perkin, K. Tockner, Light pollution as a biodiversity threat, Trends in Ecology & Evolution. 25 (2010) 681–682. https://doi.org/10.1016/j.tree.2010.09.007.

[186] J. Krause, G.D. Ruxton, S. Krause, Swarm intelligence in animals and humans, Trends in Ecology & Evolution. 25 (2010) 28–34. https://doi.org/10.1016/j.tree.2009.06.016.

[187] F. Baluška, S. Mancuso, D. Volkmann, P. Barlow, Root apices as plant command centres : the unique ‘ brain-like ’ status of the root apex transition zone, Biologia. 59 (2004) 7–19.

[188] A. NOVOPLANSKY, Picking battles wisely: plant behaviour under competition, Plant, Cell & Environment. 32 (2009) 726–741. https://doi.org/10.1111/j.1365-3040.2009.01979.x.

[189] Q. Jiang, Y. Shen, H. Li, F. Xu, New Fault Recognition Method for Rotary Machinery Based on Information Entropy and a Probabilistic Neural Network, Sensors. 18 (2018) 337. https://doi.org/10.3390/s18020337.

[190] D. Lyon, The discrete fourier transform, part 4: Spectral leakage, Journal of Object Technology. 8 (2009) 23–34. https://doi.org/10.5381/jot.2009.8.7.c2.

[191] T.W. Rauber, F. de Assis Boldt, F.M. Varejao, Heterogeneous Feature Models and Feature Selection Applied to Bearing Fault Diagnosis, IEEE Transactions on Industrial Electronics. 62 (2015) 637–646. https://doi.org/10.1109/TIE.2014.2327589.

[192] A. Phinyomark, P. Phukpattaranont, C. Limsakul, Investigating long-term effects of feature extraction methods for continuous emg pattern classification, Fluctuation and Noise Letters. 11 (2012) 1–17. https://doi.org/10.1142/S0219477512500289.

[193] M. D'Alessandro, R. Esteller, J. Echauz, G. Vachtsevanos, A. Hinson, B. Litt, Epileptic Seizure Prediction Using Hybrid Feature Selection Over Multiple Intracranial EEG Electrode Contacts: A Report of Four Patients, IEEE Transactions on Biomedical Engineering. 50 (2003) 603–615. https://doi.org/10.1109/TBME.2003.810706.

[194] S.G.K. Patro, K.K. Sahu, Normalization: A Preprocessing Stage, IARJSET. (2015) 20–22. https://doi.org/10.17148/IARJSET.2015.2305.

[195] G. Chandrashekar, F. Sahin, A survey on feature selection methods, Computers & Electrical Engineering. 40 (2014) 16–28. https://doi.org/10.1016/j.compeleceng.2013.11.024.

[196] J.R. Quinlan, Induction of decision trees, Machine Learning. 1 (1986) 81–106. https://doi.org/10.1007/BF00116251.

[197] J. K, Convergence of Optimization Problems, Bonfring International Journal of Data Mining. 2 (2012) 13–16. https://doi.org/10.9756/bijdm.1106.

[198] J. Dougherty, R. Kohavi, M. Sahami, Supervised and Unsupervised Discretization of Continuous Features, in: Machine Learning Proceedings 1995, Elsevier, 1995: pp. 194–202. https://doi.org/10.1016/B978-1-55860-377-6.50032-3.

[199] E.G. Jobbágy, R.B. Jackson, S. Biogeochemistry, N. Mar, The distribution of soil nutrients with depth: Global patterns and the imprint of plants, Biogeochemistry. 53 (2001) 51–77. https://doi.org/https://doi.org/10.1023/A:1010760720215.

[200] R. Crang, S. Lyons-Sobaski, R. Wise, Plant Anatomy, Springer International Publishing, Cham, 2018. https://doi.org/10.1007/978-3-319-77315-5.

[201] Horst Marschner, Marschner's Mineral Nutrition of Higher Plants, Second Edi, Elsevier, 2012. https://doi.org/10.1016/C2009-0-63043-9.

[202] P. Bourke, Calculating the area and centroid of a polygon., (1988) 3–5. http://astonomy.swin.edu.ac.uk/~pbourke/geom-%5Cnetry/lineline/polyarea/, http://astonomy.swin.edu.ac.uk/~pbourke/%5Cn%5Cnhttp://www.seas.upenn.edu/~sys502/extra_materials/Polygon Area and Centroid.pdf.

[203] C.E. Metz, Basic principles of ROC analysis, Seminars in Nuclear Medicine. 8 (1978) 283–298. https://doi.org/10.1016/S0001-2998(78)80014-2.

[204] K.C. Chua, V. Chandran, U.R. Acharya, C.M. Lim, Application of higher order statistics/spectra in biomedical signals-A review, Medical Engineering and Physics. 32 (2010)

679–689. https://doi.org/10.1016/j.medengphy.2010.04.009.

[205] S. Lobov, N. Krilova, I. Kastalskiy, V. Kazantsev, V. Makarov, Latent Factors Limiting the Performance of sEMG-Interfaces, Sensors. 18 (2018) 1122. https://doi.org/10.3390/s18041122.

[206] Christoph Molnar, Interpretable Machine Learning, Lulu.com, 2020.

[207] J. V. Tu, Advantages and disadvantages of using artificial neural networks versus logistic regression for predicting medical outcomes, Journal of Clinical Epidemiology. 49 (1996) 1225–1231. https://doi.org/10.1016/S0895-4356(96)00002-9.

[208] A. Karatzoglou, A. Smola, K. Hornik, A. Zeileis, kernlab - An S4 Package for Kernel Methods in R, Journal of Statistical Software. 11 (2004). https://doi.org/10.18637/jss.v011.i09.

[209] W.N. Venables, B.D. Ripley, Modern Applied Statistics with S, Springer New York, New York, NY, 2002. https://doi.org/10.1007/978-0-387-21706-2.

[210] RStudio Team, RStudio: Integrated Development Environment for R, (2021).

[211] R Core Team, A Language and Environment for Statistical Computing, (2021).

[212] K. Hase, S. WANG, Predictive joint load evaluation system with a finite element analysis model of the knee joint and a walking generation model[in japanese], Japanese Journal of Clinical Biomechanics. 40 (2019) 53–59. http://ci.nii.ac.jp/naid/40022036580/en/ (accessed July 25, 2021).

[213] J.C. Erhart-Hledik, J. Favre, T.P. Andriacchi, New insight in the relationship between regional patterns of knee cartilage thickness, osteoarthritis disease severity, and gait mechanics, Journal of Biomechanics. 48 (2015) 3868–3875. https://doi.org/10.1016/j.jbiomech.2015.09.033.

[214] C.-H. Yoon, H.-S. Kim, J.H. Ju, W.-H. Jee, S.-H. Park, H.-Y. Kim, Validity of the sonographic longitudinal sagittal image for assessment of the cartilage thickness in the knee osteoarthritis, Clinical Rheumatology. 27 (2008) 1507–1516. https://doi.org/10.1007/s10067-008-0956-3.

[215] T.P. Andriacchi, S. Koo, S.F. Scanlan, Gait Mechanics Influence Healthy Cartilage Morphology and Osteoarthritis of the Knee, Journal of Bone and Joint Surgery. 91 (2009) 95–101. https://doi.org/10.2106/JBJS.H.01408.

[216] S. WANG, K. HASE, A. KATAOKA, T. ANDO, H. WARASHINA, Finite Element Modeling in the Osteoarthritis Patient Knee Joint and Evaluation Method of the Unloader Knee Braces, Biomechanisms. 25 (2020) 125–137. https://doi.org/10.3951/biomechanisms.25.125.

[217] S. Koo, G.E. Gold, T.P. Andriacchi, Considerations in measuring cartilage thickness using MRI: factors influencing reproducibility and accuracy, Osteoarthritis and Cartilage. 13 (2005) 782–789. https://doi.org/10.1016/j.joca.2005.04.013.

[218] E. Naredo, C. Acebes, I. Moller, F. Canillas, J.J. de Agustin, E. de Miguel, E. Filippucci, A. Iagnocco, C. Moragues, R. Tuneu, J. Uson, J. Garrido, E. Delgado-Baeza, I. Saenz-Navarro, Ultrasound validity in the measurement of knee cartilage thickness, Annals of the Rheumatic Diseases. 68 (2009) 1322–1327. https://doi.org/10.1136/ard.2008.090738.

[219] N. Nitta, M. Misawa, T. Numano, Composition and acoustic properties in a cartilage phantom, Japanese Journal of Applied Physics. 58 (2019) SGGE21. https://doi.org/10.7567/1347-4065/ab1a2d.

[220] A.F. Mak, The apparent viscoelastic behavior of articular cartilage–the contributions from the intrinsic matrix viscoelasticity and interstitial fluid flows, Journal of Biomechanical Engineering. 108 (1986) 123–130. https://doi.org/10.1115/1.3138591.

[221] D. Puppi, F. Chiellini, A.M. Piras, E. Chiellini, Polymeric materials for bone and cartilage repair, Progress in Polymer Science (Oxford). 35 (2010) 403–440. https://doi.org/10.1016/j.progpolymsci.2010.01.006.

[222] H. He, R. Li, K. Chen, Characteristics of Jerk Response Spectra for Elastic and Inelastic Systems, Shock and Vibration. 2015 (2015) 1–12. https://doi.org/10.1155/2015/782748.

[223] D.C. Lin, C.P. McGowan, K.P. Blum, L.H. Ting, Yank: the time derivative of force is an important biomechanical variable in sensorimotor systems, Journal of Experimental Biology. 222 (2019). https://doi.org/10.1242/jeb.180414.

[224] N. Golyandina, A. Korobeynikov, A. Zhigljavsky, Singular Spectrum Analysis with R, 2018.

[225] 2021 NEMA, PS3.1: DICOM PS3.1 2021b, A DICOM® Publication. (2021) 1–34. https://www.dicomstandard.org/.

[226] 3D Slicer, 3D Slicer image computing platform, (2021). https://www.slicer.org/.

[227] C. Hulet, J.P. Sabatier, D. Souquet, B. Locker, C. Marcelli, C. Vielpeau, Distribution of Bone Mineral Density at the Proximal Tibia in Knee Osteoarthritis, Calcified Tissue International. 71 (2002) 315–322. https://doi.org/10.1007/s00223-001-2112-9.

[228] F. Cicuttini, C. Ding, A. Wluka, S. Davis, P.R. Ebeling, G. Jones, Association of cartilage defects with loss of knee cartilage in healthy, middle-age adults: A prospective study, Arthritis & Rheumatism. 52 (2005) 2033–2039. https://doi.org/10.1002/art.21148.

[229] X.L. LU, V.C. MOW, Biomechanics of Articular Cartilage and Determination of Material Properties, Medicine & Science in Sports & Exercise. 40 (2008) 193–199. https://doi.org/10.1249/mss.0b013e31815cb1fc.

[230] M.S. Laasanen, J. Töyräs, R.K. Korhonen, J. Rieppo, S. Saarakkala, M.T. Nieminen, J. Hirvonen, J.S. Jurvelin, Biomechanical properties of knee articular cartilage., Biorheology. 40 (2003) 133–40. http://www.ncbi.nlm.nih.gov/pubmed/12454397.

[231] O. Franke, K. Durst, V. Maier, M. Göken, T. Birkholz, H. Schneider, F. Hennig, K. Gelse, Mechanical properties of hyaline and repair cartilage studied by nanoindentation, Acta Biomaterialia. 3 (2007) 873–881. https://doi.org/10.1016/j.actbio.2007.04.005.

[232] H. Lee, R. Eom, Y. Lee, Evaluation of the Mechanical Properties of Porous Thermoplastic Polyurethane Obtained by 3D Printing for Protective Gear, Advances in Materials Science and Engineering. 2019 (2019) 1–10. https://doi.org/10.1155/2019/5838361.

[233] R. Christensen, A. Astrup, H. Bliddal, Weight loss: the treatment of choice for knee osteoarthritis? A randomized trial, Osteoarthritis and Cartilage. 13 (2005) 20–27. https://doi.org/10.1016/j.joca.2004.10.008.

[234] P.O. Kotzki, D. Buyck, D. Hans, E. Thomas, F. Bonnel, F. Favier, P.J. Meunier, M. Rossi, Influence of fat on ultrasound measurements of the Os calcis, Calcified Tissue International. 54 (1994) 91–95. https://doi.org/10.1007/BF00296057.

[235] N.M. Selkow, B.G. Pietrosimone, S.A. Saliba, Subcutaneous Thigh Fat Assessment: A Comparison of Skinfold Calipers and Ultrasound Imaging, Journal of Athletic Training. 46 (2011) 50–54. https://doi.org/10.4085/1062-6050-46.1.50.

[236] J.M. Tanner, P.C.R. Hughes, R.H. Whitehouse, Radiographically determined widths of bone muscle and fat in the upper arm and calf from age 3–18 years, Annals of Human Biology. 8 (1981) 495–517. https://doi.org/10.1080/03014468100005351.

[237] H.W. Borchers, pracma: Practical Numerical Math Functions, (2021). https://cran.r-project.org/package=pracma.

[238] N.E. Huang, N.O. Attoh-Okine, eds., The Hilbert-Huang Transform in Engineering, CRC Press, 2005. https://doi.org/10.1201/9781420027532.

[239] K.M.M. Prabhu, Window Functions and Their Applications in Signal Processing, CRC Press, 2018. https://doi.org/10.1201/9781315216386.

[240] T. Manabe, S. Wakui, Production and Application of Horizontal Jerk Sensor, in: 2018 International Conference on Advanced Mechatronic Systems (ICAMechS), IEEE, 2018: pp. 298–303. https://doi.org/10.1109/ICAMechS.2018.8506990.

[241] N.K. Vitanov, K. Sakai, Z.I. Dimitrova, SSA, PCA, TDPSC, ACFA: Useful combination of methods for analysis of short and nonstationary time series, Chaos, Solitons & Fractals. 37 (2008) 187–202. https://doi.org/10.1016/j.chaos.2006.08.043.

[242] A. Zhigljavsky, Singular Spectrum Analysis for time series: Introduction to this special issue, Statistics and Its Interface. 3 (2010) 255–258. https://doi.org/10.4310/SII.2010.v3.n3.a1.

[243] R. Gong, K. Hase, H. Ohtsu, S. Ota, Adaptive Vibrarthographic Signal Denoising via Ant Colony Optimization Using Dynamic Denoising Filter Parameters, International Journal of Engineering and Technology Innovation. 12 (2022) 1–15. https://doi.org/10.46604/ijeti.2021.8718.

[244] Rui GONG, Kazunori HASE, Sentong WANG, Susumu OTA, A Novel Attempt for Diagnosing Outerbridge Classification of Articular Cartilage Damage via Vibration Transmission (in press) , Journal of Biomechanical Science and Engineering. (n.d.).